2019

Mechanism Study of Shale Gas Conversion via Chemical Looping and Heterocatalytic Processes

Lei Bai
West Virginia University, lebai@mix.wvu.edu

Mechanism Study of Shale Gas Conversion via Chemical Looping and Heterocatalytic Processes

Lei Bai

Dissertation submitted to
the Benjamin M. Statler College of Engineering and Mineral Resources
at West Virginia University

in partial fulfillment of the requirements for the degree of

Doctor of Philosophy in the
Chemical and Biomedical Engineering

Hanjing Tian, Ph.D. Committee Chairperson

Jianli Hu, Ph.D.

John W. Zondlo, Ph.D.

Xingbo Liu, Ph.D.

Zili Wu, Ph.D.

Department of Chemical and Biomedical Engineering
Morgantown, West Virginia
2019

Keywords: Shale Gas, Chemical Looping Combustion, Oxidative Coupling of Methane, Dehydro-aromatization of Ethane.

ABSTRACT

Mechanism Study of Shale Gas Conversion via Chemical Looping and Heterocatalytic Processes

Lei Bai

The shale gas revolution has significantly changed the energy landscape in US. The technical-feasible, energy-effective schemes for shale gas combustion and utilization, especially from remote resources, have attracted increasing interest due to expensive transportation/distribution cost. In this research, for the first time, chemical looping combustion (CLC) of methane with inherent CO_2 capture, oxidative coupling of methane (OCM) and dehydro-aromatization (DHA) of ethane are systematically studied as promising alternatives at O_2-rich, O_2-lean and non-oxidative conditions, respectively.

Chemical looping combustion is bridging clean fuel combustion in energy production with inherent CO_2 capture. CLC utilized an oxygen carrier (OC) to transfer oxygen to the fuel source in O_2-rich conditions. However, the fundamental kinetics of surface structure with oxygen transfer on OC, as well as the reduction activity and coupled selectivity have yet been established. OCM directly converts methane to produce C_2 hydrocarbons (C_2H_6 and C_2H_4) in O_2-lean condition. Perovskite catalysts have shown promising activity and selectivity to C_2, but the role of surface acidity of perovskite-type catalyst on OCM kinetics has not been revealed. Non-oxidative ethane DHA provides an economical and environmentally friendly alternative for aromatics and H_2 production. Pillared ZSM-5 with hierarchical pores could amplify the mass/heat transfer, which is a promising catalyst for DHA reaction. However, very few studies have been reported to directly associate the thickness of lamellar layers with reactant diffusion, Si/Al ratios, surface acidities as well as catalytic reactivity of ethane-DHA reaction.

The research objective is to provide fundamental insights of surface structure-performance relationship of model catalysts for catalytic C2/C3 conversion in three aspects: 1) the oxygen transfer mechanisms in CLC by using surface calcium-doped (1, 2 and 4 wt%) copper oxides based OC; 2) the effect of surface compositions of perovskites on the OCM by using $SrTiO_3$ as a model catalyst is investigated; and 3) a regenerable MoO_x/lamellar ZSM-5 based on the strategy of optimizing micro/mesopores structure of zeolite framework, targeting high ethane conversion and aromatic selectivity by optimizing Si/Al ratio, surface acidity and diffusion path. The work offers several economic-viable and technical-feasible solutions for shale gas utilization to value-added products.

Dedication

To my family, friends, and colleagues who have given their selfless support throughout my doctoral education.

Acknowledgements

I would like to express my sincere gratitude to my advisor Dr. Hanjing Tian for giving me the opportunity to join his research group and for his guidance throughout my endeavor at West Virginia University. His profound knowledge and expertise about chemical looping and catalysis research field were inspirational and broaden my scientific horizon.

I would like to thank my co-advisor Dr. Zili Wu in Oak Ridge National Laboratory for providing an extensive background in scientific research and problem solving. His profound knowledge about the catalysis throughout his active experience in academia helps and encourages me during my graduate research.

I am honored to have Dr. Jianli Hu, Dr. John W. Zondlo, and Dr. Xingbo Liu as my committee. I would like to thank my committee members for their time and contribution to my doctoral education.

I wish to thank Department of Chemical and Biomedical Engineering in West Virginia University, Oak Ridge National Laboratory and National Science Foundation for sponsoring my doctoral education and research activities. I have had the great opportunity to get trained at Argonne National Laboratory and Oak Ridge National Laboratory for the neutron and synchrotron experiments.

I would like to thank Dr. Jarrett Riley, Dr. William J. Benincosa III, Dr. Felipe Polo-Garzon and Dr. Zhenghong Bao for their support and suggestions on my Ph.D. research.

I would like to express my deepest gratitude to my loving parents, Mr. Liming Bai and Mrs. Caiping Liu for their love, encouragement and support. I would like to thank girlfriend Dr. Xiao Hu for her constant motivation throughout this process.

Table of Contents

List of Figures

Chapter 1. Introduction

Chapter 2. Mechanism study of methane/char chemical looping reduction process over calcium-doped copper oxide as oxygen carrier

Figure 7: CO_2 (a) and CO (b) concentration in product gas during the temperature ramp as a function of time from reaction performance of char/OCs mixtures.

Figure 8: (a) CO_2 and (b) CO concentration in product gas during the temperature ramp as a function of time from reaction performance of oxygen carriers and methane.

Figure 9: H_2 concentration in product gas as a function of time during the temperature ramp of the reaction between oxygen carriers and methane. The curves in the small window represent the original curves for four oxygen carriers. Deconvolution peaks (r1, r2, r3, r4) of H_2 concentration profiles are shown in the main window.

Figure 10: Scheme schematic of the contributing reactions in the CH_4/oxygen carrier system.

Chapter 3. Impact of Surface Composition of $SrTiO_3$ catalysts for Oxidative Coupling of Methane (OCM)

Figure 12: (a) CH_4 conversion, (b) CO_2 yield, (c) CO yield, (d) C_2H_6 yield and (e) C_2H_4 yield with respect to the composition of the top surface of various STO samples at different catalyst bed temperatures (600, 650, 700, 750, 800°C) for OCM reaction with conditions in present work.

Figure 13: Rate of CH_4 conversion versus composition of outermost atomic layer of various STO samples at different temperatures for methane combustion.

Figure 14: (a) Ratio of C_2/CO_x yield and (b) ratio of ethylene/ethane yield as function of top surface composition at different catalyst bed temperatures over various STO samples.

Figure 15: (a) Arrhenius plots for the CH_4 consumption rate. (b) Apparent activation energies (Ea) measured under differential conditions, for CH_4 consumption rate over STO catalysts under study with different surface Sr concentration. Experimental conditions: 5 mg catalyst, 1.0 atm, feed consists of 25 mL/min of 10% CH_4/Ar, 10 mL/min of 5% O_2/He, and 15 mL/min of He as balance gas.

Figure 16: The Arrhenius plots for CO, CO_2 and C_2 formation during OCM over various STO catalysts.

Figure 17: CH_4 conversion as the function of the surface base site density and the acid site density for OCM reaction over various STO samples.

Figure 18: CH_4 conversion rate with respect to Base/(Base+Acid) ratio at different temperatures over various STO samples.

Figure 19: CH_4 conversion rate with respect to temperatures over various STO samples (with different Base/(Base+Acid) ratios).

Figure 20: Methane consumption rate as a function of (a) CH_4 pressure at $P(O_2)$=0.01 atm and of (b) O_2 pressure at $P(CH_4)$=0.04 atm, respectively, over various STO samples. (Reaction conditions: 650 °C for bed temperature, total flow rate=50 mL/min, He+Ar as balance gas.)

Figure 21: Effect of (a) CH_4 partial pressure on CH_4 conversion rate at $P(O_2)$=0.01 atm and (b) O_2 partial pressure on CH_4 conversion rate at $P(CH_4)$=0.04 atm at 650°C.

Figure 22: (a) Plots of $\frac{P_{O_2}^{0.5}}{r_{CH_4}}$ against $\frac{1}{P_{CH_4}}$ at $P(O_2)$=0.01 atm and (b)plots of $\frac{P_{CH_4}}{r_{CH_4}}$ against $\frac{1}{P_{O_2}^{0.5}}$ at $P(CH_4)$=0.04 atm at 650 °C.

Figure 23: Linearized correlations of (a) $\frac{P_{CH_4}}{r_{CH_4}}$ versus P_{CH_4} and (b) $\frac{P_{O_2}}{r_{CH_4}}$ versus P_{O_2}. The inset in (b) shows an enlarged image of Sr/STO(HNO_3)-2, STO, Sr/STO-1, Sr/STO-2 samples.

Figure 24: Linearized correlations of (a) $\frac{P_{CH_4}}{r_{CH_4}}$ versus $\frac{1}{P_{O_2}}$, and (b) $\frac{P_{O_2}}{r_{CH_4}}$ versus $\frac{1}{P_{CH_4}}$. The inset in (a) shows an enlarged image of Sr/STO(HNO_3)-2, STO, Sr/STO-1, Sr/STO-2 samples.

Chapter 4. Fabrication of Pillared ZSM-5 Framework for Shape Selectivity of Ethane Dehydroaromatization

Figure 8: TPO profiles for spent Mo/MFI-50(T0), Mo/MFI-50(T2), Mo/MFI-50(T8), Mo/MFI-25(T8), Mo/MFI-100(T8) catalysts after ethane dehydro-aromatization reactions.

Figure 9:Ethane dehydro-aromatization reaction-regeneration cyclic operation. a), b) plots of ethane conversion and aromatic yield achieved on Mo/Commercial MFI catalyst in each reaction cycle; c), d) plots of ethane conversion and aromatic yield achieved on Mo/MFI-50(T8) in each reaction cycle.

Figure 10: TPO profiles for fresh Mo/Commercial MFI and Mo/MFI-50(T8) catalyst after the fourth dehydro-aromatization reactions-regeneration cycles. The curves in the small window represent the original curves between two used catalysts. Deconvolution peaks of TPO profiles in the main window: a) back solid line and red solid line stand for carbide associated with Mo species over Mo/Commercial MFI and Mo/MFI-50(T8), respectively; b) black and red dash-dot-dash lines are assigned to coke combined with Brønsted acid sites over Mo/Commercial MFI and Mo/MFI-50(T8), respectively.

List of Tables

Chapter 2. Mechanism study of methane/char chemical looping reduction process over calcium-doped copper oxide as oxygen carrier

Chapter 3. Impact of Surface Composition of $SrTiO_3$ catalysts for Oxidative Coupling of Methane (OCM)

Chapter 4. Fabrication of Pillared ZSM-5 Framework for Shape Selectivity of Ethane Dehydroaromatization

Table of Abbreviations

CLC	Chemical Looping Combustion
CLOU	Chemical Looping with Oxygen Uncoupling
OC	Oxygen Carrier
Me_xO_y	Metal Oxide
Me_xO_{y-1}	Regenerated Metal Oxides
Me	Regenerated Metal Species
TGA	Thermogravimetric Analysis
XRD	X-Ray Diffraction
XPS	X-Ray Photoelectron Spectroscopy
TPR	Temperature Programmed Reduction
TCD	Thermal Conductivity Detector
UHP	Ultra-High Purity
UV-vis	Ultraviolet-visible Spectroscopy
CDM	Catalytic Decomposition of Methane
OCM	Oxidative Coupling of Methane
STO	$SrTiO_3$
LEIS	Low Energy Ion Scattering
UV-Raman	Ultraviolet-Raman
TPD	Temperature Programmed Desorption
MTO	Methanol-to-Olefins
FT	Fischer-Tropsch

NSR	NO_x Storage and Reduction
IWI	Incipient Wetness Impregnation
BET	Brunauer-Emmett-Teller
AMI	Altamira Instruments System
GC	Gas Chromatograph
RDS	Rate-Determining Step
Ea	Apparent Activation Energies
BTX	Benzene, Toluene and Xylene
DHA	Dehydroaromatization
SDA	Structure Directing Agent
TPAOH	Tetrapropylammonium Hydroxide
CTAB	Cetyltrimethylammonium Bromide
DI water	Deionized water
SEM	Scanning Electron Microscopy
TPO	Temperature-Programmed Oxidation
MS	Mass Spectrometry
BJH	Barrett-Joyner-Halenda
MAS	Magic-Angle Spinning
NMR	Nuclear Magnetic Resonance
DFT	Density Functional Theory
TOS	Time-on-Stream
TOF	Turn-over-Frequency

Chapter 1. Introduction

Due to the innovative technological advances in horizontal drilling and hydraulic fracturing, a boom in shale gas (mainly CH_4) production has emerged in the U.S during last decade.[1] According to an Energy Information Administration report[2], shale gas production rose by over 670% from 1.77 trillion cubic feet in 2000 to 13.64 trillion cubic feet by 2015.(See Fig. 1) The U.S. government also projects that the annual domestic shale gas production will account for 68% of United States gas supply by 2040. Recoverable deposits of shale gas are distributed worldwide, with major deposits in the countries in Asia, Europe, Latin America and many other regions.[3] The impact of the shale gas revolution has been notable in many areas of applications, including electricity/power generation, automobiles and transportation, residential heat supply, industrial and commercial applications.[4]

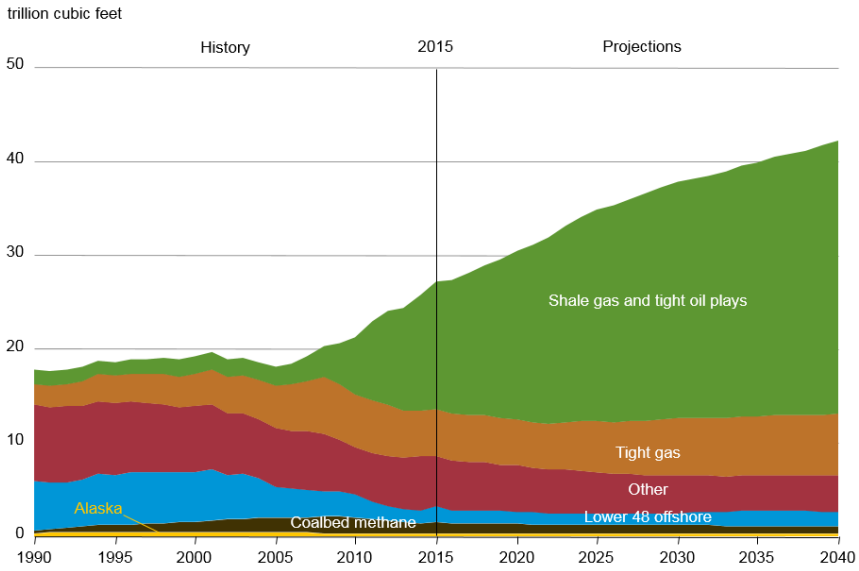

Figure. 1 U.S. dry natural gas production over the past and prediction.

Source: U.S. Energy Information Administration, *Annual Energy Outlook 2018* .
Note: "Tight oil" is light crude oil contained in petroleum-bearing formations of low permeability, often shale or tight sandstone, known as shale oil. "Tight gas" is natural gas produced from reservoir rocks with such low permeability that massive hydraulic fracturing is necessary to produce the well at economic rates. and "Coalbed methane" refers to is a form of natural gas extracted from coal beds.

Shale gas exists as the fossil natural gas trapped within shale formations. Shale is sedimentary rock composed of clay and other minerals, especially quartz and calcite. Over time, decaying biomass became trapped in these sedimentary layers and was converted into methane via anaerobic biological and chemical processes. Some of methane formed from the deposited biomass became encapsulated within the sedimentary rock layers, while portions of the methane escaped to more superficial rock layers, ultimately yielding what is now known as conventional natural gas resources. However, a considerable amount of methane remained trapped in the low permeability shale layers, and it is only with recent advances in drilling technology that it has become economical to recover methane from these shale gas deposits.[5, 6] The composition of shale gas varies on the location of the shale reservoirs. The gas contains methane (70–90%), as the major component, along with other hydrocarbons, such as ethane, propane, butane (0–20%) and gases such as carbon dioxide and nitrogen (0–5%). Especially, ethane is the second main component in some shale reservoirs. For example, the ethane component of the gas from Marcellus and Barnett shales are 16.1 and 11.8%, respectively[7, 8]. Moreover, in some regions of the United States, the price of ethane is actually lower than natural gas[9].

On one hand, natural gas is now the largest source of U.S. electric power generation, helping reduce U.S. greenhouse gas emissions to mid-1990 levels.[10] Natural gas combustion emits about half as much CO_2 as coal and 30 % less than oil, and far fewer pollutants, per unit of energy delivered. To fully realize the potential climate benefits of natural gas, technologies and policies must be put in place to capture carbon emissions.

Despite the positive advances with methane production, costs for shale gas shipment from production wells to potential end users is still high. A promising alternative to these high gas

shipping costs is to convert shale gas (methane and ethane) into a higher energy density liquid chemicals and fuels, which are more readily shipped via pipeline[11].

Dramatically increased supply of shale gas has led to a significant drop in natural gas prices. Therefore, there is potential to boost chemical and synthetic liquid fuel productions, providing methane from shale gas at low cost. However, the efficient conversion of shale gas to chemicals, liquid fuels, and electricity remains a major unsolved scientific problem. Therefore, there is a critical need to provide new and reliable approaches for further utilization of shale gas. Some promising alternatives are proposed in this project including methane combustion with inherent CO_2 capture, oxidative coupling of methane and ethane dehydroaromatization. Details of these techniques will be discussed in the following chapters.

Reference

[1] S. Luo, L. Zeng, D. Xu, M. Kathe, E. Chung, N. Deshpande, L. Qin, A. Majumder, T.-L. Hsieh, A. Tong, Z. Sun, L.-S. Fan, Shale gas-to-syngas chemical looping process for stable shale gas conversion to high purity syngas with a H_2:CO ratio of 2 : 1, Energy & Environmental Science, 7 (2014) 4104-4117.

[2] EIA - Annual Energy Outlook 2018. https://www.eia.gov/outlooks/archive/aeo18/, in, 2018.

[3] A. Galadima, O. Muraza, Revisiting the oxidative coupling of methane to ethylene in the golden period of shale gas: A review, Journal of Industrial and Engineering Chemistry, 37 (2016) 1-13.

[4] S. Clark, Shale Gas Market by End User (Industrial, Power generation, Residential, Commercial, Transportation) - Global Opportunity Analysis and Industry Forecast, 2014 - 2022, in, 2016.

[5] E.I. Administration, What is Shale Gas? https://geology.com/energy/shale-gas, in, 2010.

[6]Wikipedia,Shalegas.https://en.wikipedia.org/w/index.php?title=Shale_gas&oldid=859786243.

[7] A. Sharma, S. Namsani, J.K. Singh, Molecular simulation of shale gas adsorption and diffusion in inorganic nanopores, Molecular Simulation, 41 (2015) 414-422.

[8] K.A. Bulba, and Peter E. Krouskop, Compositional variety complicates processing plans for US shale gas, Oil & Gas Journal, 107 (2009) 50-55.

[9] H. Chen, L. Li, J. Hu, Upgrading of stranded gas via non-oxidative conversion processes, Catalysis Today, 310 (2018) 94-97.

[10] Nature Gas, At-a-glance. https://www.c2es.org/content/natural-gas/, in.

[11] F. Polo-Garzon, Optimization of pyrochlore catalysts for the dry refoming of methane, in: Chemical Engineering, Clemson University, 2015.

Chapter 2. Mechanism Study of Methane/char Chemical Looping Reduction Process over Calcium-doped Copper Oxide as Oxygen Carrier

Abstract

Chemical looping with oxygen uncoupling (CLOU) is a novel CO_2 capture technology which uses metal oxides to release gaseous O_2. Compared to regular chemical looping combustion (CLC), the advantage of CLOU is the instant oxygen releasing/transfer from the bulk or surface of oxygen carriers, so that the thermodynamic limits of the slow gasification step will be overcome. However, the fundamental kinetics of surface structure with oxygen transfer, as well as the reduction activity and coupled selectivity has not yet been established. In this study, calcium-doped (1, 2 or 4 wt%) copper oxide based oxygen carriers were prepared by the impregnation method and employed in CLC with Wyodak char and methane as fuels at 900^{o}C. Utilizing a combination of XRD and XPS analysis, calcium was confirmed to be dispersed on the surface of CuO. It is found that doping Ca improves CuO oxygen uncoupling characteristics. By comparing the chemical looping reduction process of Ca-doped CuO and un-doped CuO, Ca surface-doping increases the lattice oxygen transfer and surface O_2 formation under CLOU conditions. Meanwhile the comparison of thermal decomposition reactivity under an inert environment and *in-situ* Raman spectra of doped and undoped CuO suggested the change of reduction pathway from a sequential ($CuO \rightarrow Cu_2O \rightarrow Cu$) to a direct transition ($CuO \rightarrow Cu$) during oxygen carrier decomposition. Different mechanisms were revealed for the calcium-doped copper(II) oxide oxygen carriers when reacted with different fuel types (solid: char, gaseous: methane). For the char CLC reduction

process, more CO_2 was generated at a faster rate with CaO-doped CuO than with pure CuO. For methane CLC reduction, the calcium dopant not only accelerated the reaction rate, but also acted as an *in situ* adsorption site, which induced the methane reforming reaction.

2.1 Introduction

CO_2 emission from fossil fuels combustion has been regarded as a major factor attributing to global warming in past decades[1-3]. CO_2 capture and storage technologies are required to reduce the emission of this greenhouse gas. CO_2 post combustion separation and capture after coal-fired power plants are traditional technologies, which can carry a significant energy penalty. In contrast, the concept of chemical looping combustion (CLC) has been proposed as a promising low-cost CO_2 capture technology to produce energy with inherent CO_2 separation [4-6].

CLC is realized by the oxygen transfer from solid oxide materials to fuels. These solid oxide materials, called oxygen carriers (OCs), travel to and from between an air reactor and fuel reactor. In the fuel reactor, the oxygen carriers are reduced by the reaction with fuel, as shown below:

$$(2n+m)Me_xO_y + C_nH_{2m} \rightarrow (2n+m)Me_xO_{y-1} + nCO_2 + mH_2O \qquad (1)$$

where Me_xO_y denotes a metal oxide and Me_xO_{y-1} is reduced compound. The reduced oxygen carriers are transferred to the air reactor and oxidized by air. The regeneration of metal oxides is as follows:

$$Me_xO_{y-1} + \frac{1}{2}O_2 \rightarrow Me_xO_y \qquad (2)$$

Subsequently, the regenerated metal oxides travel back to the fuel reactor to initiate the next cycle. The oxygen transferred from air to fuels through metal oxides avoids direct contact between air and fuel. Consequently, CO_2 and H_2O can be obtained in a pure form without the need for energy-consuming separation. After simple condensation of steam, pure CO_2 can be easily captured and stored.

The development of oxygen carriers is a key aspect in CLC technology. A large number of oxygen carriers have been proposed and tested by numerous researchers[7-12]. Several transition metal oxides of Cu, Fe, Ni, Co, and Mn have served as conventional oxygen carriers in CLC[13, 14]. Among these suitable metal complexes, CuO has been singled out for its high reactivity and oxygen transport capacity[15]. Oxygen carriers are always supported by inert materials such as Al_2O_3, ZrO_2, TiO_2, or MgO to enhance their redox reactivity as well as the recyclability[15-17]. Recently researchers demonstrated that the significant modification of the metal crystal phase can be achieved via addition of secondary metals, including alkali metal ions (e.g. Li^+, Na^+ or K^+), transition metals, and rare earth metals. For example, Zheng et al.[18] synthesized $LaFeO_3$ supported CeO_2 oxygen carriers for chemical looping reforming of methane, and claimed that 10% $CeO_2/LaFeO_3$ produced higher yields of syngas and pure hydrogen than those of pure $LaFeO_3$. Galinsky et al.[19] reported that $CaMnO_3$ doped with 25% Sr exhibited a stabilized perovskite structure and noticeable oxygen release at significantly lower temperature than that observed for pure $CaMnO_3$, which can shift the initial reduction temperature by approximately 200 ℃. Cheng et al.[20] modified the Fe_2O_3-based oxygen carriers by different potassium salts (i.e. KNO_3, K_3PO_4, KOH, K_2CO_3), and pointed out that the 10% KNO_3/Fe_2O_3 was proven to be favorable oxygen carrier for CLC with methane due to its improved activity and redox characteristics and stability. However, the metal oxide crystal phases and structure of oxygen carriers, can be altered

due to the introduction of high concentration of dopants[16]. In addition, the oxygen carrying capacity can be degraded when a large quantity of dopant is added that does not contribute to the oxygen carrying capacity[16, 21]. Doping low concentrations of metal cations on the surface of oxygen carriers offers the possibility to improve reactivity and the oxygen releasing yield without changing the bulk phase structures. This approach is a challenging requirement for the oxygen carrier development field.

When solid fuels are used in CLC, the gasification of fuels occurs and generates products like CO and H_2. The reaction between gasification products with oxygen carriers (metal oxide particles) happens simultaneously along with the slow fuel gasification. In contrast, chemical looping with oxygen uncoupling (CLOU) is utilized as an alternative to burn the solid fuels, where the gaseous oxygen is released/transferred from the bulk or surface of oxygen carriers. Therefore, the solid fuels are combusted in gas-phase oxygen in CLOU, so that the thermodynamic limits for combustion reaction in regular CLC will be overcome by avoiding the slow gasification step. However, the fundamental kinetics of surface structure with oxygen transfer, as well as the reduction activity/selectivity has not yet been established.

This study is designed to probe the mechanism of surface oxygen transfer of the oxygen carriers during the chemical looping reaction by using CuO, with a CaO dopant well dispersed on the material surface. CaO is added as active dopant from 1-4 wt% to avoid modifying the CuO crystalline phase. A series of experiments was conducted to understand the reduction characteristics of the CaO doped CuO materials, including, gas-fueled reduction, uncoupling potential and solid-fueled oxygen transfer. To examine oxygen transfer in these scenarios, the surface modified CuO was reacted with Wyodak char (solid fueled), methane and hydrogen (gas

fueled) in the chemical looping process. In addition oxygen uncoupling potential was also explored. The reaction pathway of oxygen release/transfer on the CaO-CuO surface and the surface-doping effects were determined through the present study.

2.2 Experimental Section

2.2.1 Materials and Oxygen Carrier Synthesis

The concept of CLC with solid fuels such as coal or char has been investigated extensively in the past[13, 14, 22-24], and progress of the CLC technology for solid fuel combustion has been presented in various review articles[25-27]. Therefor we would like to firstly investigate the effect of surface modification of oxygen carriers on CLC performance when reacting with solid fuels, i.e. char. Wyodak coal samples in present work were obtained from the Penn State Coal Sample Bank (sample number: DECS-26). The composition of coal is listed in Table 1. Coal samples were crushed and ground, then pyrolyzed to remove volatiles and produce the chars. The coal samples were heated up to 900 ℃ at a ramp rate of 10 ℃/min in a vertical quartz tube furnace under atmospheric flow of 100mL/min pure helium and held isothermally for 30 min upon reaching the target temperature. Chars prepared from pyrolysis were subsequently ground and sieved to obtain particles below 106 μm. Although the ash is existing in the char, it is reported that the ash in the solid fuel does not affect the reactivity of the oxygen carriers in the CLC[28, 29].

Table 1. Proximate and ultimate analysis of Wyodak coal sample.

Proximate analysis (wt.%)				Ultimate analysis (wt.%)				
M_{ad}	V_d	A_d	FC_d	C_{daf}	H_{daf}	N_{daf}	S_{daf}	O_{daf}
26.23	44.86	7.57	47.57	75.48	6.11	1.02	0.47	16.92

Note: ad-air dry basis; d-dry basis; daf-dry and ash free basis

CaO-CuO-based oxygen carriers were synthesized by an impregnation method using calcium hydroxide and copper(II) oxide as metal oxide precursors. The calcium hydroxide and copper(II) oxide were purchased from ACROS ORGANICS in the purity of 98% and 99+%, respectively. A prescribed amount of calcium hydroxide was dissolved in deionized water to give a solution. The solution was added to dry copper(II) oxide at a volume equal to its pore volume to form a wet paste. A muffle furnace was then used to calcine the paste at a temperature of 550 ℃ for 10 min at a ramp rate of 5ºC/min to decompose the hydrate to the desired calcium oxides covering the surface of copper oxide. Samples with different CaO weight percentages are designated as 1wt%-CaO-CuO, 2wt%-CaO-CuO and 4wt%-CaO-CuO, referring to the number of successive impregnations. Pure copper oxide is also used as a baseline oxygen carrier for comparison. Sample size range for all oxygen carriers was less than 106 μm.

2.2.2 Oxygen Carriers Characterization

The prepared oxygen carriers were characterized by X-ray diffraction (XRD) and X-ray photoelectron spectroscopy (XPS) to probe whether the calcium dopant exists on the copper oxide surface.

The XRD analysis was carried out using on a Panalytical X'Pert Pro XRD system in the range of 20° to 80° for 2θ. Cu-Kα1 8047.2 eV source and a maximum X-Ray power of 45 kV and 40 mA were used.

X-ray photoelectron spectra (XPS) were obtained with a Physical Electronics PHI 5000 VersaProbe XPS system. A monochromated 25 W, 15 kV Al-Kα X-ray source (photon energy of 1486.6 eV) and a hemispherical analyzer were used. The routine operation pressure in the main chamber is ~1×10^{-9} Torr. All reported intensities are experimentally determined peak areas divided

by the instrumental sensitivity factors. The acquired spectra were collected using multiple scans, and the data were averaged and analyzed using MultiPak v9 software. All the spectra registered were referred to signal C 1s 284.8 eV corresponding to adventitious carbon. All XPS peak assignments were acquired based on the NIST XPS database[30].

2.2.3 Temperature-programmed Reduction Analysis of OCs

Temperature-programmed reduction (TPR) analysis was carried out in Micromeritics Autochem 2900 instrument coupled with a thermal conductivity detector (TCD), at a heating rate of 4 °C/min up to 900 °C, then holding at that temperature for 30 min. Approximately 150 mg of oxygen carriers sample was supported on a quartz wool plug inside the U-shaped quartz reactor and reduced with 5% H_2 (balanced with 95% He) as reducing agent (25 mL/min). A K-type thermocouple was placed in quartz wool for accurate temperature measurement.

2.2.4 Reaction Performance and OCs Decomposition Characterization

Chemical looping reduction experiments of oxygen carriers were performed by using the Micromeritics Autochem 2900 instrument (fixed-bed reactor) coupled with a Pfeiffer Omnistar mass spectrometer in order to identify the gaseous products formed during the reduction. When the char presented as the solid fuel, 60 mg char and 150 mg CaO-CuO oxygen carriers were mixed prior to the tests. Then the mixture was heated from 50 °C to 900 °C at a heating rate of 4 °C/min in helium at a flow rate of 25 mL/min at atmospheric pressure. After that, the sample was maintained at 900 °C for 30 min in helium. Methane was also presented as a gaseous fuel. 150 mg OC sample was loaded into quartz tube and heated to 900 °C at a heating rate of 4 °C/min hold for 30 min 20%CH_4/80%Ar stream at a flow rate of 25 mL/min.

The decomposition (uncoupling) experiments were carried out in U.H.P He atmosphere to ensure an inert environment to promote the reaction. 150 mg CaO-CuO sample was heated in flowing U.H.P He (flowing rate=25 mL/min) from 50 °C to 900 °C (ramping rate= 4 °C/min) and holding there for an additional 30 min.

2.2.5 Raman Spectroscopy of OCs Decomposition

The two oxygen carrier samples, pure CuO and 2wt%CaO-CuO, were decomposed *in situ* in a Raman catalytic reactor (Linkam CCR1000) before Raman spectral collection. The decomposition was done by heating the sample (ca. 15 mg) in flowing pure He (60 mL/min) from room temperature to 900 °C (ramping rate 20 °C /min) and holding there for an additional 5 min. Due to the decrease of Raman band intensities with increasing temperature,[31, 32] the spectra were collected at lower temperature to reduce this thermal effect. For example, after staying at each temperature (400, 500, 600, 700, 800, 900°C) for 5min, the sample was then cooled down to 300°C in He, and Raman spectra were collected with laser excitation of 532nm. Since the experiments were conducted in the sealed Raman cell with purging pure He, no reversible reaction for the oxygen carriers will occur when the temperature is decreased to 300 ^{o}C for spectra collection. The Raman measurements were performed on a multiwavelength Raman system at Oak Ridge National Laboratory's Center for Nanophase Materials Sciences.[33] Raman scattering was collected via a customized ellipsoidal mirror and directed by a fiber optic bundle to the spectrograph stage of a triple Raman spectrometer (Princeton Instruments Acton Trivista 555). Edge filters (Semrock) were used in front of the UV-vis fiber optic bundle (Princeton Instruments) to block the laser irradiation. The 532 nm excitation (20 mW at sample) is emitted from a solid-state laser (Princeton Scientific, MSL 532-50). A UV-enhanced liquid N_2-cooled CCD detector (Princeton Instrument) was employed for signal detection. The Raman reactor sits on an XY stage

(Prior Scientific, OptiScan XY system) and translates in raster mode while collecting the spectrum. The fast translation has shown to be able to eliminate/minimize any laser damage of the samples.[33]

2.3 Results and Discussion

2.3.1 Characterization of Oxygen Carriers

The respective X-ray diffraction (XRD) patterns of calcined oxygen carriers are shown in Figure 1. Pure CuO and CaO XRD patterns are characterized as references. XRD patterns of the oxygen carriers is identical to the single-phase CuO with a monoclinic structure and the positions of the peaks are in good agreement with PDF-4+ 2016 card of CuO (Reference code: 01-073-6234). XRD patterns exhibited strong diffraction peaks at 36°, 39°, 49°, 58°, 62°, 72° and 76°.The crystallographic parameters for this CuO unit cell are a=4.662 Å, b=3.417 Å, c=5.118 Å, α=γ=90°, β=99.48°. No peaks of impurity are observed in the oxygen carriers and CuO reference sample XRD patterns. XRD patterns of CaO reference sample was also shown in Fig. 1. Obvious peaks appeared with 2θ values of 32°, 37°, 54°, 64°, 67° and 80°, which were correspondent to a diffraction pattern of cubic calcium oxide with crystallographic parameters a=b=c=4.797 Å, α=β=γ=90° (matched by reference code:00-001-1160). For the XRD patterns from oxygen carriers, no peaks could be attributed to CaO or other precursor compounds. CuO is the only crystalline phase that is clearly apparent. The presence of copper and absence of calcium implies there is no interaction between calcium and copper oxide in the bulk phase.

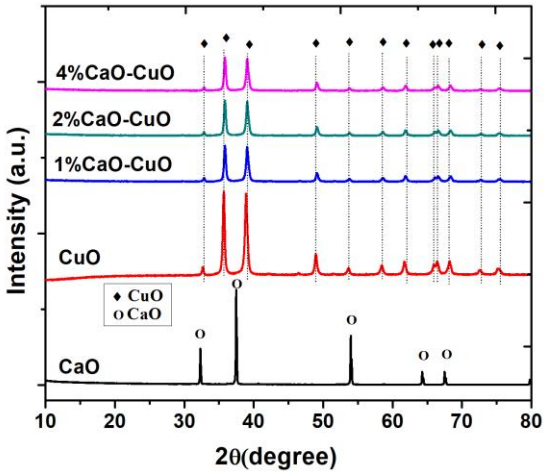

Figure 1. Powder XRD patterns of CaO-CuO oxygen carriers calcined at 550 °C

Even though bulk lattice oxygen is a crucial reactant, the reaction between oxygen carriers and solid fuels (i.e. coal, char and carbon black) was regarded to proceed at the solid-solid interface in some researches[24, 34, 35]. It is therefore important to investigate the surface properties of oxygen carriers in addition to their bulk structural properties. The near-surface elemental compositions of the as-prepared CaO-CuO oxygen carriers as determined by XPS. From the survey scan, Cu2p, Ca2p and O1s peaks are observed, which is understandable due to the OCs synthesis procedure. Apart from these, a significant amount of carbon is detected at the outer surface. This is due to carbonaceous contaminations, deposited on the sample during sample transfer under ambient conditions, which are frequently measured by XPS. On the other hand, this contamination may also result from the formation of small amounts of calcium carbonate, which is caused by the unavoidable absorption of CO_2 in air by calcium oxide in CaO-CuO sample.

Calcium-doped samples O1s and Ca2p profiles are also examined and shown in Figure 2. Two major peaks are identified in the O1s profiles in Figure 2(a). The major peak located at 531.5 eV can be assigned to calcium oxide, and the other major peak at 529.5 eV can be ascribed to lattice oxygen in copper (II) oxide. Comparing the relative intensities of CaO and CuO peaks, the

increased intensities for CaO peaks on the surface of 1wt%, 2wt% and 4wt% CaO-CuO samples were corresponding with the increasing amount of calcium addition. The XPS Ca2p spectra of calcium-doped CuO are shown in Figure 2(b). The Ca2p (2p1/2 and 2p3/2) binding energy values of 351.1 and 347.3 eV indicate that the oxidized Ca at the surface in the oxygen carriers can be assigned to calcium oxide as well. The increased Ca2p peak intensities are observed due to the increasing loading amount. The calcium enrichment on the oxygen carriers surface is proved by XPS atomic concentration analysis as well, which will be discussed later. The absence of calcium in the OC bulk phase presented by XRD analysis as well as the presence of calcium on the surface illustrated by XPS analysis prove that the calcium is doped only on the surface of copper oxide as desired.

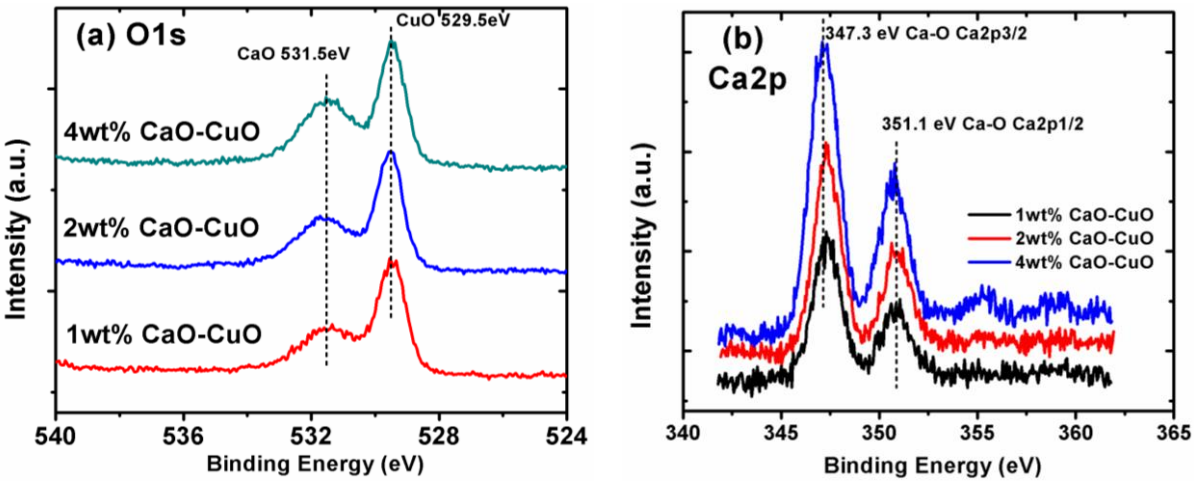

Figure. 2 Detailed O1s XPS scan for OC samples with different amount of doping calcium

The degree of Ca surface enrichment can also be quantified by calculating the near surface Ca concentration. The bulk theoretical calcium molar ratio can be estimated by assuming the oxygen carriers to be homogeneous mixture of CaO-CuO samples with different Ca-doping amounts. The calculated molar ratios of Ca and Cu of 1, 2, 4wt% CaO-CuO samples are listed in Table 2. As it shown, a significant surface enrichment of calcium can be observed on all Ca-doped oxygen carriers. The near-surface Ca concentration becomes more pronounced with a higher

amount of Ca addition, while Cu drops to 84.9%. It is necessary to pay attention that the Ca concentration derived from XPS is much higher than theoretical ones in bulk. Thus it is concluded that the calcium is accumulated on the CuO surface and it is valuable to study the impact of this surface doping on CLC, which will be discussed in later sections.

Table 2. Ca and Cu Concentrations of 1, 2, 4wt% CaO-CuO samples (Excluding oxygen) (%)

Sample	Surface metals concentration from XPS		Theoretical metals concentration in bulk	
	Ca2p	Cu2p	Ca	Cu
1wt%CaO-CuO	8.3	91.7	1.8	98.2
2wt%CaO-CuO	12.0	88.0	3.6	96.4
4wt%CaO-CuO	15.1	84.9	7.1	92.9

2.3.2 Temperature-Programmed Reduction Analysis

To study the reducibility of the CaO-CuO oxygen carriers, Temperature-Programmed Reduction (TPR) was performed on all prepared oxygen carrier samples in 5%H_2/95%He atmosphere. Pure CuO was also examined as a reference. The normalized H_2 TPR profile is presented and three peaks are obtained in Figure 3. The corresponding peak areas are summarized in Table 3. Figure 3(a) illustrated that all Ca-doped samples show three main peaks with a maximum at 277 °C, 357 °C, 532 °C, which are donated as α, β, γ, respectively. In contrast, only α peak is obtained for pure CuO sample. The α peak is ascribed to the reduction of CuO to metallic copper. Besides, water is detected at the exit of the reactor with a mass spectrometer when CuO reduction occurred. A similar report was found in previous investigation on CuO TPR study[36]. After the CuO is reduced, β and γ peaks start to appear after 300 °C, as shown in Figure 3(b). To identify these two following peaks, pure calcium oxide is subjected to H_2-TPR and two noticeable peaks are observed at the same temperatures with those of β and γ peaks. Therefore, β and γ peaks are assigned to the reduction of doped calcium compounds on OC surface. Water is detected by

the mass spectrometer as well when the temperature is ~357 °C (β peak). This water is produced by the reaction between oxygen in CaO and hydrogen, indicating that the β peak stemmed from the reduction of CaO in the oxygen carriers. As for γ peak, it is partially caused by the Ca-O bond reduction in H_2 as well, which is observed around 600°C in another report[37]. On the other hand, the γ peak is caused by calcium carbonate decomposition, which is proved by the CO_2 appearance in low concentration from mass spectrometer analysis. Thus, produced CO_2 partially contributes to the signal intensity of γ peak which was detected by TCD. The presence of $CaCO_3$ is consistent with the detected impurity carbon atom described by XPS in Section 3.1. As summarized in Table 3, the relative peak areas of α peak decrease slightly with calcium dopant amount in the order: pure CuO > 1wt% CaO-CuO >2wt% CaO-CuO > 4wt% CaO-CuO. This is because the introduction of inactive calcium sacrifices a small amount of oxygen transfer capacity of CuO. The intensity and peak area of β and γ are increasing with CaO loading from 1wt% to 4wt%. Furthermore, γ peak positions shifts with increasing CaO loading from 525 to 550 °C. It is believed that samples with finely dispersed CaO (lower calcium dopant) tend to be reduced at lower temperature.[38]

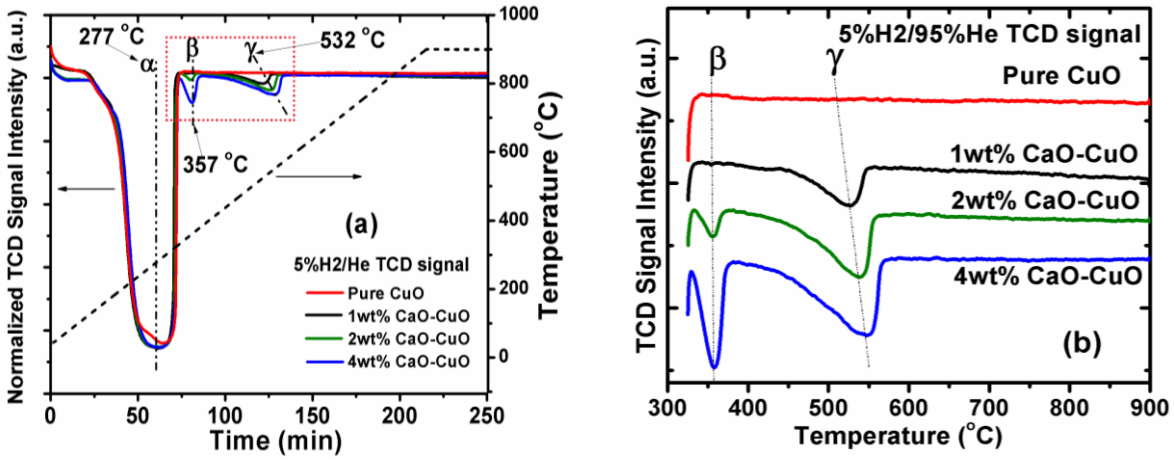

Figure. 3 H_2 temperature-programmed reduction profiles for three CaO-CuO OCs and pure CuO. (a) plot of TCD signal/Temperature vs. Time during whole reduction process; (b) plot of TCD signal vs. Temperature in 300-900 °C range.

Table 3. Peak areas for H_2-TPR peaks.

Sample	Area for α peak (a.u.)	Area for β peak (a.u.)	Area for γ peak (a.u.)	Area for α+β+γ peak (a.u.)	CuO reduction peak area (α peak) in percentage (%)	Total peak areas (α+β+γ peaks) in percentage (%)	Theoretical CuO amount (wt%)
Pure CuO	52.11	0	0	52.11	100	100	100
1wt%CaO-CuO	50.64	0	0.86	51.5	97.2	98.8	99
2wt%CaO-CuO	49.81	0.16	1.64	51.61	95.6	99.0	98
4wt%CaO-CuO	48.17	0.95	2.35	51.47	92.4	98.8	96

2.3.3 Effect of Calcium on CLOU

In order to understand how the oxygen uncoupling reaction from the CaO-CuO oxygen carrier is affected by Ca-doping, decomposition of CaO-CuO oxygen carriers with different Ca contents and pure CuO were conducted in helium. Oxygen concentration from the effluent gas stream was analyzed during the temperature ramp. The results are shown in Figure 4(a). Two peaks for released oxygen concentration are observed when pure CuO is decomposed in helium and this phenomenon is confirmed by repeated experiments. The first peak, centered at 880°C, can be assigned to the reduction of CuO to Cu_2O. Meanwhile, the second small peak represented the further transition of copper oxide state from Cu_2O to Cu, to release oxygen. The similar phase changes were also obtained by Siriwardane et al.[24] by using *in situ* XRD and XPS. These studies clearly showed that during carbon/CuO combustion: CuO was first converted to Cu_2O at relative low temperature, and then reaction proceeds until Cu_2O is fully converted to Cu metal at higher temperature.

In contrast, the addition of calcium significantly accelerates the reduction process, which is shown by single peak of the oxygen release when Ca-doped oxygen carriers are employed. Calcium addition on the surface strongly promotes the reduction process of copper oxide so that the carrier releases all the available oxygen in a single range of temperature to directly achieve full

conversion (from CuO to Cu). The data indicate that the presence of Ca is favorable for the oxygen un-coupling process, which is consistent with the data reported previously[21]. Before reaching the maximum value (215 min, ~880°C), the O_2 releasing rate (which can be represented by the slope of the curves in Figure 4(a)), increased in the order: pure CuO ≈ 1wt%CaO-CuO < 4wt%CaO-CuO < 2wt%CaO-CuO. Figure 4(b) displays the O_2 production rate over temperature [$dC(O_2)/dT$] at the ramping stage, which is represented by the first derivative of the O_2 concentration curve. The maximum O_2 production rates are found at 882, 863 and 879 °C for 1wt%CaO-CuO, 2wt%CaO-CuO, 4wt%CaO-CuO, respectively. Meanwhile the rate reaches maximum at higher temperature 885°C for pure CuO sample. Therefore, it is concluded that Ca can accelerate the oxygen release from CuO. Moreover, it can be seen that 2wt%CaO-CuO sample possesses both the maximum O_2 concentration and lowest peak temperature of O_2 production rate. This implies that when 2wt% CaO is doped and dispersed on CuO surface, monolayer coverage is formed to initiate and accelerate the decomposition reaction[39].

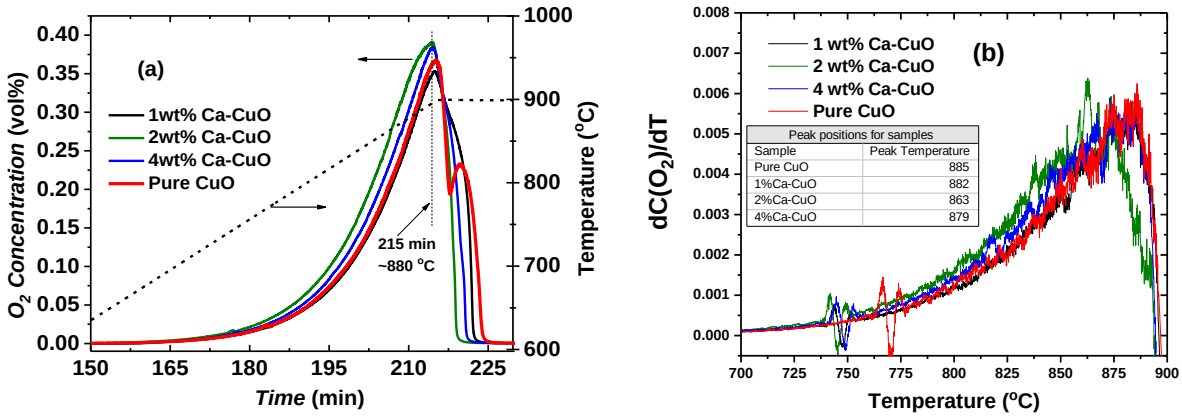

Figure. 4 O_2 concentration in product gas during the temperature ramp for decomposition of CaO-CuO oxygen carries and pure CuO.

2.3.4 Raman Spectra as Function of Temperature during OCs Decomposition

The *in situ* Raman was employed to test the pathway of copper(II) oxide reduction process during decomposition of oxygen carriers. The decomposition property of pure CuO and 2wt%-CaO-CuO was tested with temperature-programmed experiments coupled with *in situ* visible Raman spectroscopy. Figure 5(a) shows the 532nm excitation Raman spectra collected after different temperatures for pure CuO to correlate the observed change in reactivity (Section 2.3.3) with any structural changes to the lattice during the decomposition process. Since the Raman signal intensity is diminished with increased temperature, all Raman spectra were collected at 300°C after sample materials(both pure CuO and 2wt%-CaO-CuO) were heated up and kept for 5min at the desired temperature, i.e. 400-900°C.[32] Meanwhile, Raman spectra was collected at room temperature. In the Raman shift range of 100-600 cm^{-1}, CuO peaks are assigned at 290 and 329 cm^{-1}, while Cu_2O peaks were assigned at 219 and 408 cm^{-1}. The CuO and Cu_2O spectra agree well with the literature[40]. The plasma peaks noted in Figure 5, which are derived from the laser source itself[41], are regarded as an internal standard making Raman spectra at different temperatures comparable. As can be seen, for the pure CuO sample, only the CuO peaks at 290 and 329 cm^{-1} are existing and no extra peak is found when the temperature is lower than 800°C. When the temperature is raised to 900 °C, Cu_2O peaks at 219 and 408 cm^{-1} appear while CuO peaks diminish, even disappear. The appearance of Cu_2O and disappearance of CuO peaks confirm that CuO decomposed to Cu_2O when the temperature reached 900°C. This result is consist with the O_2 production from pure CuO sample decomposition in Section 2.3.3, the temperature for the first O_2 concentration peak is 880°C where the O_2 is generated from the transition from CuO to Cu_2O.

For the 2wt%-CaO-CuO sample, similarly, there is no phase changes of CuO when the temperature is lower than 800°C. However, when the temperature goes up to 900°C, CuO is

directly converted to metallic Cu, without producing Cu_2O. The Raman spectra for 2wt%-CaO-CuO along with pure CuO sample are compared in Figure 5(b). For 2wt%-CaO-CuO sample, it is obvious that CuO peaks diminish and still exist when the decomposition reaction occurs. No Cu_2O peaks are detected from the Raman spectra. The absence of Cu_2O and existence of CuO confirmed the one-step decomposition of Ca-doped CuO (CuO→Cu). Different reduction pathways are revealed through *in situ* Raman spectra and O_2 yield from oxygen carriers decomposition. The comparison of decomposition reactivity and *in situ* Raman spectra of doped and un-doped CuO suggested the change of reduction pathway from a sequential (CuO→Cu_2O→Cu) to a direct transition (CuO→Cu) during OCs decomposition. These different pathways can be illustrated in Figure 6. It can be explained that CaO potentially forms a surface structure with oxygen vacancies and electron gaps, which are regarded as the possible driving force to allow O_2 to form the surface O^{2-} anions moving from the solid lattice structure[42]. The further study on the cause for the change of CuO transition pathway is undergoing.

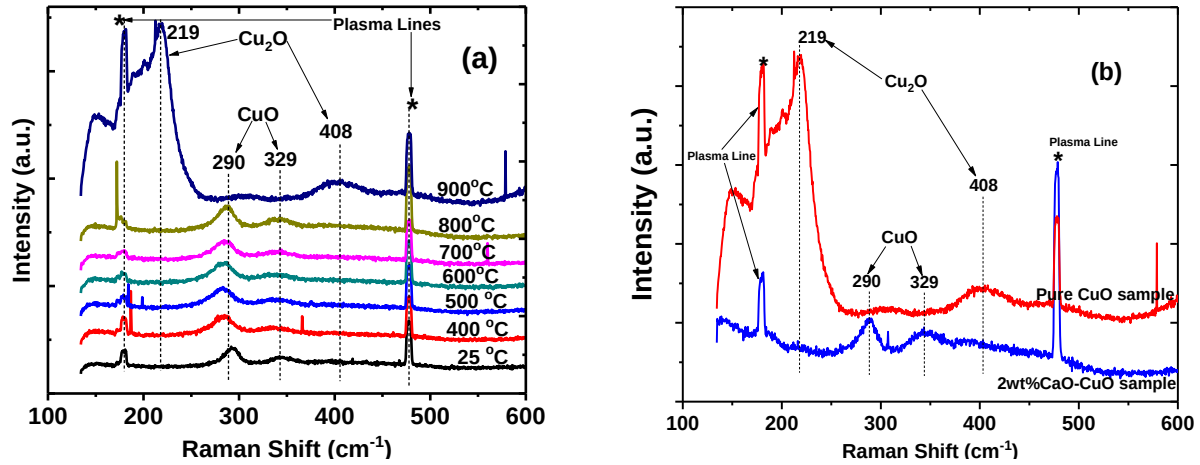

Figure. 5 Raman spectra (532 nm) of (a)pure CuO collected at different temperatures and (b)comparison between pure CuO and CaO-CuO oxygen carries at 900°C.

Note: * Peaks are denoted to plasma peaks, which are regarded as internal standard to make Raman peaks are comparable.

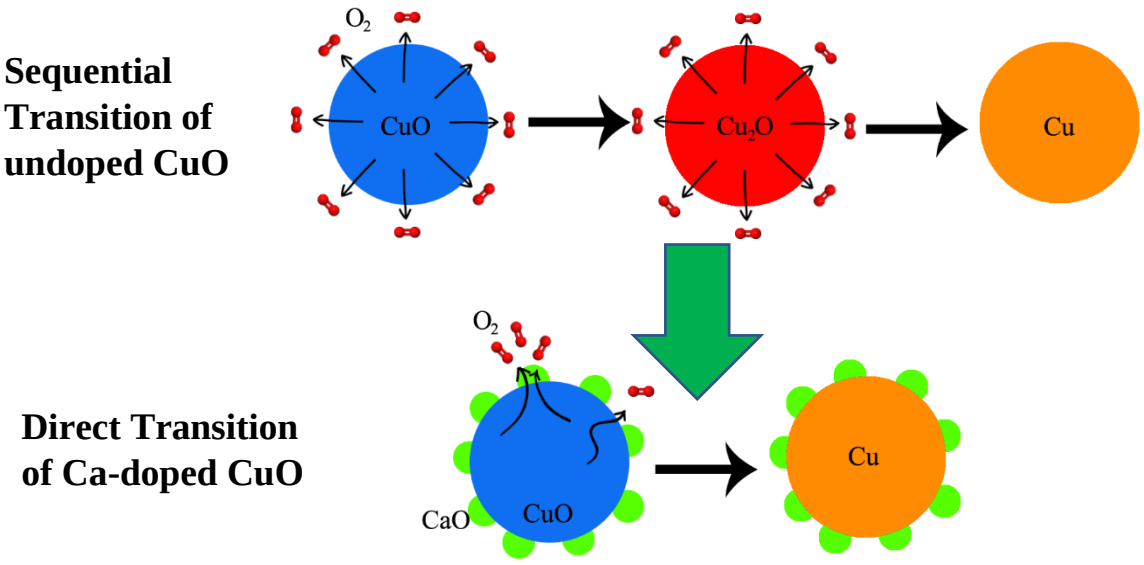

Figure. 6 Proposed reduction pathway scheme schematic for calcium-undoped/doped CuO based on decomposition reactivity and Raman spectra.

2.3.5 Effect of Surface-doped Calcium on CuO on Char-CLC Performance

To investigate the role of doped calcium on CuO surface on reaction performance of CLC, the mixtures of Wyodak Char and CuO oxygen carriers with various amount of CaO (1wt%, 2wt%, 4wt%) were heated to 900ºC and kept for 30 min. The concentrations of CO_2 and CO are presented as a function of time from reaction performance of char/OCs mixtures in Figure 7. When a mixture of char and CaO-CuO oxygen carriers was heated in helium, a combustion reaction with a significant rate is observed around 550 ºC, which is consistent with previous studies[14, 24]. Since volatiles are not produced from char[43, 44], the rapid reaction of CuO and char cannot proceed via the coal volatiles. Therefore, this reaction can only be explained as solid-solid interaction between metal oxide and solid fuel. It has been claimed that solid-solid reactions can occur with coal and oxygen carriers when there are significant contacts between the oxygen carrier and coal.

This kind of reaction mechanism is described as “fuel-induced oxygen release” from metal oxides and presented in the following equation[24, 45]:

$$Me_xO_y + \frac{1}{2}C \rightarrow xMe + \frac{y}{2}CO_2 \qquad (3)$$

The concentration peak of CO_2 with CaO-doped CuO were higher than that with pure CuO, indicating faster reaction rate with CaO-CuO. The relative amount of produced gases can be indicated by the areas of produced gas curve. In Figure 7(a), the areas of produced CO_2 employing CaO-CuO are clearly larger than that using pure CuO, indicating that there is additional carbon dioxide formation due to the presence of calcium surface-decorated oxygen carrier. Namely, more oxygen is released/transferred from the CuO at faster rate from either surface or bulk with the help of the calcium doped on the surface. Furthermore, it can be seen a significant CO_2 production from the 2wt%-CaO-CuO sample with the maximum values (3.81% for p1 and 5.32% for p2). These maximum values for p1 and p2 increased 47.1% and 26.7% compared to those for pure CuO sample (2.59% for p1 and 4.20% for p2). The reaction with 2wt%-CaO-CuO also takes place at a lower temperature than that with other samples which also indicates the best reactivity to process the chemical looping combustion of Wyodak char. As noted earlier in Section 2.3.3, when calcium oxide loading reached 2wt%, a CaO monolayer on CuO surface would be generated and then promote the CLOU characteristics of CuO-based oxygen carriers. This Ca monolayer probably is also the main reason for the best reactivity performance of 2wt% CaO-CuO sample to accelerate the OCs-char reaction to produce CO_2.

It is necessary to note that there are no significant changes in the peak intensity and amount of CO produced, as shown in Figure 7(b). CO was considered as the intermediate during the solid-

solid reaction between metal oxide and char. Saucedo et al.[46] also claimed that rapid oxidation of CO by the oxygen carrier (i.e. Fe_2O_3) to CO_2 occurred within the mass transfer boundary layer surrounding the char particle.

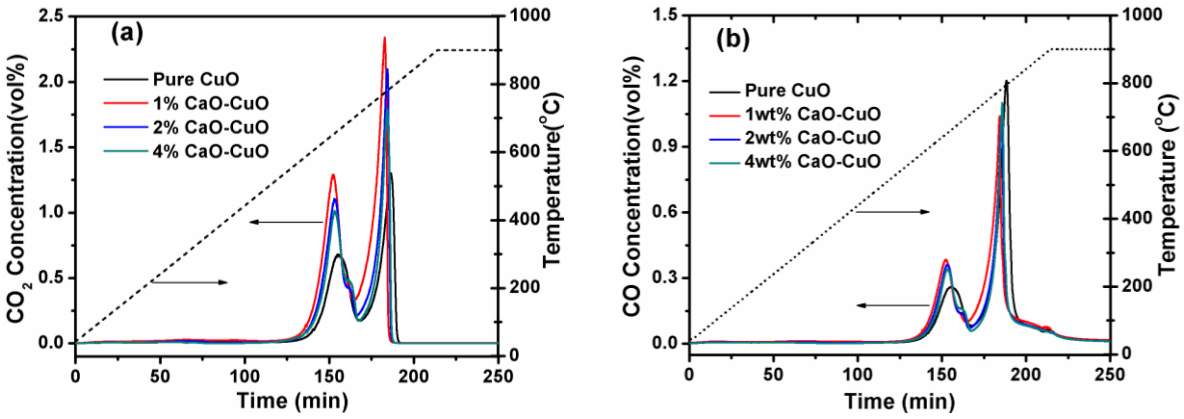

Figure. 7 CO_2 (a) and CO (b) concentration in product gas during the temperature ramp as a function of time from reaction performance of char/OCs mixtures.

2.3.6 Effect of Surfaced-doped Calcium on CuO on CH_4-CLC performance

The reaction performance of CaO-doped and pure CuO were conducted with 20 vol% CH_4/Ar and results are shown in Figure 8. Different from solid fuel (char) CLC, there are three peaks in produced CO_2 and CO concentrations plots, designated as p1, p2 and p3 for CO_2 and q1, q2 and q3 for CO, respectively. Similar data were reported elsewhere[24] explaining that p1 and p2 are attributed to two reaction steps during the CLC process: CuO is first reduced to Cu_2O at relatively low temperature, and then fully reduced to metallic Cu at higher temperature. CO_2/CO of p1/q1 is produced by the reaction of CH_4 with oxygen released from CuO→Cu_2O, while those of p2/q2 is acquired from the reaction of CH_4 with oxygen generated from Cu_2O→Cu. In Figure 8(a), the slight increase of CO_2 production rate (maximum value) is observed for CaO-CuO samples over the pure CuO, is attributed to the favorable influence of the alkali addition. During the CLC process, calcium oxide absorbs the released CO_2 so that the CO_2/CO production is delayed

for CaO-CuO samples compared with the pure CuO experiment. The third peak p3 appears when the temperature is higher than 500-550 ℃. $CaCO_3$ decomposes to be CaO and CO_2, thus a small CO_2 peak (p3) is found at the third stage. The generated CO_2 would also react with CH_4 at a relatively higher temperature and thus the methane reforming reaction is initiated to produce CO (q3). CaO-CO_2 adsorption and decomposition processes are also obtained and explained in the research about biomass catalytic pyrolysis with alkali-treated CaO/ZSM-5 by Sun et al.[47]. In addition, the methane reforming reaction is also promoted by the produced metallic Cu as catalyst[48]. Therefore, it is reasonable that the maximum value and peak area for both p3 and q3 peaks are pronouncedly increasing with the CaO doping amounts. H_2 concentration in the product gas as a function of time during the temperature ramp of the reaction between oxygen carriers and methane is shown in Figure 9. The H_2 concentration profile is deconvoluted into four peaks, designated as r1, r2, r3 and r4, respectively. A small amount of H_2 was generated at r1 and r2, which are corresponding to the CLC decomposition of CH_4 (simultaneously producing p1/q1 and p2/q2 peaks). r3 peak is generated by the above-mentioned dry (CO_2) reforming of methane. It is clear to see that H_2 concentrations derived by calcium doped samples are much higher than that of pure CuO sample. Moreover, the maximum H_2 concentration increases with the Ca loading amount, which is in line with the CO results. It is interesting to note that a set of peaks r4 shows up at higher temperature (700-800 ℃), where the catalytic decomposition of methane (CDM) is occurring[49-51]. When the temperature reaches 700 ℃, CuO has been reduced to metal Cu, which is not active for methane decomposition[52]. Meanwhile, the doped Ca as a catalyst, promotes the H_2 production[53], which is increasing with Ca dopant content. Many researches have reported that the calcium species, mainly CaO and calcium, could serve as promoters to improve the activity and lifetime of catalysts in methane decomposition[54-56]. The main reactions during the whole

CLC using CaO-doped CuO as oxygen carrier are summarized as shown below. The whole process could be expressed in Figure 10.

CLC of CH_4:	$CuO + \frac{1}{4}CH_4 \rightarrow Cu + \frac{1}{4}CO_2 + \frac{1}{2}H_2O$	(4)
CaO Adsorption:	$CaO + CO_2 \rightarrow CaCO_3$	(5)
CaO Decomposition:	$CaCO_3 \rightarrow CaO + CO_2$	(6)
Methane Reforming:	$CO_2 + CH_4 \rightarrow 2CO + 2H_2$	(7)
Methane Decomposition:	$CH_4 \rightarrow C + 2H_2$	(8)

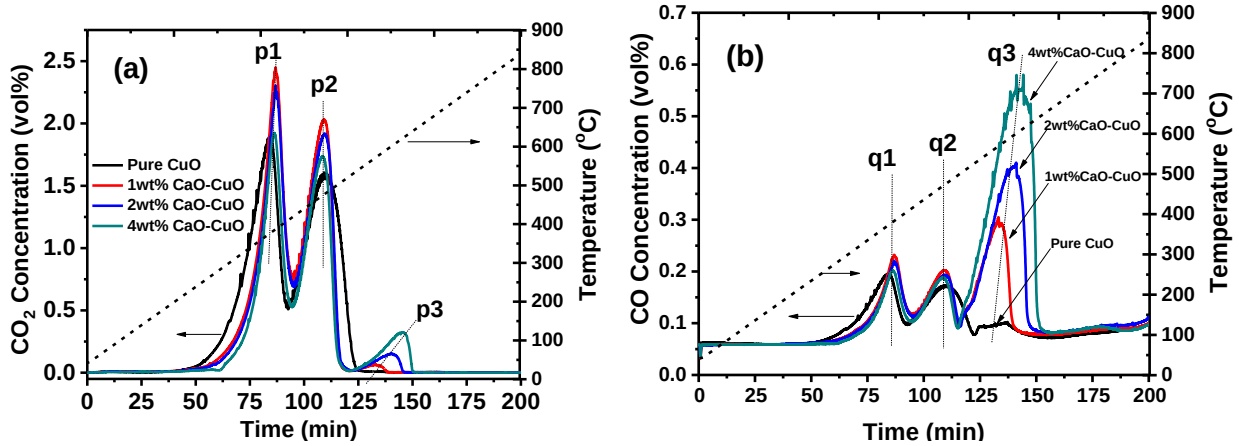

Figure. 8 (a) CO_2 and (b) CO concentration in product gas during the temperature ramp as a function of time from reaction performance of oxygen carriers and methane.

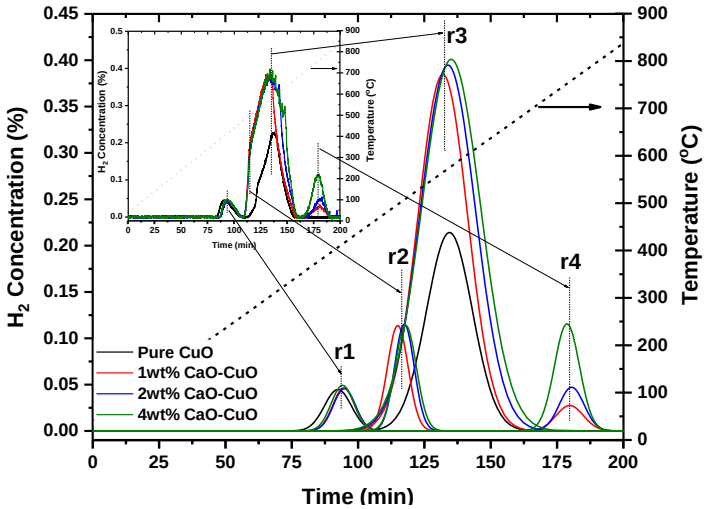

Figure 9. H_2 concentration in product gas as a function of time during the temperature ramp of the reaction between oxygen carriers and methane. The curves in the small window represent

the original curves for four oxygen carriers. Deconvolution peaks (r1, r2, r3, r4) of H_2 concentration profiles are shown in the main window.

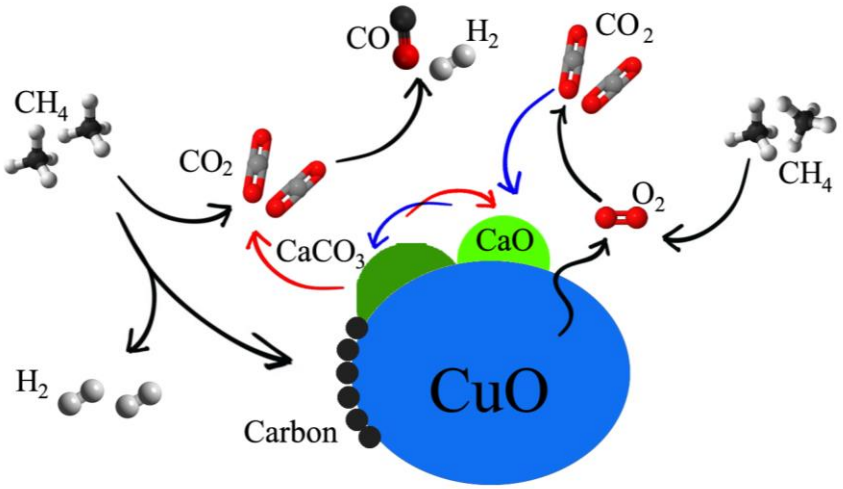

Figure. 10 Scheme schematic of the contributing reactions in the CH_4/oxygen carrier system

2.4 Conclusions

In this study, copper oxides were doped with calcium (1, 2 or 4 wt%) to improve reactivity and enhance surface controlled reactions. Combined results from XRD and XPS illustrate that the CaO is dispersed on CuO surface. CaO-CuO oxygen carriers present three reductive active sites corresponding to CuO reduction, CaO reduction and impurity $CaCO_3$ decomposition in 5%H_2-TPR process. It was claimed that doping Ca improves the CuO oxygen uncoupling characteristics. Ca surface-doping increases the lattice oxygen transfer and surface O_2 formation rate under CLOU conditions. Additionally, reduction pathway for CuO from a sequential (CuO→Cu_2O→Cu) to a direct transition (CuO→Cu) is verified through OCs decomposition and *in situ* Raman analysis. When char reacts as solid fuel in the CLC process, more CO_2 is generated at a faster rate with

CaO-doped CuO especially with 2wt% loading content. In contrast, when methane was used as gaseous fuel in the CLC process, the calcium dopant not only accelerated the reaction rate, but also induced the methane reforming reaction by reacting with released CO_2, that was initially bound in the form of $CaCO_3$, to promote the formation of CO and H_2.

Reference

[1] X. Zhao, H. Zhou, V.S. Sikarwar, M. Zhao, A.-H.A. Park, P.S. Fennell, L. Shen, L.-S. Fan, Biomass-based chemical looping technologies: the good, the bad and the future, Energy & Environmental Science, 10 (2017) 1885-1910.

[2] Q. Yi, W. Li, J. Feng, K. Xie, Carbon cycle in advanced coal chemical engineering, Chemical Society Reviews, 44 (2015) 5409-5445.

[3] A. Goeppert, M. Czaun, J.-P. Jones, G.K. Surya Prakash, G.A. Olah, Recycling of carbon dioxide to methanol and derived products – closing the loop, Chemical Society Reviews, 43 (2014) 7995-8048.

[4] R. Siriwardane, J. Riley, S. Bayham, D. Straub, H. Tian, J. Weber, G. Richards, 50-kWth methane/air chemical looping combustion tests with commercially prepared CuO-Fe_2O_3-alumina oxygen carrier with two different techniques, Applied Energy, 213 (2018) 92-99.

[5] K. Wang, X. Tian, H. Zhao, Sulfur behavior in chemical-looping combustion using a copper ore oxygen carrier, Applied Energy, 166 (2016) 84-95.

[6] A. Lyngfelt, Chemical-looping combustion of solid fuels – Status of development, Applied Energy, 113 (2014) 1869-1873.

[7] M. Arjmand, H. Leion, T. Mattisson, A. Lyngfelt, Investigation of different manganese ores as oxygen carriers in chemical-looping combustion (CLC) for solid fuels, Applied Energy, 113 (2014) 1883-1894.

[8] L. Chen, J. Bao, L. Kong, M. Combs, H.S. Nikolic, Z. Fan, K. Liu, The direct solid-solid reaction between coal char and iron-based oxygen carrier and its contribution to solid-fueled chemical looping combustion, Applied Energy, 184 (2016) 9-18.

[9] L. Chen, J. Bao, L. Kong, M. Combs, H.S. Nikolic, Z. Fan, K. Liu, Activation of ilmenite as an oxygen carrier for solid-fueled chemical looping combustion, Applied Energy, 197 (2017) 40-51.

[10] W. Yang, H. Zhao, J. Ma, D. Mei, C. Zheng, Copper-decorated hematite as an oxygen carrier for in situ gasification chemical looping combustion of coal, Energy & Fuels, 28 (2014) 3970-3981.

[11] T. Song, T. Shen, L. Shen, J. Xiao, H. Gu, S. Zhang, Evaluation of hematite oxygen carrier in chemical-looping combustion of coal, Fuel, 104 (2013) 244-252.

[12] M.R. Quddus, M.M. Hossain, H.I. de Lasa, Ni based oxygen carrier over γ-Al_2O_3 for chemical looping combustion: Effect of preparation method on metal support interaction, Catalysis today, 210 (2013) 124-134.

[13] R. Siriwardane, H. Tian, G. Richards, T. Simonyi, J. Poston, Chemical-Looping Combustion of Coal with Metal Oxide Oxygen Carriers, Energy & Fuels, 23 (2009) 3885-3892.

[14] Y. Cao, B. Casenas, W.-P. Pan, Investigation of chemical looping combustion by solid fuels. 2. Redox reaction kinetics and product characterization with coal, biomass, and solid waste as solid fuels and CuO as an oxygen carrier, Energy & Fuels, 20 (2006) 1845-1854.

[15] Y. Zhang, H. Zhao, L. Guo, C. Zheng, Decomposition mechanisms of Cu-based oxygen carriers for chemical looping with oxygen uncoupling based on density functional theory calculations, Combustion and Flame, 162 (2015) 1265-1274.

[16] L. Qin, Z. Cheng, M. Guo, M. Xu, J.A. Fan, L.-S. Fan, Impact of 1% lanthanum dopant on carbonaceous fuel redox reactions with an iron-based oxygen carrier in chemical looping processes, ACS Energy Letters, 2 (2016) 70-74.

[17] V. Manovic, E.J. Anthony, Integration of calcium and chemical looping combustion using composite CaO/CuO-based materials, Environmental science & technology, 45 (2011) 10750-10756.

[18] Y. Zheng, K. Li, H. Wang, D. Tian, Y. Wang, X. Zhu, Y. Wei, M. Zheng, Y. Luo, Designed oxygen carriers from macroporous $LaFeO_3$ supported CeO_2 for chemical-looping reforming of methane, Applied Catalysis B: Environmental, 202 (2017) 51-63.

[19] N. Galinsky, A. Mishra, J. Zhang, F. Li, $Ca_{1-x}A_xMnO_3$ (A= Sr and Ba) perovskite based oxygen carriers for chemical looping with oxygen uncoupling (CLOU), Applied energy, 157 (2015) 358-367.

[20] X. Cheng, K. Li, Y. Wei, X. Zhu, D. Tian, Modification of KNO_3 on the reducibility and reactivity of Fe_2O_3 - based oxygen carriers for chemical - looping combustion of methane, The Canadian Journal of Chemical Engineering, 95 (2017) 1569-1578.

[21] L. Duan, D. Godino, V. Manovic, F. Montagnaro, E.J. Anthony, Cyclic oxygen release characteristics of bifunctional copper oxide/calcium oxide composites, Energy Technology, 4 (2016) 1171-1178.

[22] T. Mattisson, A. Lyngfelt, H. Leion, Chemical-looping with oxygen uncoupling for combustion of solid fuels, International Journal of Greenhouse Gas Control, 3 (2009) 11-19.

[23] L. Shen, J. Wu, J. Xiao, Q. Song, R. Xiao, Chemical-Looping Combustion of Biomass in a 10 kWth Reactor with Iron Oxide As an Oxygen Carrier, Energy & Fuels, 23 (2009) 2498-2505.

[24] R. Siriwardane, H. Tian, D. Miller, G. Richards, T. Simonyi, J. Poston, Evaluation of reaction mechanism of coal–metal oxide interactions in chemical-looping combustion, Combustion and flame, 157 (2010) 2198-2208.

[25] J. Adanez, A. Abad, F. Garcia-Labiano, P. Gayan, L.F. de Diego, Progress in Chemical-Looping Combustion and Reforming technologies, Progress in Energy and Combustion Science, 38 (2012) 215-282.

[26] A. Lyngfelt, C. Linderholm, Chemical-Looping Combustion of Solid Fuels – Status and Recent Progress, Energy Procedia, 114 (2017) 371-386.

[27] E.J. Anthony, Solid Looping Cycles: A New Technology for Coal Conversion, Industrial & Engineering Chemistry Research, 47 (2008) 1747-1754.

[28] H. Gu, L. Shen, J. Xiao, S. Zhang, T. Song, Chemical Looping Combustion of Biomass/Coal with Natural Iron Ore as Oxygen Carrier in a Continuous Reactor, Energy & Fuels, 25 (2011) 446-455.

[29] T. Mendiara, A. Abad, L.F. de Diego, F. García-Labiano, P. Gayán, J. Adánez, Biomass combustion in a CLC system using an iron ore as an oxygen carrier, International Journal of Greenhouse Gas Control, 19 (2013) 322-330.

[30] NIST X-ray Photoelectron Spectroscopy (XPS) Database, in, https://srdata.nist.gov/xps/, 2018.

[31] S. Xie, E. Iglesia, A.T. Bell, Effects of temperature on the Raman spectra and dispersed oxides, The Journal of Physical Chemistry B, 105 (2001) 5144-5152.

[32] Z. Wu, P.C. Stair, S. Rugmini, S.D. Jackson, Raman spectroscopic study of V/θ-Al_2O_3 catalysts: quantification of surface vanadia species and their structure reduced by hydrogen, The Journal of Physical Chemistry C, 111 (2007) 16460-16469.

[33] Z. Wu, M. Li, J. Howe, H.M. Meyer III, S.H. Overbury, Probing defect sites on CeO_2 nanocrystals with well-defined surface planes by Raman spectroscopy and O_2 adsorption, Langmuir, 26 (2010) 16595-16606.

[34] J. Riley, R. Siriwardane, H. Tian, W. Benincosa, J. Poston, Kinetic analysis of the interactions between calcium ferrite and coal char for chemical looping gasification applications: Identifying reduction routes and modes of oxygen transfer, Applied energy, 201 (2017) 94-110.

[35] R. Siriwardane, J. Riley, H. Tian, G. Richards, Chemical looping coal gasification with calcium ferrite and barium ferrite via solid–solid reactions, Applied energy, 165 (2016) 952-966.

[36] J.A. Rodriguez, J.Y. Kim, J.C. Hanson, M. Pérez, A.I. Frenkel, Reduction of CuO in H_2: in situ time-resolved XRD studies, Catalysis Letters, 85 (2003) 247-254.

[37] S. Sivasangar, M. Mastuli, A. Islam, Y. Taufiq-Yap, Screening of modified CaO-based catalysts with a series of dopants for the supercritical water gasification of empty palm fruit bunches to produce hydrogen, RSC Advances, 5 (2015) 36798-36808.

[38] M.-F. Luo, Y.-J. Zhong, X.-X. Yuan, X.-M. Zheng, TPR and TPD studies of $CuOCeO_2$ catalysts for low temperature CO oxidation, Applied Catalysis A: General, 162 (1997) 121-131.

[39] T. Andrushkevich, V. Kaichev, Y.A. Chesalov, A. Saraev, V. Buktiyarov, Selective oxidation of ethanol over vanadia-based catalysts: The influence of support material and reaction mechanism, Catalysis Today, 279 (2017) 95-106.

[40] L. Debbichi, M. Marco de Lucas, J. Pierson, P. Kruger, Vibrational properties of CuO and Cu_4O_3 from first-principles calculations, and Raman and infrared spectroscopy, The Journal of Physical Chemistry C, 116 (2012) 10232-10237.

[41] Z. Wu, S. Dai, S.H. Overbury, Multiwavelength Raman spectroscopic study of silica-supported vanadium oxide catalysts, The Journal of Physical Chemistry C, 114 (2009) 412-422.

[42] Q. Imtiaz, P.M. Abdala, A.M. Kierzkowska, W. Van Beek, S. Schweiger, J.L. Rupp, C.R. Müller, Na^+ doping induced changes in the reduction and charge transport characteristics of Al_2O_3-stabilized, CuO-based materials for CO_2 capture, Physical Chemistry Chemical Physics, 18 (2016) 12278-12288.

[43] B. Tian, Y. Qiao, L. Bai, W. Feng, Y. Jiang, Y. Tian, Pyrolysis behavior and kinetics of the trapped small molecular phase in a lignite, Energy Conversion and Management, 140 (2017) 109-120.

[44] X.-q. Xu, Y.-g. Wang, Z.-d. Chen, X.-j. Chen, H.-y. Zhang, L. Bai, S. Zhang, Variations in char structure and reactivity due to the pyrolysis and in-situ gasification using Shengli brown coal, Journal of Analytical and Applied Pyrolysis, 115 (2015) 233-241.

[45] R. Siriwardane, W. Benincosa, J. Riley, H. Tian, G. Richards, Investigation of reactions in a fluidized bed reactor during chemical looping combustion of coal/steam with copper oxide-iron oxide-alumina oxygen carrier, Applied energy, 183 (2016) 1550-1564.

[46] M.A. Saucedo, J.Y. Lim, J.S. Dennis, S.A. Scott, CO_2-gasification of a lignite coal in the presence of an iron-based oxygen carrier for chemical-looping combustion, Fuel, 127 (2014) 186-201.

[47] Z. Sun, B. Xu, A.H. Rony, S. Toan, S. Chen, K.A. Gasem, H. Adidharma, M. Fan, W. Xiang, Thermogravimetric and kinetics investigation of pine wood pyrolysis catalyzed with alkali-treated CaO/ZSM-5, Energy Conversion and Management, 146 (2017) 182-194.

[48] Z. Zhou, L. Han, O. Nordness, G.M. Bollas, Continuous regime of chemical-looping combustion (CLC) and chemical-looping with oxygen uncoupling (CLOU) reactivity of CuO oxygen carriers, Applied Catalysis B: Environmental, 166 (2015) 132-144.

[49] H. Wang, R.T.K. Baker, Decomposition of methane over a Ni− Cu− MgO catalyst to produce hydrogen and carbon nanofibers, The Journal of Physical Chemistry B, 108 (2004) 20273-20277.

[50] U. Ashik, W.W. Daud, H.F. Abbas, Production of greenhouse gas free hydrogen by thermocatalytic decomposition of methane–A review, Renewable and Sustainable Energy Reviews, 44 (2015) 221-256.

[51] H.F. Abbas, W.W. Daud, Hydrogen production by methane decomposition: a review, International journal of hydrogen energy, 35 (2010) 1160-1190.

[52] A. Cunha, J. Órfão, J. Figueiredo, Methane decomposition on Ni–Cu alloyed Raney-type catalysts, International Journal of hydrogen energy, 34 (2009) 4763-4772.

[53] M.M. Hossain, H.I. de Lasa, Chemical-looping combustion (CLC) for inherent CO_2 separations—a review, Chemical Engineering Science, 63 (2008) 4433-4451.

[54] J. Wang, L. Jin, Y. Zhou, Y. Li, H. Hu, Effect of $Ca(NO_3)_2$ addition in coal on properties of activated carbon for methane decomposition to hydrogen, Fuel processing technology, 176 (2018) 85-90.

[55] Z. Alipour, M. Rezaei, F. Meshkani, Effect of alkaline earth promoters (MgO, CaO, and BaO) on the activity and coke formation of Ni catalysts supported on nanocrystalline Al_2O_3 in dry reforming of methane, Journal of Industrial and Engineering Chemistry, 20 (2014) 2858-2863.

[56] Z. Hou, O. Yokota, T. Tanaka, T. Yashima, Characterization of Ca-promoted Ni/α-Al_2O_3 catalyst for CH_4 reforming with CO_2, Applied Catalysis A: General, 253 (2003) 381-387.

Chapter 3. Impact of Surface Composition of $SrTiO_3$ Catalysts for Oxidative Coupling of Methane (OCM)

Abstract

Due to the increasing production of shale gas (mostly methane), various schemes for direct catalytic methane conversion have regained attention from the research community. One of the routes for upgrading methane is the oxidative coupling of methane (OCM) to C_2 hydrocarbons (C_2H_6 and C_2H_4). Perovskite-type oxide catalysts have shown promising activity and selectivity toward C_2 hydrocarbons. The present work investigates the effect of surface reconstruction (which leads to different surface compositions) of perovskites on the OCM by using $SrTiO_3$ (STO) as a model catalyst. Different surface densities of Sr, between 25 and 96 % according to low energy ion scattering studies (LEIS), were attained via various treatments of STO. UV-Raman and LEIS analysis results are in good agreement on the surface and subsurface composition of the reconstructed STO samples. Temperature programmed desorption (TPD) of ammonia and carbon dioxide was conducted to measure the concentration of acid and base sites, respectively. From hydrogen temperature-programmed reduction (TPR) results, only surface Ti^{4+} reduction occurs and H_2 consumption of the STO samples was found to be the same, which allows correlating their catalytic performances with surface acid-base properties. Steady-state catalytic tests were performed at 600-800 ^oC, and it was found that the enrichment of surface Sr enhances CH_4 conversion, C_2 selectivity and the ratio C_2H_4/C_2H_6 up to a Sr/(Sr+Ti) of 0.66 at the surface and then levels off. Compared to the surface concentration of Sr, the relative concentration of basic sites, base/(base+acid) ratio, are observed as a better descriptor for the catalytic performance of the various STO samples. Extensive kinetic analysis for OCM was attempted with various rate

expressions reported in the literature. However, none of those expressions could accurately describe the performance of all the STO catalysts under this study and thus further study is necessary. This work shows the clear correlation between surface reconstruction, relative basicity/acidity of the surface and the catalytic performance for OCM over perovskite catalysts. The trends here are similar to those observed for methane combustion over the reconstructed STO in a recent work[1]. Overall, it is suggested that tuning surface reconstruction/composition of perovskites can be an effective approach for controlling methane activation and conversions.

3.1 Introduction

Due to the pronounced increase in shale gas (mostly methane) production in recent years, there has been a renewed interest in various schemes for catalytic methane conversion. These schemes can be classified as indirect and direct methods. Indirect conversion of methane to valuable chemicals, e.g. Fischer-Tropsch (FT) synthesis and methanol-to-olefins (MTO), include multiple stages, beginning with syngas production (H_2/CO mixture) from methane. The direct method is defined as those schemes that convert methane to hydrocarbons without undergoing the capital cost of the intermediate syngas step. Therefore, direct methods are expected to be more economical and environmentally friendly than indirect methods. One of the attractive routes for direct upgrading of methane is the oxidative coupling of methane (OCM) to C_2 hydrocarbons (C_2H_6 and C_2H_4), which are valuable intermediates for many chemical industries [2]. However, some difficulties for the commercialization of OCM have been recognized, such as (1) overcoming significant heat emission at high reaction temperature (700-1000 °C); and (2) finding active catalysts with high selectivity to meet the requirement for 30% C_2 yield [3]. Thus, there is a crucial need for efficient catalysts with high C_2 selectivity at significant levels of methane conversion, and long-term thermal stability.

It is widely accepted that ethylene formation through the OCM follows three steps[4]: (1) homolytic cleavage of methane C-H bond occurs on oxygen species of the catalyst surface to generate the methyl radicals; (2) two methyl radicals homogeneously couple in the gas phase to form ethane; (3) ethane is dehydrogenated to ethylene. The main function of the OCM catalyst is to generate methyl radicals [5] and simultaneously to circumvent the overoxidation of radicals at the surface [6]. As for the former function, the surface oxygen ion-radicals (O^- and O_2^{2-}) as the electron deficient species, are reported to be the active centers for methane activation to produce methyl radicals in the OCM reaction.[7-10] For example, the existence of peroxide-like ions has been observed in the perovskite $BaPbO_3$ and $BaBiO_3$ catalysts, [11] resulting in their good catalytic performance in the OCM reaction. These surface oxygen sites have been accepted as the basic centers.[12] Considering the latter function, the lattice oxygen O^{2-} is responsible for completed oxidation of methyl radicals to form CO and CO_2 [7, 8, 13, 14]. The low mobility of lattice oxygen in the OCM catalyst is desired, aiming to avoid the overoxidation of $CH_{3}\cdot$. Therefore, the low oxygen mobility and the presence of surface oxygen ion-radicals, which are acting as the active sites for the methyl radical generation, are essential properties for the OCM catalysts. Numerous efforts have been made to find a high-performance catalyst since the pioneering work by Keller and Bhasin in 1982 [15]. Simple basic oxides (e.g. CaO [16], MgO [17], SrO [18], etc.), and alkali and alkaline metals supported on basic oxides (e.g. Li/MgO [19-21], Na/MgO and Na/CaO [22], etc.) have shown high activity in the OCM reaction. On the other hand, transition metal oxides combined with alkali metals, e.g. Na_2WO_4-Mn/SiO_2 system, are also considered as promising catalysts for the OCM reaching C_2 yields as high as 25 %[23-25].

The thermally and chemically stable perovskite-type oxide catalysts[26, 27] are attractive alternatives. Perovskites oxides have a general formula ABO_3 (A represents a lanthanide, alkali or

alkaline earth and B represents a transition metal). Numerous studies have found that the perovskite-type oxides are a promising OCM catalyst with high activity and selectivity toward C_2 hydrocarbons[28-32]. For instance, Fakhroueian and co-workers[33] reported the C^{2+} selectivity and ethylene yield of a Na-doped $BaSrTiO_3$ perovskite catalyst to be 51% and 24%, respectively. The promising catalytic performance of perovskite catalysts is attributed not only to the segregation of oxygen ion-radicals at the surface, but also the creation of electronic defects and oxygen vacancies (achieved by doping cations in the A and B sublattice)[34]. Some studies have been conducted to investigate the effect of active alkali dopants on catalytic behavior of perovskite oxides under the OCM conditions. D.V. Ivanov[34] synthesized Mg- and Al-doped $SrTiO_3$ and Sr_2TiO_4, obtaining C_2 yields and selectivity up to 25% and 66%, respectively, under optimal OCM reaction conditions. It was found that "layered" perovskite phases $Sr_{2-x}A_xTiO_4$ or $Sr_{3-x}A_xTi_2O_7$ (A=Mg, Al) are destroyed and SrO segregated on the catalyst surface, promoting methane activation. However, fundamental understanding of the effects of perovskite surface reconstruction, independent of the dopant used, on catalytic reactivity/selectivity for OCM is yet to be fully attained.

In addition, the effect of surface reconstruction (which leads to different surface compositions) of perovskites has been recently considered to play an important role in various catalytic process, such as oxygen evolution[35-37], NO_x storage and reduction (NSR)[38], ethanol dehydrogenation[39] etc. Previous work has demonstrated that surface reconstruction is capable of tuning catalytic acid/base properties[39, 40], which are reported to be related to active sites in the OCM reaction[41, 42]. In addition, the effect of surface reconstruction on the rate of methane combustion was investigated by employing a set of $SrTiO_3$ (STO) samples with various surface compositions[1]. Surface Sr concentration is found to be proportional to the rate of

methane combustion. However, the impact of surface reconstruction on the OCM catalysis has, to the best of our knowledge, not yet been reported.

The goal of the present work is to unveil the effect of the surface reconstruction of perovskites using STO as a model material on the OCM reaction. The composition of surface and subsurface layers of STO samples, which were tuned via post-synthesis-treatments (thermal treatment, chemical etching and incipient wetness impregnation), has been characterized via low energy ion scattering (LEIS) in previous work [1], and UV Raman spectroscopy (in the present work). The density and strength of acid/base sites on the STO samples have been characterized via NH_3/CO_2-temperature programmed desorption. Correlations between the surface termination of STO samples, the acid/base sites, and the catalytic performance for the OCM were drawn, providing insights into the structure-performance relationships.

3.2 Experimental Section

3.2.1 Materials

Strontium titanate (STO) and strontium oxide (SrO) were purchased from Sigma-Aldrich. Titanium oxide in the rutile phase was purchased from Alfa Aesar. Argon, Helium, 10% CH_4/Ar, 5% O_2/He, 2% CO_2/Ar, 2% NH_3/He and 4% H_2/Ar were all purchased from Airgas.

3.2.2 Sample Preparation

Five STO samples with different concentrations of Sr at the surface (STO(HNO_3), Sr/STO(HNO_3)-1, Sr/STO(HNO_3)-2, Sr/STO-1, Sr/STO-2) were prepared using chemical etching and incipient wetness impregnation (IWI), as reported in previous publications [1, 39, 40]. Figure 1 is a flowchart for the preparation of these STO samples with surface reconstruction. In brief, to promote the exposure of the Ti-terminated surface, STO(HNO_3) was prepared by

submerging the commercial STO in the 0.2 M aqueous solution of HNO_3 (20 mL of solution per gram of catalyst), the mixture was vigorously stirred for a few seconds and left still for 1 day at room temperature. The catalyst was then washed with deionized water and centrifuged at least four times at 12000 RPM for 10 min. The separated solid was dried at 60 °C overnight in a vacuum oven to obtain STO(HNO_3). Sr/STO(HNO_3)-1 and Sr/STO(HNO_3)-2 were prepared from impregnating Sr on STO(HNO_3), to alter the exposure of the Sr-terminated surface after reconstruction. A prescribed amount of STO(HNO_3) was mixed with an aqueous solution of $Sr(NO_3)_2$ in a glass dish to ensure the solid was homogeneously wetted with the solution. The mixture was placed in the drying oven at 110 °C for approximately 16 h at 110 °C. To promote the exposure of the Sr-terminated surface after reconstruction, Sr/STO-1 and Sr/STO-2 were prepared with loading Sr at the surface of commercial STO by employing the same above-mentioned IWI method. All samples were calcined at 750 °C for at least 5h and then subjected to following analyses and catalytic performance tests.

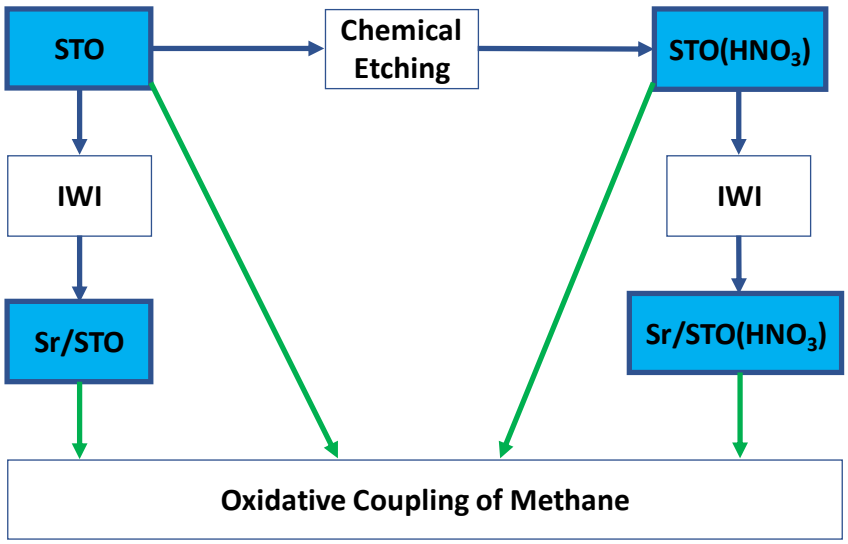

Figure 1. Process Sequences for the preparation of STO catalysts.

In previous study[1], it was found that all prepared samples have similar Brunauer-Emmett-Teller (BET) surface area (18.8-22.2 m^2/g). In addition, all samples presented the same

STO perovskite crystal structure without detectable additional phases via XRD. For the reference sample, the BET surface area for SrO/TiO_2 is 2.8 m^2/g, and the SrO content on this sample is 3.55 $mg/(m^2$,catalyst). The particle size for Sr/TiO_2 is c.a.40nm, calculated with XRD data using the Scherrer equation.

3.2.3 Low Energy Ion Scattering (LEIS) Analysis

LEIS measurements were performed at Lehigh University in an IONTOF Qtac100 spectrometer (ION-TOF GmbH, Münster, Germany) to determine the composition of the outmost atomic layer. Charge neutralization was invoked during spectra acquisition and sputtering. More details of LEIS measurement can be found in previous work[1]. Sr-composition, namely Sr/(Sr+Ti), reported in this work is calculated by assuming that the Sr-composition is 50 % at 5 nm depth for a commercial STO sample without any pretreatment.

3.2.4 Raman Spectroscopy

Raman spectroscopy was performed on a multiwavelength Raman system[43] at sub-ambient temperature(-75°C) since the STO Raman signal intensity is enhanced at low temperature[44]. Raman spectral collection was performed with 325 and 442 nm laser excitations, which are ultraviolet- and visible-laser excitations, respectively. Raman scattering was collected via a customized ellipsoidal mirror and directed by a fiber optic bundle to the spectrograph stage of a triple Raman spectrometer (Princeton Instruments Acton Trivista 555). Edge filters (Semrock) were used in front of the UV-vis fiber optic bundle (Princeton Instruments) to block the laser irradiation. The 325 (<5 mW at sample) and 442 nm (<10 mW at sample) excitations are from a HeCd laser (Melles Griot). A UV-enhanced liquid N_2-cooled CCD detector (Princeton Instruments) was employed for signal detection. The Raman reactor (Linkam THMS 600) sits on

an XY stage (Prior Scientific, OptiScan XY system). Prior to Raman characterization, all STO samples were pretreated in air in the muffle oven at 850 °C for 5 h. The samples were then transferred to the Raman reactor and cooled down to the measurement temperature under a constant Ar flow (30mL/min).

3.2.5 Temperature Programmed Desorption of Ammonia (NH_3-TPD) and Carbon Dioxide (CO_2-TPD)

The temperature programmed desorption of ammonia (NH_3-TPD) and carbon dioxide (CO_2-TPD) was conducted to evaluate the comparative strength and quantify the concentration of surface acid and base sites of the samples under study. An Altamira Instruments system (AMI-300) coupled with an on-line mass spectrometer (Omnistar GSD-301, Pfeiffer Vacuum) was used to perform the TPD measurements. Prior to a TPD measurement, 20 mg of a STO sample was loaded into a U-tube quartz reactor and pretreated at 850 °C for 5 h under 50 mL/min of 5% O_2/He. The temperature was increased from 25 to 850 °C at a heating rate of 20 °C/min. After pretreatment, the sample was cooled to 150 °C (for ammonia adsorption) or 30 °C (for carbon dioxide adsorption) under helium. Prior to desorption, the catalyst was exposed to 30 mL/min of 2% NH_3/He for 2 h. Then, the sample was purged with 30 mL/min of He for 2 h to remove physisorbed NH_3. Afterwards, the temperature of the sample was ramped from 150 to 800 °C at a rate of 5 °C/min, and the NH_3-TPD profile was recorded using the mass spectrometer. CO_2-TPD profiles were collected using the same procedure as the NH_3-TPD. 2% CO_2/Ar was employed to perform the CO_2 adsorption/desorption cycle to evaluate the density of the basic sites for the STO catalysts.

3.2.6 Temperature Programmed Reduction with Hydrogen (H_2-TPR)

The reducibility of the STO samples was evaluated via temperature-programmed reduction with hydrogen (H_2-TPR). These measurements were done in an Altamira Instruments AMI-300 system, coupled with an online mass spectrometer (Omnistar GSD-301, Pfeiffer). Before the reduction, 20 mg of the STO catalyst were treated at 850 °C for 5 h under 50 mL/min of 5% O_2/He. Then, the catalyst temperature was cooled to 50 °C under He. Once the temperature of the catalyst bed reached 50 °C, the flow through the bed was switched to 30 mL/min of 4%H_2/Ar. After exposure to 4% H_2/Ar for 2 h, the temperature of the catalyst sample was ramped from 50 °C to 800 °C at a rate of 5 °C/min, and the H_2-TPR profile was recorded using the online mass spectrometer.

3.2.7 Steady-State Kinetic Measurement

The OCM reaction was performed in the AMI-300 system. 5 mg STO or SrO sample (particle sizes both are 177-250 μm) was diluted in quartz sand (177-250 μm) to minimize channeling and local temperature differences. The quartz-to-catalyst mass ratio was approximately 60:1. The catalyst bed was placed inside a quartz u-tube (10 mm inner diameter) and held in place by quartz wool at both ends of the bed. A K-type thermocouple was placed inside the reactor to monitor the temperature of the catalyst bed. Before kinetic measurements, each sample was pretreated under 50 mL/min of 5% O_2/He at 850 °C for 5 h. Steady-state conversions and selectivity do not change during at least 2 h time-on-stream, suggesting that the surface does not reconstruct further after the initial activation in O_2 at high temperature. The feed used to perform the OCM reaction consisted of 25 mL/min of 10% CH_4/Ar, 10 mL/min of 5% O_2/He, and 15 mL/min of He as balance gas. Thus, the methane to oxygen ratio was 5. Products were analyzed by an on-line gas chromatograph (Agilent Technologies, 6890N) with HayeSep-N and Molecular

Sieve 13X columns using both thermal conductivity and flame ionization detectors. The GC response factor was calibrated for all compounds. All lines were heated to 120 °C to avoid water condensation. All the kinetic data were measured under differential conditions (methane conversion less than 6%) at temperatures of 650 °C. A blank test using the same U-tube reactor without catalyst was carried out and showed negligible methane conversion and C_2 yield (CH_4 conversion of 0.39%, 0.94%, 2.3%, and C_2 yield of 0%, 0%, 0.04% at 600, 700, 800 °C, respectively). All data points are averaged values of 3 to 5 GC-runs after the reaction reached steady state. The error for each data point is less than 5%, and the averaged values are presented below. The CH_4 conversion (%), C_2 hydrocarbon selectivity (%), C_2 hydrocarbon yield (%), CO_x selectivity (%), CO_x yield (%) and ethylene/ethane ratio (mol/mol) were defined as follows:

$$Methane\ conversion\ (\%) = \frac{moles\ of\ methane\ reacted}{moles\ of\ methane\ in\ feed} \times 100 \quad \text{(Eq3.2-1)}$$

$$C_2\ selectivity\ (\%) = \frac{2(moles\ of\ ethane\ and\ ethlene\ formed)}{moles\ of\ methane\ reacted} \times 100 \quad \text{(Eq3.2-2)}$$

$$C_2\ yield\ (\%) = methane\ conversion\ (\%) \times C_2\ selectivity\ (\%) \times \frac{1}{100} \quad \text{(Eq3.2-3)}$$

$$CO_x\ selectivity\ (\%) = \frac{moles\ of\ CO\ or\ CO_2\ formed}{moles\ of\ methane\ reacted} \times 100 \quad \text{(Eq3.2-4)}$$

$$CO_x\ yield\ (\%) = methane\ conversion\ (\%) \times CO_x\ selectivity\ (\%) \times \frac{1}{100} \quad \text{(Eq3.2-5)}$$

$$C_2H_4/C_2H_6\ (mol/mol) = \frac{moles\ of\ ethylene\ produced}{moles\ of\ ethane\ produced} \quad \text{(Eq3.2-6)}$$

3.3 Results and Discussion

3.3.1 Surface Composition

LEIS was used to analyze the composition at the surface of the STO samples since it is considered as a particularly suitable technique to probe the top atomic monolayer of a material

(escape depth of ~0.3 nm) with a sensitivity on the order of 0.1 at.% [45-47]. Sr-compositions (Sr/(Sr+Ti)) of the outermost surface layer of STO samples are presented in Figure 2. The Sr/(Sr+Ti) value for the STO(HNO_3) sample is 0.25, indicating the STO(HNO_3) surface is enriched with Ti cations. As reported previously, chemical etching with HNO_3 exposed Ti cations at the surface (as single and double layers)[40]. Although Sr-doping increases the surface composition of Sr for Sr/STO(HNO_3)-1 and Sr/STO(HNO_3)-2 samples (whose Sr/(Sr+Ti) values are larger than that of STO(HNO_3) sample), surface Ti enrichment is also observed for Sr/STO(HNO_3)-1 sample since its Sr/(Sr+Ti) value is 0.28, namely 72% of its surface is covered by Ti cations. For the commercial STO sample, Sr/(Sr+Ti) at the surface is 0.66, i.e. the Sr/Ti ratio is about 2. The impregnation of Sr significantly increases the Sr termination on the top layer of Sr/STO-1 and Sr/STO-2 samples, whose Sr/(Sr+Ti) are 0.92 and 0.96, respectively. To sum up, chemical etching and IWI methods effectively tuned the surface compositions of the STO perovskite. The concentration of surface Sr increases in the order: STO(HNO_3) < Sr/STO(HNO_3)-1 < Sr/STO(HNO_3)-2 < STO < Sr/STO-1 < Sr/STO-2. The ratio of base/acid sites (quantified by NH_3-TPD and CO_2-TPD to be shown in a later section) is also tuned by the surface compositions of the samples (see Figure 2). This base/acid ratio correlates with the surface Sr concentration, and the details about this relationship will be discussed in Section 3.3.3.

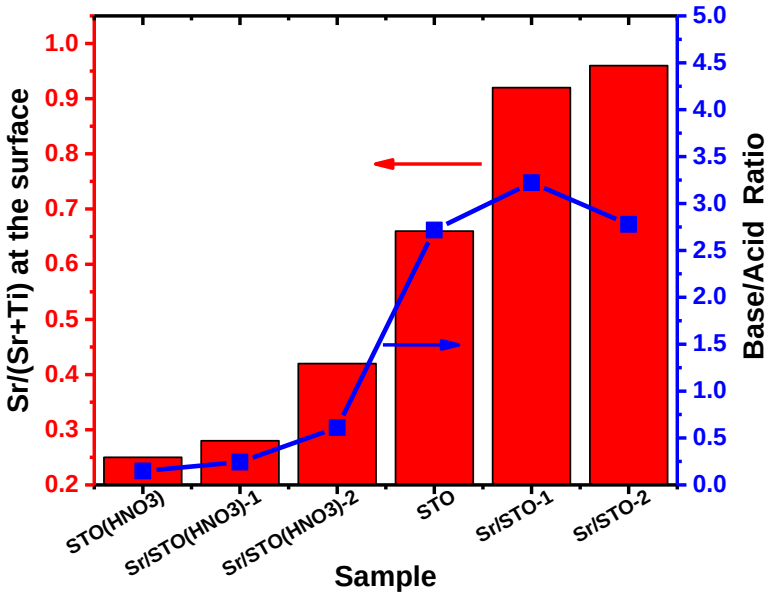

Figure 2. Sr-compositions (Sr/(Sr+Ti)) of outermost surface layer and ratio of base/acid site of STO samples.

The evidence for surface reconstruction of the STO perovskites upon high temperature treatment was collected via LEIS. Significant differences in the segregation of cations at the surface were observed before and after the *in situ* O_2 treatment (the treatment in the O_2 atmosphere at high temperatures attempts to reproduce approximately the OCM reaction conditions, given the limitations of the technique). The compositions before and after reconstruction for commercial STO and STO(HNO_3) samples are summarized in Table 1.

Table 1. Surface composition from LEIS analysis with in situ heat treatment in O_2 atmosphere at 500°C for 30min.

Catalyst	Sr/(Sr+Ti) at the surface	
	Before Treatment	After Treatment
STO	0.35	0.66
STO(HNO_3)	0.20	0.25

3.3.2 Raman Spectra as Function of Laser Excitations and Surface Composition

The commercial STO sample was selected for the comparison of the Raman spectra from UV- and visible- laser excitations. Figure 3(a) shows the Raman spectra of commercial STO

excited at 325 (UV-Raman spectrum) and 442 nm (visible Raman spectrum). All the peaks assignments are listed in Table 2. Excitation by the two lasers at different wavelengths gives Raman spectra with similar peak positions but different relative intensity. The relative intensities of the peaks at 795, 1038, 1292 and 1618 cm^{-1} to that of the peak at 308 cm^{-1} are greatly enhanced with the 325-nm excitation, due to the resonance enhancement effect [48, 49].

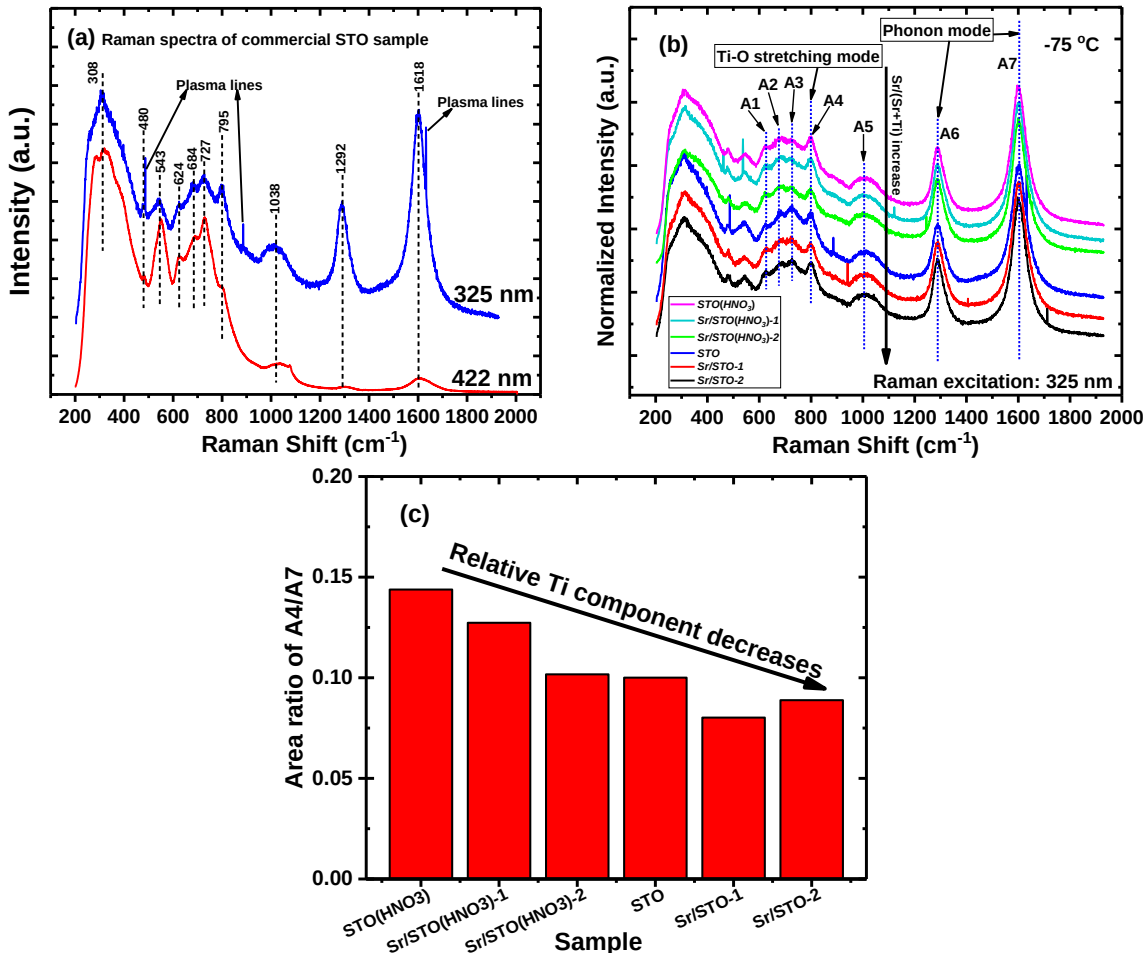

Figure 3. (a) Raman spectra of commercial STO excited at 325 and 442 nm. (b) 325-nm excited Raman spectra of STO samples with surface reconstruction. (c) Ratio of I_{A4}/I_{A7} values for different STO samples.

Table 2. Raman peak assignments for STO samples.

Peak Position (cm^{-1})	Assignment	Reference
308	TO_2+TA, TO_2+TO_1, TO_4-TO_2	[50]
480	LO_3	[51]
543	TO_4	[51]
624	TO_4+TA, TO_4+TO_1	[50]
684	$2TO_3$	[50]
727	TO_4+TO_2	[50]
795	LO_4, Ti-O stretching mode	[52, 53]
1038	$2LO_2$, $2TO_4$	[50]
1292	LO_4+LO_2	[50]
1618	$2LO_4$	[50]

In its diffuse reflectance UV-vis spectrum in Figure 4, STO shows strong electronic absorption in the region below 400 nm, whereas it exhibits little absorption in the visible region. As a result, compared to the conventional visible Raman spectroscopy, UV-excitation Raman has a shorter penetration depth, preventing light from entering the substrate or deep bulk[44, 49]. Therefore, the UV excitation at 325 nm was utilized for studying the composition in the surface sublayers in the STO samples. Indeed the 325 nm laser was found to have a penetration depth of ~9 nm[54] of STO, a relatively small portion of the outside of the STO particles with an average particle size of ~100 nm[39].

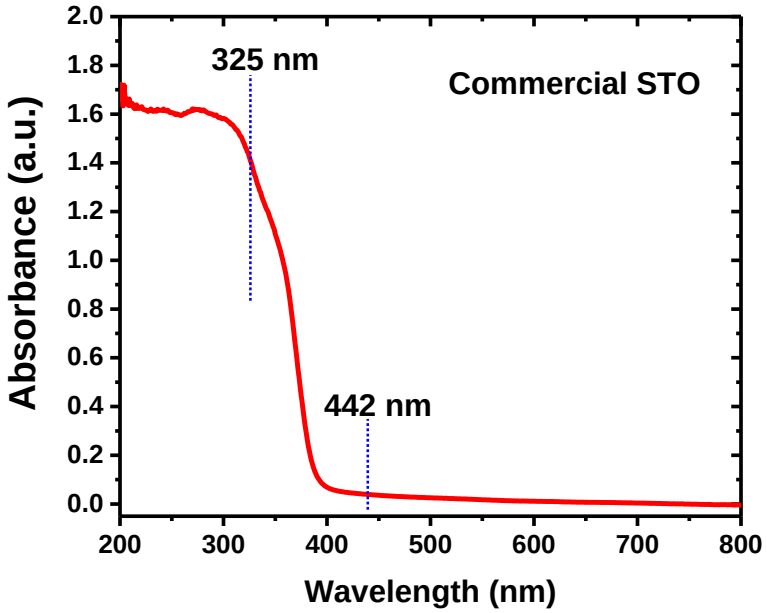

Figure 4. UV-vis diffuse reflectance spectrum of the commercial STO sample.

Figure 3(b) gives the 325 nm excited Raman spectra of various STO samples and the corresponding Raman spectra from 442 nm excitation are shown in Figure 5.

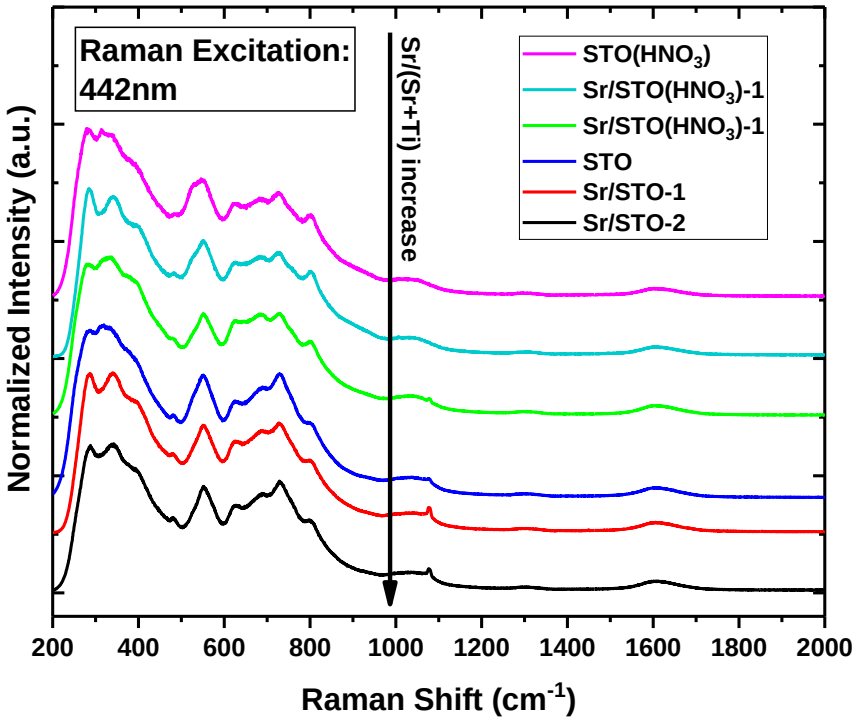

Figure 5. Raman spectra of all STO samples with excitation at 442 nm.

Since the three overtone bands at 1038, 1292 and 1618 cm^{-1} yield consistent values for the phonon energies of the LO_4 and LO_2 modes[50], their intensities remain constant for all the samples and normalization was conducted regarding the band at 1618 cm^{-1} as the reference. Each of the acquired spectra in the region between 600-1900 cm^{-1} were deconvoluted to 7 Gaussian bands A1-A7. A typical example of the spectral deconvolution of the Raman spectra of the commercial STO sample is shown in Figure 6. Coefficient of determination (R^2) of curve deconvolution is more than 0.98 for all samples ($0 \leq R^2 \leq 1$). All band assignments for A1-A7 can be found in Table 2. Especially, the A4 peak at 795 cm^{-1} is assigned to the Ti-O stretching mode [53] and A7 peak at 1618 cm^{-1} is assigned to the combination of LO_4+LO_2 mode. The relative amount of Ti in the sublayer of STO samples can be described by the area ratios of the A4 band to A7 band (I_{A4}/I_{A7}). Figure 3(c) exhibits the I_{A4}/I_{A7} values for different STO samples. The I_{A4}/I_{A7} ratio, namely, the relative amount of the Ti in the STO sublayer, decreases with the increase of Sr/(Sr+Ti) detected from LEIS analysis. UV-Raman and LEIS analysis results are in good agreement on the surface and subsurface composition of reconstructed STO samples.

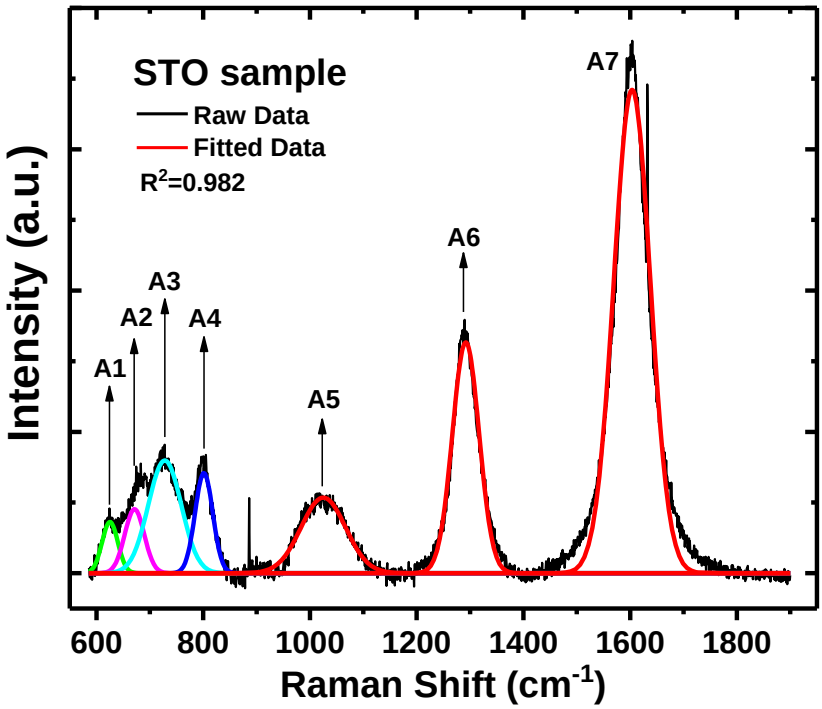

Figure 6. Spectral deconvolution of the Raman spectrum of the commercial STO sample.

In situ Raman was also attempted to probe any possible surface reconstruction of the STO samples during the OCM reaction. Unfortunately, some featured peaks (i.e. peaks at 684, 727, 795 cm^{-1} etc.) for STO samples become weak at such high temperature (600-800 °C) due to thermal effects.[55] Also, the oxygen ion-radicals expected in the range of 800-1500 cm^{-1} are not found in the *in situ* Raman spectra after reaction at the high temperatures shown in the Figure 7.

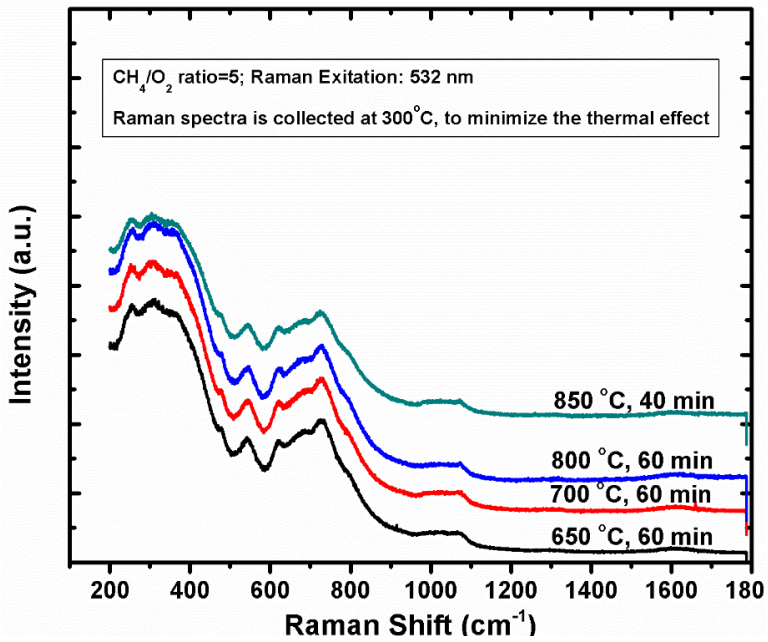

Figure 7. Raman spectra for commercial STO sample under OCM conditions at different temperatures and reaction time.

3.3.3 Acid-base Properties Investigation

It is widely accepted that the acid/base properties of the catalysts, especially the concentration of surface base sites, play an important role in the formation of C_2 hydrocarbons in the OCM reaction. Florica *et al.*[41] claimed that the higher the catalyst basicity, the better the efficiency for selectively converting methane to C_2 products. Acid/base catalytic properties of perovskites have been studied with multiple techniques and these studies were reviewed recently[12]. It is accepted that the acid/base catalytic performance can be influenced by some factors, such as density, strength and type of adsorption sites, the surface reconstruction (both surface concentration and surface structure) under reaction conditions and the facet exposed. In recent work [39], the acid-base properties were found to relate with the surface composition which can be tuned by surface reconstruction of shape-controlled STO nanocrystals. In this work, the NH_3-TPD measurements were performed to analyze the acid-site strength distribution and concentration on the STO surface. As shown in Figure. 8(a), three desorption peaks Q1, Q2, Q3

were obtained by conducting deconvolution at low temperature around 190 and 250 °C and high temperature around 500 °C. The low temperature peaks (Q1 and Q2) correspond to weak acid sites, whereas the higher temperature peak Q3 is related to strong acid sites. It is observed that surface-Sr-rich samples (Sr/(Sr+Ti) > 0.5), i.e. STO, Sr/STO-1, Sr/STO-2, only possess a weak Q2 peak at low temperature; in contrast, surface-Ti-rich samples (i.e. STO(HNO_3), Sr/STO(HNO_3)-1, Sr/STO(HNO_3)-2) exhibit both Q1 and Q2 low temperature peaks. Moreover, the increase of Ti at the surface further increases the strength of acid sites by shifting the corresponding high temperature desorption peak Q3 from 450 to 550 °C. The amount of NH_3 adsorbed represents the surface acid site concentration of the catalysts and is summarized in Table 3. The acid site density increases in the order: Sr/STO-2 < Sr/STO-1 < STO < STO(HNO_3)-2 < Sr/STO(HNO_3)-1 < STO(HNO_3).

Table 3. Acid and base site density of catalyst

Catalyst ID	Acid site (μmol/g)	Base site (μmol/g)	Ratio of base/acid	Ratio of base/(base+acid)
STO(HNO_3)	71.32	10.58	0.15	0.13
Sr/STO(HNO_3)-1	71.37	17.33	0.24	0.20
Sr/STO(HNO_3)-2	62.00	37.53	0.61	0.38
STO	54.05	146.82	2.72	0.73
Sr/STO-1	48.40	155.92	3.22	0.76
Sr/STO-2	52.36	145.46	2.78	0.74
Sr/TiO_2	51.77	1.13	0.02	0.02

The basicity of STO catalysts was measured by CO_2-TPD as shown in Figure 8(b). There are three peaks in the CO_2-TPD profile, labelled P1, P2 and P3. P1 and P2 were assigned to the weak and strong CO_2 desorption at the temperature < 100 and 300 °C, respectively, which are due to the alkalinity of strontium[56]. P3 appears at 700 °C for the Sr/STO samples, which is caused by the decomposition of surface carbonate ($SrCO_3 \rightarrow SrO + CO_2$)[57, 58]. Surface-Sr-rich STO samples possess P1, P2 and P3 basic sites; whereas surface-Ti-rich samples only have the P1

weakly basic sites, except that STO(HNO_3)-2 shows small amount of P2 strong basic sites. The amount of basic sites for the STO samples was also calculated and summarized in Table 3. The total amount of basic sites increases with the surface Sr concentration. The plot in Figure 9 suggests the correlation of base-site density with acid-site density on STO samples, where the base site concentration is inversely proportional to that of the acid sites.

The catalyst performance was evaluated over the temperature range of 600-800 °C and the product CO_2 can form carbonate species on the STO surface. From the CO_2-TPD profile, it is found that most basic sites (locating on P1 and P2 peaks) on the STO samples are available to reactants when the temperature is higher than 600 °C. Furthermore, when reaction temperature is higher than 700 °C, the basic sites corresponding to P3 are exposed and can contribute to the formation of C_2. Reactivity trends are similar in the temperature range studied (600-800 °C); and therefore, we conclude that the basic sites corresponding to P3 at reaction temperatures above 700 °C do not have significant impact on the OCM performances over the STO samples.

The surface ratio of base/acid sites and base/(base+acid) are listed in the Table 3. From Figure 2, the base/acid ratio trend in the STO samples is in good agreement with the LEIS results, indicating that the surface Sr enrichment of the catalysts is proportional to the density of basic sites.

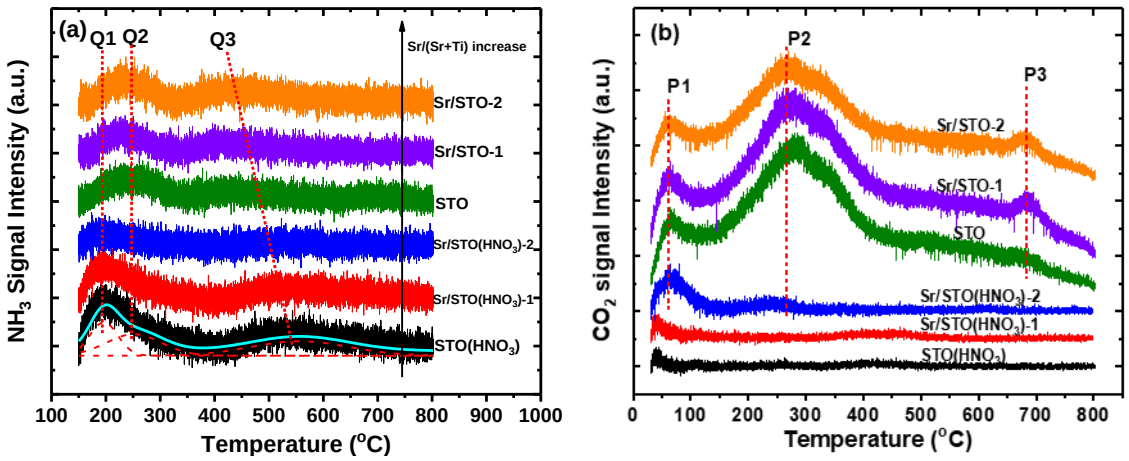

Figure 8. (a) NH_3-TPD profiles and (b) CO_2-TPD profiles of STO samples.

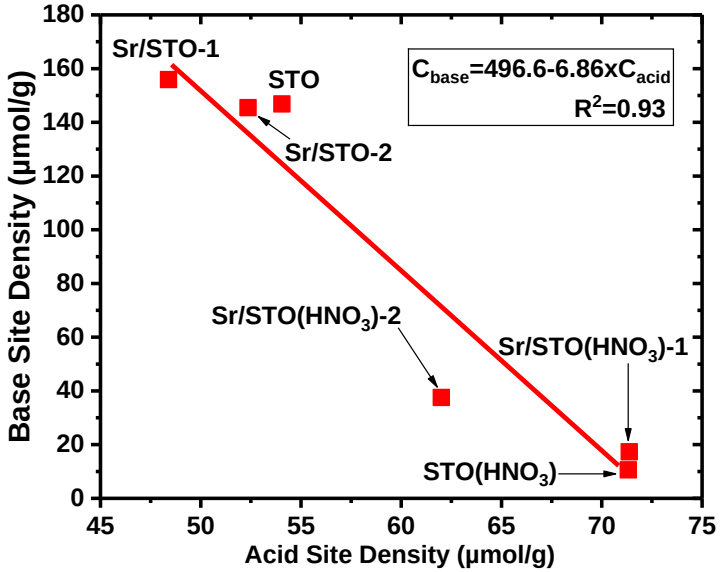

Figure 9. Correlation of base-site density with acid-site density on STO samples.

3.3.4 H_2-TPR Analysis

To study the dependence of the reducibility of the STO samples with surface termination, TPR tests were performed in 30 mL/min 4% H_2/He flow. The H_2-TPR profiles are presented in Figure 10, illustrating that all STO samples show one main peak with a maximum at 500 °C. This peak was assigned to the reduction of the B-site Ti^{4+} to Ti^{3+} of perovskites [59]. The H_2 uptake for

all STO samples was calculated and summarized in Table 4. All samples showed similar H_2 consumption (584-595 μmol/g); therefore, the surface composition has negligible effect on the reducibility of STO samples.

Table 4. H_2 consumption of STO samples during H_2-TPR

Catalyst ID	H_2 consumption (μmol/g)
STO(HNO_3)	595.9
Sr/STO(HNO_3)-1	592.9
Sr/STO(HNO_3)-2	581.6
STO	591.3
Sr/STO-1	586.4
Sr/STO-2	584.0

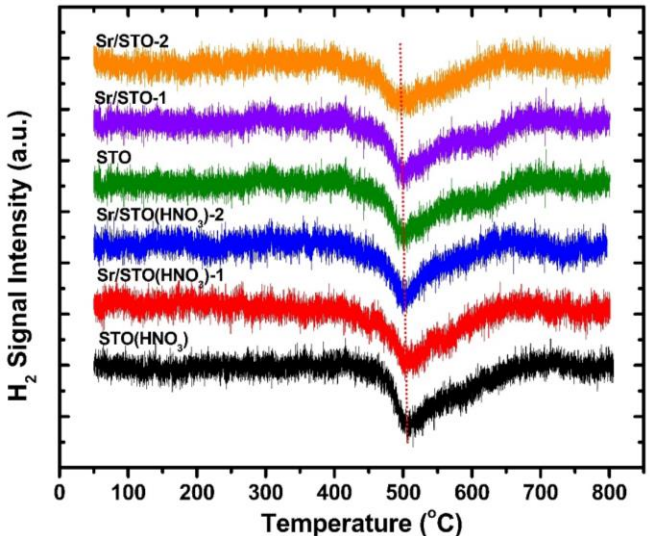

Figure 10. H_2-TPR profiles of STO samples.

3.3.5 Catalytic Performance

When tested for the OCM reaction, the STO catalysts have shown promising activity and selectivity toward C_2 hydrocarbons, i.e. C_2 yield can reach 10.5% for 30 mg STO at 800 ~ 850 °C at $CH_4/O_2 = 5$ (See Figure 11). The yield, upon further catalyst optimization, has the potential to meet the industrial requirement, which is 30% for combined C_2 yield [10, 60]. For example, D. V. Ivanov and co-workers[34] reported the C_2 yield in the OCM reaction for Mg-/Al-doped STO and

Sr_2TiO_4 can achieve as high as 25% at 850-900 °C, thus can be comparable to that found for the-state-of-the-art OCM catalysts, such as Na-doped $Ba_{0.5}Sr_{0.5}TiO_3$ (24 % C_2 yield)[33], and Na-W-Mn/SiO_2 (29 % C_2 yield)[55], among others. In addition, excellent regenerability of the STO catalysts was validated in the present work. The spent STO after the OCM reaction at 850 °C for 3 h was exposed to oxygen (5% O_2/He, 850 °C, 5h) for regeneration. The regenerated STO exhibited unchanged catalytic activity as shown in Figure 11.

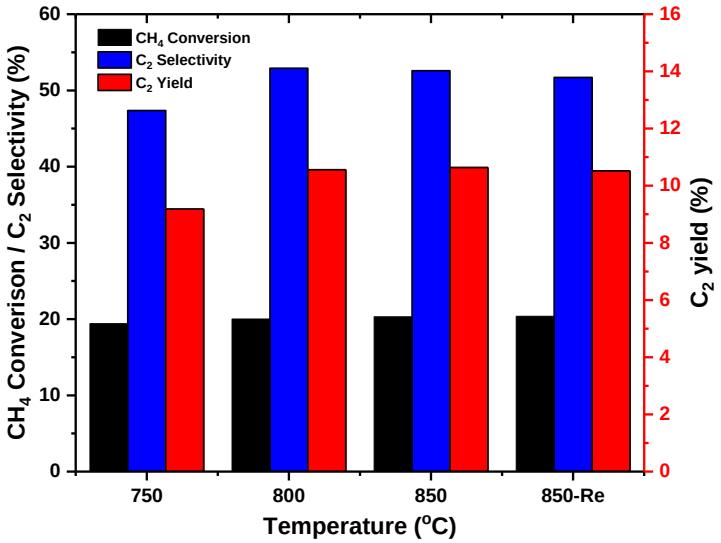

Figure 11. Regenerability test of commercial STO sample for OCM reaction.

Note: CH_4 conversion, C_2 selectivity and C_2 yield for 30mg commercial STO with CH_4/O_2 feeding ratio 5 at different temperatures in OCM reaction. 850-Re represents that spent STO sample was regenerated (in 5% O_2/He for 5h at 850 °C) after OCM reaction (850 °C for 3h), then employed to OCM reaction in the same condition at 850 °C.

To study the OCM kinetics, the STO catalysts were tested for the OCM reaction with CH_4/O_2=5 over the 600-800 °C temperature range with CH_4 conversion below 10%. The variation of CH_4 consumption rate and product (CO_2, CO, C_2H_4 and C_2H_6) yields with respect to the composition of the top catalyst surface at different temperatures are presented in Figure 12(a)-(e). Although the maximum C_2 (C_2H_4+C_2H_6) yield in present experimental condition is 5.3% (Figure 12 (d) and (e)), the fundamental understanding of the effects of perovskite surface composition can be investigated. The methane consumption rate and product yields are found proportional to

the concentration of Sr at the surface for the range of temperature studied up to Sr/(Sr+Ti) ratio of 0.66, beyond which the CH_4 conversion and yields tend to level off. The trends are similar to the trend observed for methane combustion over these STO samples in recent work (See Figure 13), i.e., similar enhancement of CH_4 conversion is present with surface Sr concentration of STO in both methane combustion and the OCM reaction. Apparently, the surface Sr concentration can be highlighted as a universal descriptor for methane activation, independent of the reaction (OCM or combustion). As a control test, the OCM reaction was conducted on a Sr/TiO_2 catalyst and no activity was observed (CH_4 conversion of 0.65%, 0.84%, 2.45% at 600, 700, 800 °C, respectively, similar to the blank test results). From recent report[1], the Sr/TiO_2 sample was synthesized by impregnating Sr on the surface of rutile TiO_2. XRD results indicated Sr does not diffuse into the TiO_2 lattice and its theoretical surface Sr/(Sr+Ti) value is 1. This prominent reactivity difference between Sr-doped TiO_2 and impregnated STO indicates that the arrangement of cations in the bulk, related to the crystal structure, is critical for the OCM reaction. From Table 3, the acid-site density of Sr/TiO_2 is comparable to those of perovskite STO with surface reconstruction (48.40-71.37 μmol/g). In contrast, the base-site density of Sr/TiO_2 is only 1.13 μmol/g, which is much less than those of perovskite STO samples (10.58-155.92 μmol/g), resulting in poor OCM activity. Therefore, it can be concluded that the ABO_3 crystal structure is necessary for the existence and stabilization of basic sites on the catalyst surface.

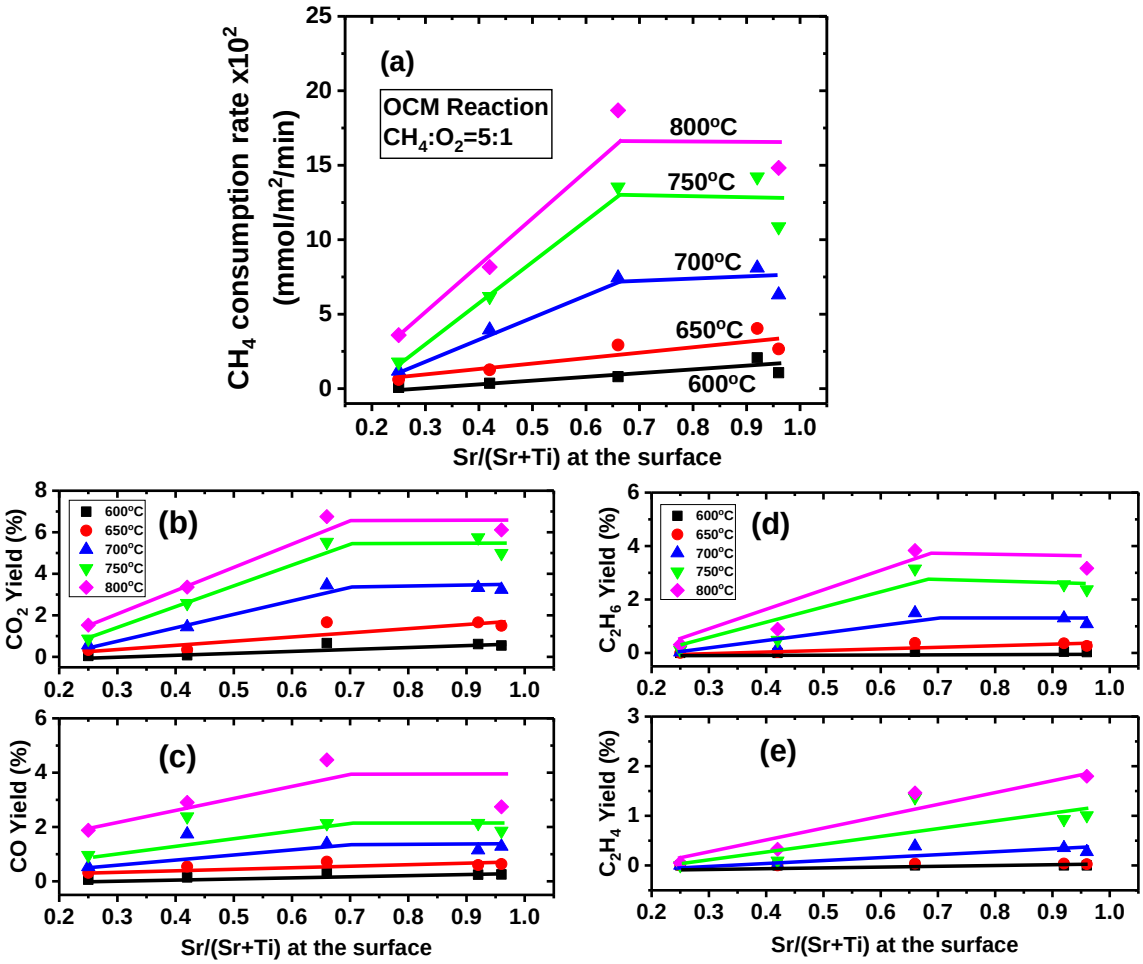

Figure 12. (a) CH_4 conversion, (b) CO_2 yield, (c) CO yield, (d) C_2H_6 yield and (e) C_2H_4 yield with respect to the composition of the top surface of various STO samples at different catalyst bed temperatures (600, 650, 700, 750, 800°C) for OCM reaction with conditions in present work.

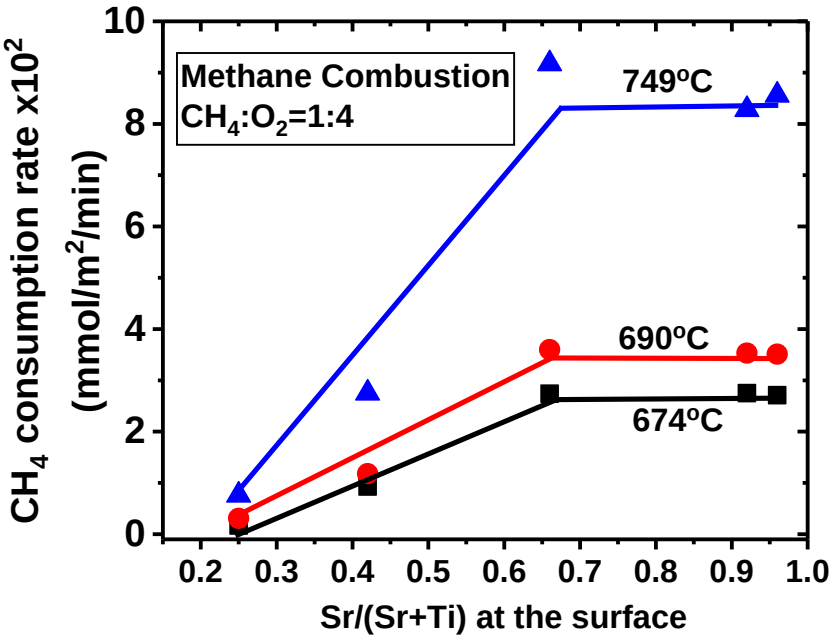

Figure 13. Rate of CH_4 conversion versus composition of outermost atomic layer of various STO samples at different temperatures for methane combustion.

Note: Reaction conditions for methane combustion: 30 mg of catalyst, 1.4 atm, feed consists of 51 mL/min 1.1% CH_4, 4.5% O_2, balance Ar + He. Reprinted with permission from (F. Polo-Garzon, V. Fung, X. Liu, Z.D. Hood, E.E. Bickel, L. Bai, H. Tian, G.S. Foo, M. Chi, D.-e. Jiang, Z. Wu, Understanding the Impact of Surface Reconstruction of Perovskite Catalysts on CH4 Activation and Combustion, ACS Catalysis, (2018)). Copyright (2018) American Chemical Society.

Figure 14(a) and (b) show the ratio of C_2/CO_x and ethylene/ethane yield, respectively, at different temperatures as a function of top surface composition. C_2 selectivity along with ethylene/ethane ratio increased with both temperature and Sr/(Sr+Ti) at the surface. The surface basic sites are reported to be responsible for the formation of C_2.[41, 42]. From previous work [1], the homolytic dehydrogenation of methane, which would create free methyl radicals, presents the lowest activation energy (0.32 eV) on the Sr-terminated step surface, compared with Ti-terminated step surface and other heterolytic C-H bond cleavage over STO surface. Subsequently, more C_2H_6 is formed via the combination of methyl radicals in the gas phase. Then, the dehydrogenation of concentrated C_2H_6 is promoted and finally more C_2H_4 is generated in the gas phase. In short, a clear connection between STO surface composition and the OCM catalytic performance is expressed, i.e.,

Sr concentration at the surface is shown to be an indicator for the activity and selectivity in the OCM reaction.

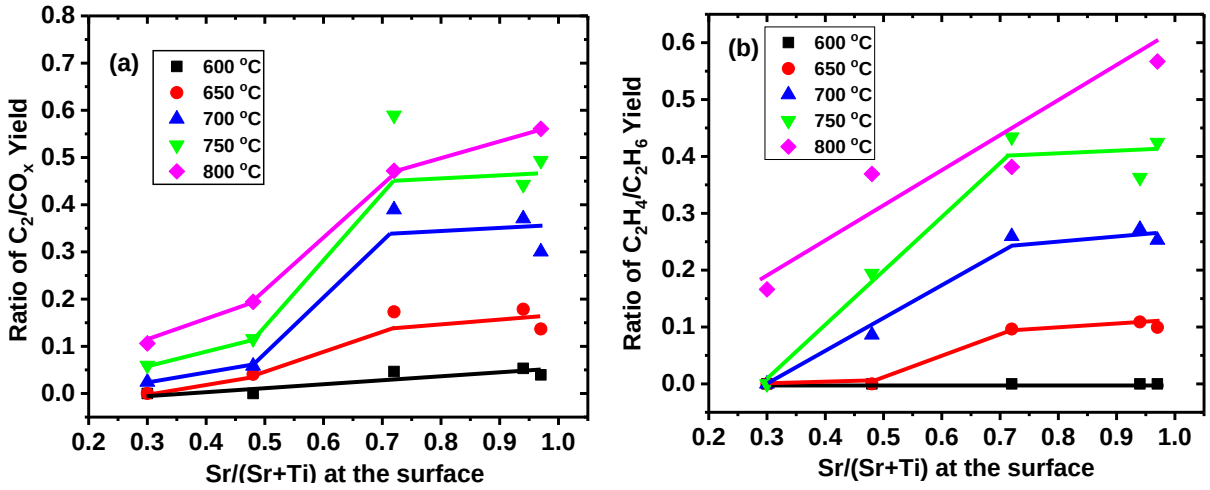

Figure 14. (a) Ratio of C_2/CO_x yield and (b) ratio of ethylene/ethane yield as function of top surface composition at different catalyst bed temperatures over various STO samples.

To calculate the apparent activation energies for different STO samples, the reaction rates under differential conditions (CH_4 conversion < 10%) are fitted to power law model[61] with a simple rate expression:

$$rate = k(P_{CH_4})^a(P_{O_2})^b \qquad \text{(Eq3.3-1)}$$

with $k = A'\exp(-\frac{E_a}{RT})$

Where the A' is the pre-exponential factor in the Arrhenius equation, Ea is the apparent activation energy, R is the gas constant with the value of 8.314×10^{-3} kJ/K/mol, T is the reaction temperature.

Thus, the Eq3.3-1 can be rewritten as:

$$rate = A'\exp(-\frac{E_a}{RT})(P_{CH_4})^a(P_{O_2})^b \quad \text{(Eq3.3-2)} \quad \text{or,}$$

$$rate = A \cdot \exp(-B \cdot (\frac{1000}{T})) \quad \text{(Eq3.3-3)}$$

Where, A=A'$(P_{CH4})^a$ $(P_{O2})^b$, B=Ea/(1000×R). By plotting the ln(rate) against the (1000/T), A and B can be derived from the intercept and slope of the plots, respectively. Hence, the Ea can be solved from B values in (Eq-S3), which are shown in Table 5. The calculated Ea values are listed in the Table 6 in the following part.

Table 5. Fitted B values according to Eq3.3-3.

Sample	Fitted B values			
	CH_4 consumption	CO formation	CO_2 formation	C_2 formation
STO(HNO_3)	16.388±2.666	15.209±0.950	14.952±1.374	22.09±3.100
Sr/STO(HNO_3)-2	14.902±1.957	14.274±0.407	18.08±0.831	23.745±3.176
STO	14.839±1.560	12.04±1.842	11.087±2.671	22.746±0.394
Sr/STO-1	14.171±1.672	12.792±0.568	13.251±1.176	36.016±3.554
Sr/STO-2	12.603±0.985	11.045±2.405	11.437±2.450	23.899±1.989

The Arrhenius plots for CH_4 consumption with various catalysts are presented in Figure 15(a). The apparent activation energies (Ea) for CH_4 consumption, CO, CO_2 and C_2 formation are shown in Table 6. Moreover, Figure 16 shows the Arrhenius plots for CO, CO_2 and C_2 formation rates with different catalysts. The relationship between apparent activation energies with surface Sr concentration is plotted in Figure. 15(b). The Ea values remained constant with varying surface Sr concentration for the STO samples, indicating the reaction pathway for the OCM reaction on STO is unchanged. It is reported in precious publication[1] that the rate-determining step (RDS) for the combustion of methane over STO is involved in the dehydrogenation of CH_4 rather than the dissociation of O_2, confirmed by kinetic isotopic experiments. Since the OCM rate trends are similar to that for methane combustion over these STO samples, it is reasonable to assume the

RDS for OCM reaction is also related to the C-H bond breaking of CH_4. The difference in the rate of the OCM reaction (Figure 12(a)) can be attributed to the different surface density of active sites, which increases with either surface Sr or basic sites.

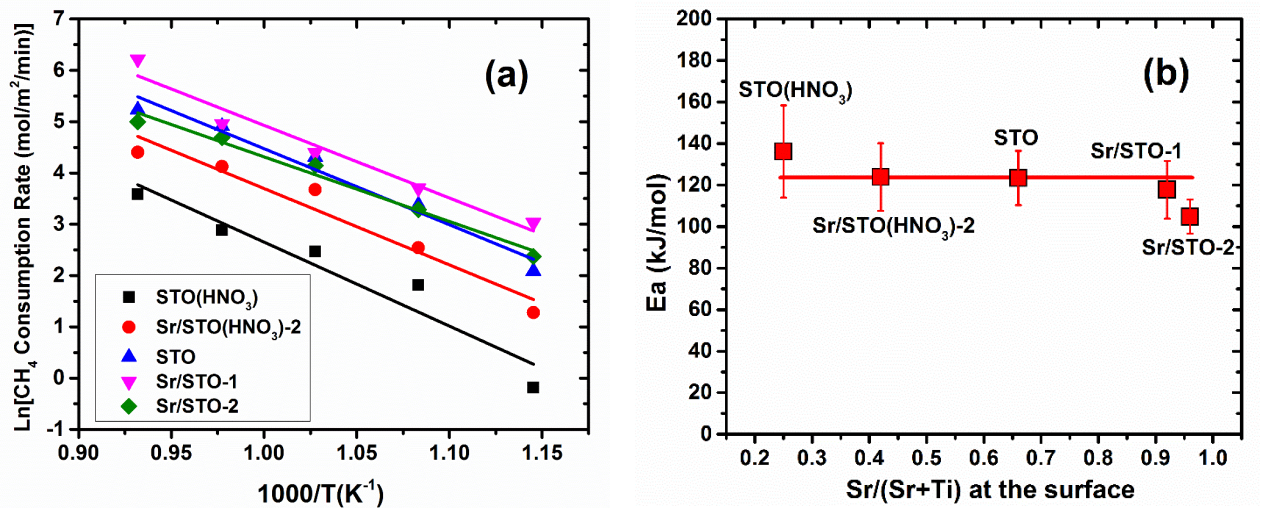

Figure 15. (a) Arrhenius plots for the CH_4 consumption rate. (b) Apparent activation energies (Ea) measured under differential conditions, for CH_4 consumption rate over STO catalysts under study with different surface Sr concentration. Experimental conditions: 5 mg catalyst, 1.0 atm, feed consists of 25 mL/min of 10% CH_4/Ar, 10 mL/min of 5% O_2/He, and 15 mL/min of He as balance gas.

Table 6. Apparent Activation Energies for CH_4 consumption and CO,CO_2, C_2 formation

Sample	Apparent Activation Energy (kJ/mol)			
	CH_4 consumption	CO formation	CO_2 formation	C_2 formation
$STO(HNO_3)$	136.2±22.2	126.4±7.9	124.3±11.4	183.7±25.8
$Sr/STO(HNO_3)$-2	123.9±16.3	118.7±3.4	150.3±6.9	197.4±26.4
STO	123.4±13.0	100.1±15.3	92.2±22.2	189.1±3.3
Sr/STO-1	117.8±13.9	106.4±4.7	110.2±9.8	299.4±29.6
Sr/STO-2	104.8±8.2	91.8±20.0	95.1±20.4	198.7±16.5

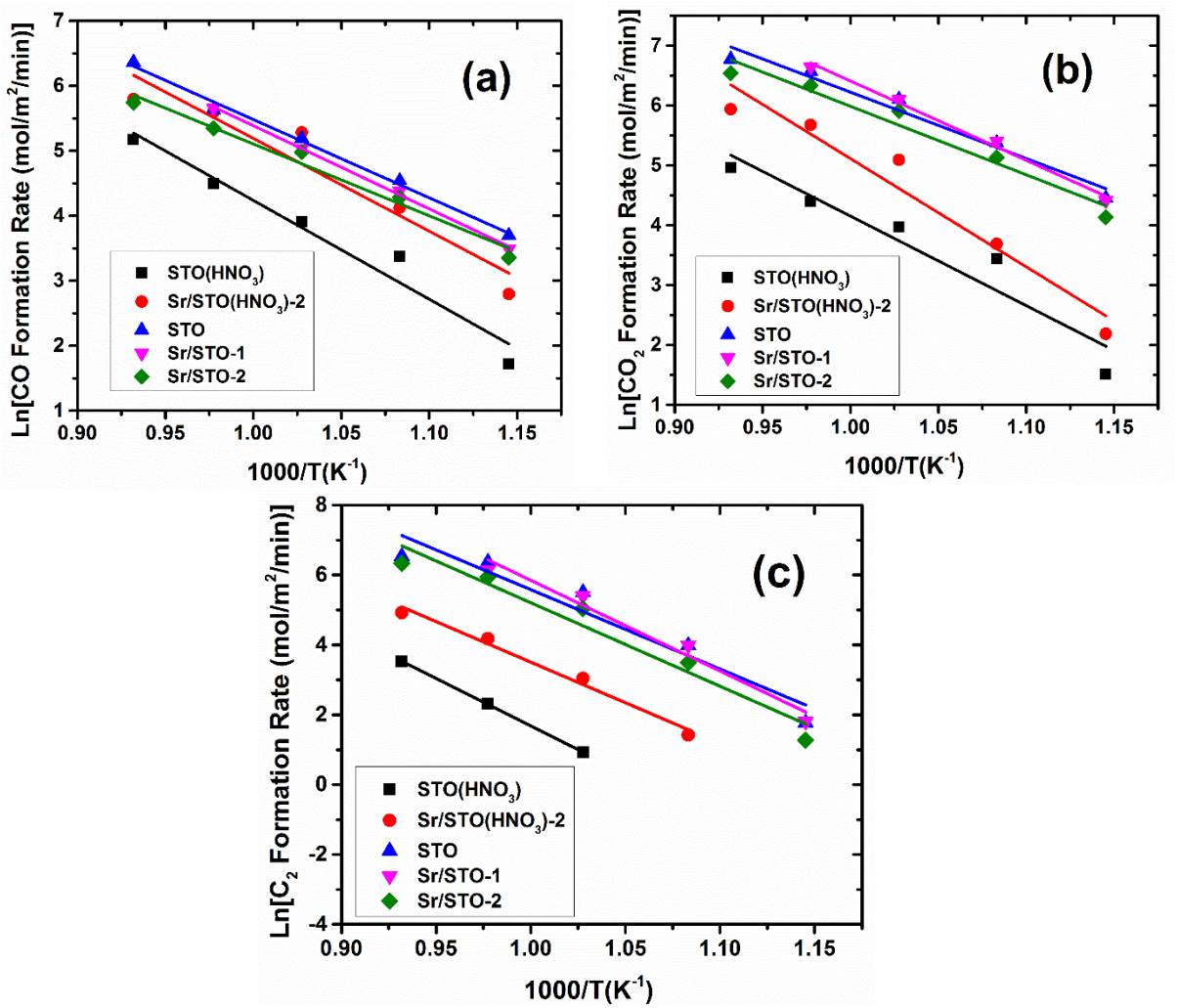

Figure 16. The Arrhenius plots for CO, CO_2 and C_2 formation during OCM over various STO catalysts.

Note: Experimental conditions: 5 mg catalyst, 1.0 atm, feed consists of 25 mL/min of 10% CH_4/Ar, 10 mL/min of 5% O_2/He, and 15 mL/min of He as balance gas.

The acid-base properties of active sites on catalysts are reported to be responsible for the catalytic performance in the OCM reaction[41, 42]. Therefore, the relationship between CH_4 conversion and acid or base site density is investigated and plotted in Figure 17. The CH_4 conversion increases with increasing surface base site density (Figure 17(a)), while it decreases with increasing acid site density (Figure 17(b)).

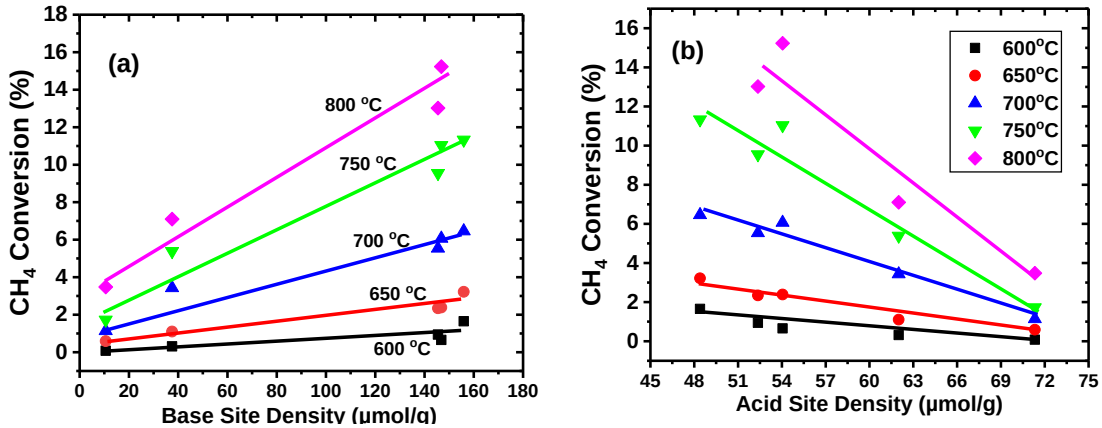

Figure 17. CH_4 conversion as the function of the surface base site density and the acid site density for OCM reaction over various STO samples.

Moreover, Figure 18 indicates that the higher the relative concentration of base sites (i.e. base/(base+acid)), the higher the CH_4 conversion. As mentioned before, CH_4 conversions of STO samples remain steady when Sr/(Sr+Ti) is greater than 0.66. However, after Sr/(Sr+Ti) > 0.66, the relative concentration of basic sites (base/(base+acid)) also remains constant. Furthermore, Figure 8(b) shows that the strength of the basic sites is the same for STO samples with Sr/(Sr+Ti) ratio more than 0.66. Therefore, the CH_4 conversion shows a linear increase with the ratio of base/(base+acid) over the whole range of surface compositions, suggesting that the relative base site concentration (i.e. base/(base+acid)) is a better descriptor for the catalytic activity. This relationship also suggested that the synergy between the basic sites and the acid sites over STO catalysts plays an important role in the oxidative coupling of methane.

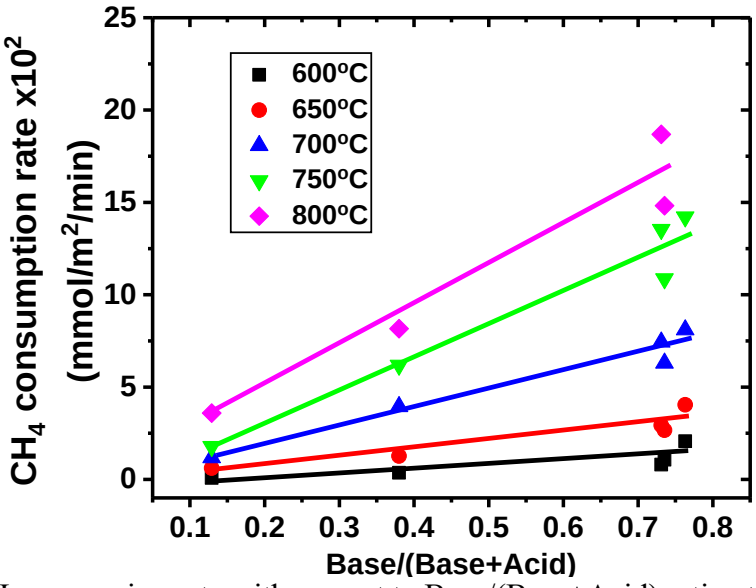

Figure 18. CH_4 conversion rate with respect to Base/(Base+Acid) ratio at different temperatures over various STO samples.

In Figure 18, the enhancement effect of base sites on the CH_4 conversion can be represented by the slopes of the trendlines at each temperature. The enhancement effect of base sites on the CH_4 conversion increases with reaction temperature, since the slope values rise with temperatures (See Table 7). It is also observed from Figure 19, for each sample with a fixed Base/(Base+Acid) concentration, the CH_4 consumption rate is exponentially enhanced with reaction temperature.

Table 7. Slopes of trendlines for Base/(Base+Acid)-CH_4 consumption relationship.

Temperatures	600	650	700	750	800
Slopes of Trendline	2.2	4.5	9.9	18.2	22.1

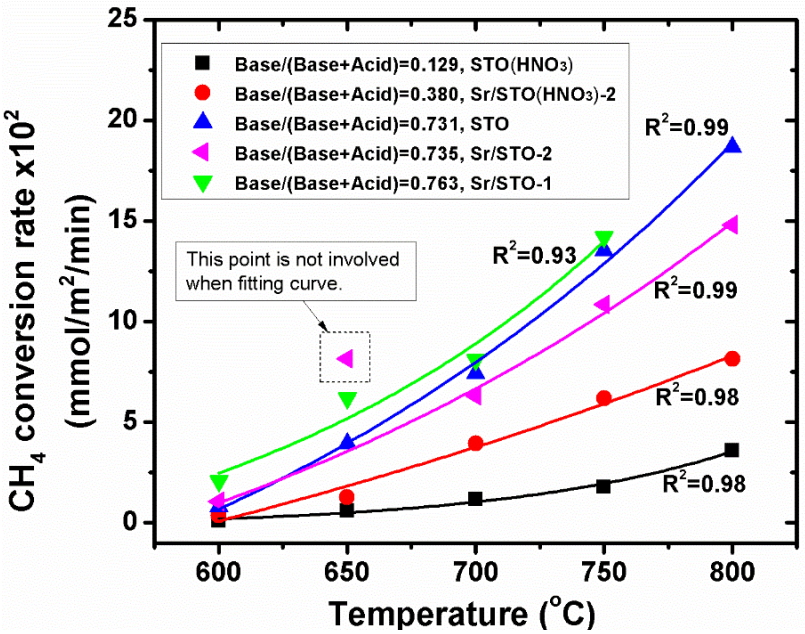

Figure 19. CH_4 conversion rate with respect to temperatures over various STO samples (with different Base/(Base+Acid) ratios).

3.3.6 Kinetics Analysis of STO Samples in OCM

The kinetics of the OCM reaction has been intensively studied over different catalysts[62-64]. In this work, four reported mechanisms, including the Power Law model[61, 65], the Mars-Van Krevelen model[66], the double-site Langmuir-Hinshelwood model[67] and the Eley-Rideal model[68], were examined for the OCM reactions over the STO catalysts. All the reaction schemes proposed by each model and the corresponding rate equations for each mechanism are presented in the Section 3.3.7. To achieve the differential conditions, the OCM reaction was performed at 650°C to obtain low CH_4 conversion (< 10%). It is noted that the O_2-lean condition for kinetic tests (CH_4/O_2 ratio in the range of 2-7) is in favor of both OCM and the partial oxidation reaction[69, 70]. In some kinetic tests for OCM, production of CO and H_2 was detected, suggesting the coexistence of partial oxidation over a metastable state of the catalyst surface. The catalyst pretreatment in O_2 was extended in some cases out to 15 h to achieve the thermodynamically stable

surface that favors the OCM reaction. All results presented in this work are for cases where OCM dominates.

Figure 20 shows the methane consumption rate as a function of $P(CH_4)$ and $P(O_2)$ over different STO catalysts. In general, the rate of CH_4 conversion exhibits a positive dependence on both $P(CH_4)$ and $P(O_2)$. Through a comparison across these STO catalysts, it can be observed that the commercial STO sample has the highest methane conversion rate (except that Sr/STO-1 shows higher conversion rate when $P(CH_4) > 0.048$ atm), while the acid-treated STO(HNO_3) sample shows the lowest methane conversion rate at the same $P(CH_4)$ or $P(O_2)$. We have attempted kinetic analyses of the OCM reaction by using the above-mentioned four models over this set of STO samples (Section 3.3.7). However, poor fitting of the measured methane consumption rates with any of the models suggests that the catalytic behavior of the STO samples cannot be simply described by these proposed four models. Accurate modelling of kinetics for OCM over the reconstructed perovskite catalysts remains contingent upon a detailed computational study of reaction elementary steps.

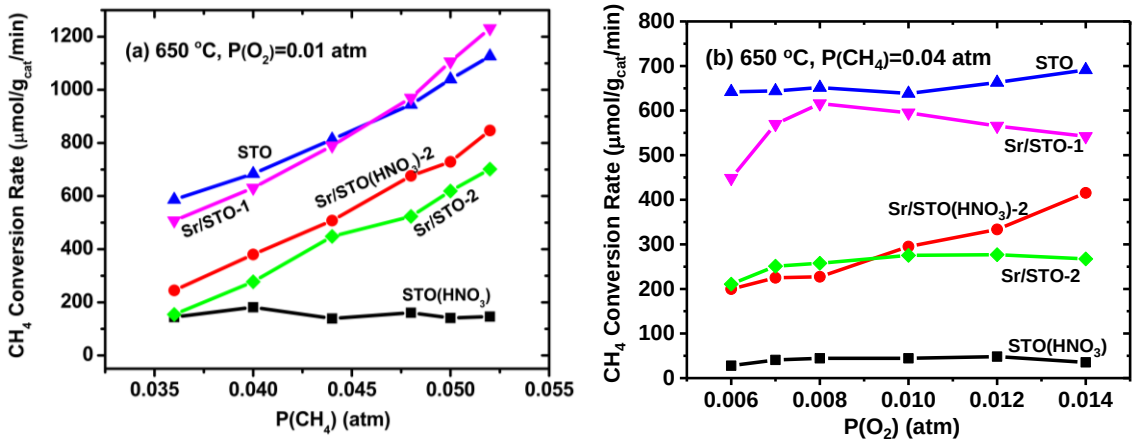

Figure 20. Methane consumption rate as a function of (a) CH_4 pressure at $P(O_2)$=0.01 atm and of (b) O_2 pressure at $P(CH_4)$=0.04 atm, respectively, over various STO samples. (Reaction conditions: 650 °C for bed temperature, total flow rate=50 mL/min, He+Ar as balance gas.)

3.3.7 Methane and Oxygen Consumption Rates over STO Catalysts Based on Different Mechanisms

In present work, the methane consumption rates (r_{CH_4}) were measured under various partial pressure of methane (P_{CH_4}) or oxygen (P_{O_2}) to study the kinetics of OCM reactions. Four kinetic models are tested to analyze the OCM reaction over the STO catalysts with surface reconstruction. The applied models are Power Law model[61, 65], Mars-Van Krevelen model[71], Double site Langmuir-Hinshelwood model[67] and Eley-Rideal model[68].

3.3.7.1 Power Law Model

This model is proposed by Takanabe and Iglesia[65], with the assumption that the methane activation is the rate determine step and dissociative oxygen adsorption is weak at high temperature for OCM reaction. In this mechanism, the first step involves oxygen (O_2) dissociatively adsorbed on the active surface vacancies (*) to form O*. In the second step, methane is activated by surface O* to form methyl radicals and OH*. Finally, two OH* combine to from H_2O and surface vacancies (*). The later steps for C_2H_6 and CO_x formation and corresponding methane consumption rate expression are presented in the Table 8.

Table 8. The OCM reaction scheme proposed by Takanabe and Iglesia[65].

$O_2 + 2(*) \overset{K_1}{\leftrightarrow} 2O^*$	(S1-1)
$CH_4 + O^* \overset{k_2}{\rightarrow} CH_3 \bullet + OH^*$	(S1-2)
$2OH^* \overset{K_3}{\leftrightarrow} H_2O + O^* + (*)$	(S1-3)
$2CH_3 \bullet + M \overset{k_4}{\rightarrow} C_2H_6 + M$	(S1-4)
$CH_3 \bullet + O_2 \overset{k_5}{\rightarrow} CO$	(S1-5)
$2CH_3 \bullet + O^* \overset{k_6}{\rightarrow} C_2H_6 + M$	(S1-6)
CH_4 consumption rate expression: $r_{CH_4} = k_p P_{CH_4} \sqrt{P_{O_2}}$	(Eq S1-1)

M: third body in the reaction.

Based on the above-mentioned mechanism, a power law expression for methane conversion is proposed and tested:

$$r_{CH_4} = k(P_{CH_4})^a (P_{O_2})^b \qquad \text{(Eq S1-2)}$$

The effect of partial pressure of CH_4 and O_2 on methane conversion rate are studied to calculate the reactant orders. Figure 21(a) presents the CH_4 conversion rate as a function of CH_4 partial pressure at a constant oxygen pressure, meanwhile 21(b) shows the CH_4 conversion rate as a function of O_2 partial pressure at fixed methane pressure on all investigated STO samples. Reactant order *a* and one rate constant *k* can be calculated from fitting the curves in Figure 21(a). Similarly, reactant order *b* and one rate constant *k'* can be calculated from fitting the curves in Figure 21(b). If the present STO samples follow this OCM mechanism, the reactants orders should be a=1, b=0.5, respectively. *k* should be equal to *k'*. However, from the fitting results listed in

Table 9, it found that *a* and *b* are not equal to 1 and 0.5, respectively. Moreover, most calculated *k* and *k'* are different. Therefore, the proposed power law rate expression is not satisfactory to describe the OCM reaction of present STO samples.

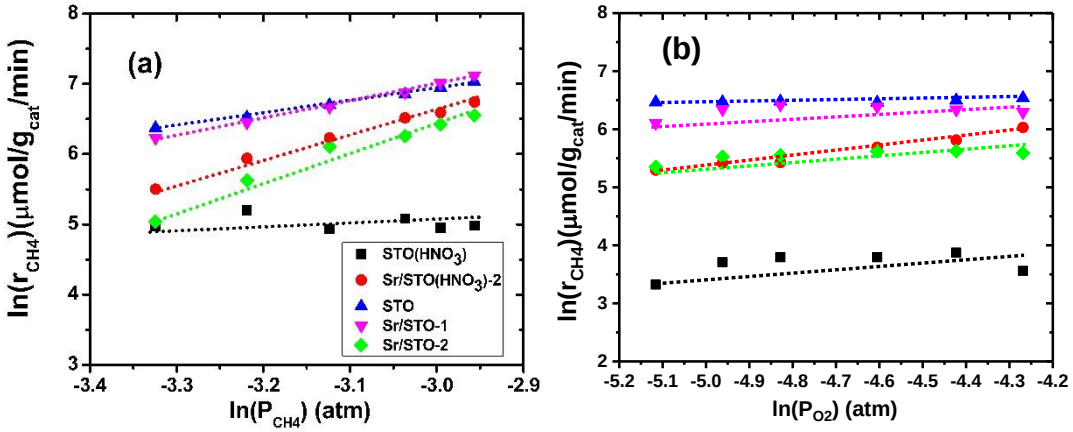

Figure 21. Effect of (a) CH_4 partial pressure on CH_4 conversion rate at $P(O_2)$=0.01 atm and (b) O_2 partial pressure on CH_4 conversion rate at $P(CH_4)$=0.04 atm at 650°C.

Table 9. Results of reactant orders and rate constants for STO samples analyzed by power law model.

Catalyst ID	*a*	*b*	*k*	*k'* ($\mu mol/g_{cat}/min/atm^{1.5}$)
$STO(HNO_3)$	-0.178	0.263	2.92E+02	7.67E+01
$Sr/STO(HNO_3)$-2	3.287	0.846	7.02E+08	5.74E+08
STO	1.779	0.071	2.95E+05	2.80E+05
Sr/STO-1	2.408	0.133	2.73E+06	2.39E+06
Sr/STO-2	3.984	0.250	3.07E+08	3.07E+08

3.3.7.2 Mars-Van Krevelen Model

The scheme in the Table 10 shows the elementary reaction steps in the proposed Mars-Van Krevelen mechanism[71]. First of all, the surface active site is oxidized to form the O·S. In the second step, the gaseous methane reacts with oxidized active site, which consequently reduced the

active site to its original form. The methyl radical is also formed in this step. Then the methyl radicals partially react with oxygen to generate CO_x (step S2-3), partially undergo coupling to form C_2H_6 (step S2-4). The corresponding methane consumption rate is also presented in the Table 10.

Table 10. The Mars-Van Krevelen mechanism for OCM reaction[71].

$$\frac{1}{2}O_2 + S \xrightarrow{k_1} O \cdot S \quad \text{(S2-1)}$$

$$CH_4 + O \cdot S \xrightarrow{k_2} CH_3 \bullet + OH \bullet + S \quad \text{(S2-2)}$$

$$CH_3 \bullet + \frac{x}{2}O_2 \xrightarrow{k_3} CO_x \quad \text{(S2-3)}$$

$$2CH_3 \bullet \xrightarrow{k_4} C_2H_6 \quad \text{(S2-4)}$$

CH_4 consumption rate expression: $r_{CH_4} = \frac{k_1 k_2 P_{O_2}^{0.5} P_{CH_4}}{k_1 P_{O_2}^{0.5} + k_2 P_{CH_4}}$ (Eq S2-1)

S: surface active site in reduced form; O·S: surface active site in oxidized form.

The equation (EqS2-1) can be rearranged to the following two expressions:

$$\frac{P_{O_2}^{0.5}}{r_{CH_4}} = \frac{1}{k_1} + \frac{P_{O_2}^{0.5}}{k_2 P_{CH_4}} \quad \text{(Eq S2-2)}$$

$$\frac{P_{CH_4}}{r_{CH_4}} = \frac{1}{k_2} + \frac{P_{CH_4}}{k_1 P_{O_2}^{0.5}} \quad \text{(Eq S2-3)}$$

When the P_{O_2} is constant, plots of $\frac{P_{O_2}^{0.5}}{r_{CH_4}}$ against $\frac{1}{P_{CH_4}}$ can be obtained. Similarly, when the P_{CH_4} is fixed, plots of $\frac{P_{CH_4}}{r_{CH_4}}$ against $\frac{1}{P_{O_2}^{0.5}}$ can also be drawn. These two plots are shown in Figure 22. Two sets of kinetic parameters k_1, k_2 and k_1', k_2' can be determined from the relationships of

$\frac{P_{O_2}^{0.5}}{r_{CH_4}} \sim \frac{1}{P_{CH_4}}$ and $\frac{P_{CH_4}}{r_{CH_4}} \sim \frac{1}{P_{O_2}^{0.5}}$, respectively. Ideally, if the OCM reaction of STO samples follows the Mars-Van Krevelen model, identical k_1 and k_1' (k_2 and k_2') are supposed to be attained. The kinetic parameters, determined from the linear plots, are given in Table 11. Obviously, k_1 and k_1' (k_2 and k_2') are significantly different. This model does not fit the kinetics for the OCM reactions over all the STO catalysts.

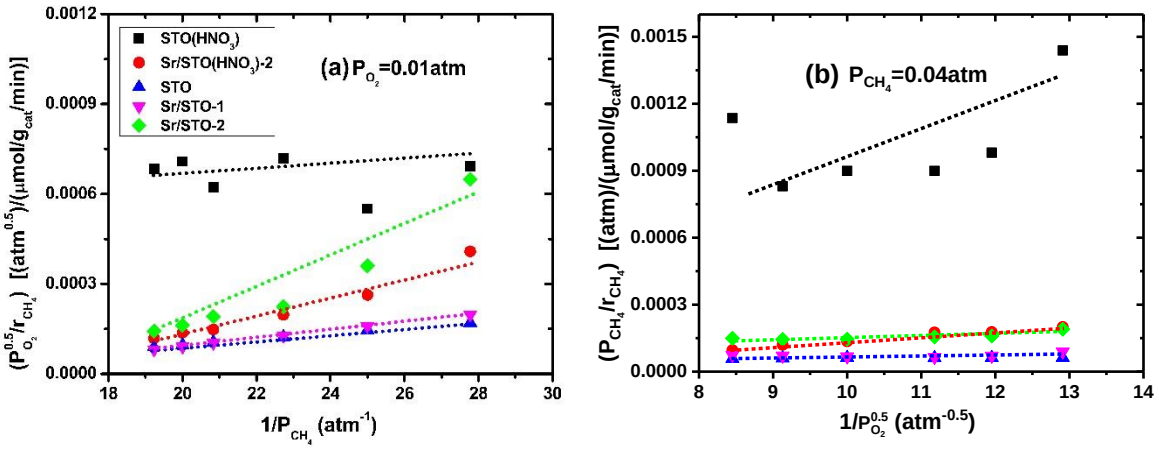

Figure 22. (a) Plots of $\frac{P_{O_2}^{0.5}}{r_{CH_4}}$ against $\frac{1}{P_{CH_4}}$ at P(O_2)=0.01 atm and (b)plots of $\frac{P_{CH_4}}{r_{CH_4}}$ against $\frac{1}{P_{O_2}^{0.5}}$ at P(CH_4)=0.04 atm at 650°C.

Table 11. Kinetic parameters for STO samples analyzed by Mars-Van Krevelen model.

Catalyst ID (Unit)	k_1 ($\mu mol/g_{cat}/min/atm^{0.5}$)	k_1'	k_2 ($\mu mol/g/min/atm$)	k_2'
$STO(HNO_3)$	1.32E+03	6.18E+02	-2.32E+04	2.90E+03
$Sr/STO(HNO_3)$-2	-1.90E+03	1.74E+03	3.06E+03	-1.07E+04
STO	-1.05E+04	5.13E+04	1.04E+04	1.89E+04
Sr/STO-1	-5.55E+03	1.72E+04	7.38E+03	2.08E+04
Sr/STO-2	-1.02E+03	4.91E+03	1.78E+03	1.41E+04

3.3.7.3 Double Site Langmuir-Hinshelwood Model

Table 12 shows the proposed reaction steps for OCM reactions following the Double site Langmuir-Hinshelwood mechanism. In this mechanism, oxygen and methane are adsorbed on two types of active sites (S^1 and S^2) to form the $O_2{\cdot}S^1$ and $CH_4{\cdot}S^2$ species in steps S3-1 and S3-2, respectively. In next step (S3-3), the C-H bond is activated and methyl radicals are produced by the reaction between molecularly adsorbed methane and oxygen species. Then the methyl radicals partially react with either oxygen on the catalyst surface or gaseous oxygen to generate CO_x (S3-4). Simultaneously, methyl radicals undergo coupling to form C_2H_6 (S3-5). The corresponding methane consumption rate Eq S3-1 is presented in the Table 12.

When the P_{O_2} is fixed in the OCM reaction, Eq S3-1 can be rearranged to,

$$\frac{P_{CH_4}}{r_{CH_4}} = \left(\frac{1+K_{O_2}P_{O_2}}{kK_{O_2}P_{O_2}}\right)P_{CH_4} + \frac{1+K_{O_2}P_{O_2}}{kK_{O_2}K_{CH_4}P_{O_2}} \qquad \text{(Eq S3-2)}$$

The plot of $\frac{P_{CH_4}}{r_{CH_4}}$ as a function of P_{CH_4} indicates that the slope of the plot is $\frac{1+K_{O_2}P_{O_2}}{kK_{O_2}P_{O_2}}$ and the intercept is $\frac{1+K_{O_2}P_{O_2}}{kK_{O_2}K_{CH_4}P_{O_2}}$. The adsorption equilibrium constant for CH_4 (K_{CH_4}) can be obtained from the ratio of slope to intercept in Eq S3-2.

Similarly, when the P_{CH_4} is constant, Eq S3-1 can be rearranged to,

$$\frac{P_{O_2}}{r_{CH_4}} = \left(\frac{1+K_{CH_4}P_{CH_4}}{kK_{CH_4}P_{CH_4}}\right)P_{O_2} + \frac{1+K_{CH_4}P_{CH_4}}{kK_{O_2}K_{CH_4}P_{CH_4}} \qquad \text{(Eq S3-3)}$$

The plot of $\frac{P_{O_2}}{r_{CH_4}}$ as a function of P_{O_2} indicates that the slope of the plot is $\frac{1+K_{CH_4}P_{CH_4}}{kK_{CH_4}P_{CH_4}}$ and the intercept is $\frac{1+K_{CH_4}P_{CH_4}}{kK_{O_2}K_{CH_4}P_{CH_4}}$. The adsorption equilibrium constant for O_2 (K_{O2}) can be obtained from the ratio of slope to intercept in Eq S3-3.

Plots of P_{CH4}/r_{CH4} against P_{CH4} and plots of P_{O2}/r_{CH4} against P_{O2} are shown in Figure 23. Two methane activation rate constants (*k* and *k'*) can be calculated by substituting the K_{CH4} and K_{O2} into the Eq S3-2 and Eq S3-3, respectively. If the Double site Langmuir-Hinshelwood model fits the kinetics for the OCM reaction over STO samples, *k* and *k'* with the same values will be solved. The determined kinetic parameters are listed in the Table 13. It is found from Figure 23 that the linear fitting for Sr/STO(HNO_3)-2, STO, Sr/STO-1, Sr/STO-2 samples exhibit negative intercepts. Also, all K_{CH4} are with negative values, and *k* does not match with *k'* value for each STO sample. These results are in contrary to the proposed model. Therefore, the Double site Langmuir-Hinshelwood model is not suitable to describe the OCM reaction over STO samples.

Table 12. The Double site Langmuir-Hinshelwood mechanism for OCM reaction[67].

$O_2 + S^1 \overset{K_{O2}}{\leftrightarrow} O_2 \cdot S^1$	(S3-1)
$CH_4 + S^2 \overset{K_{CH4}}{\leftrightarrow} CH_4 \cdot S^2$	(S3-2)
$CH_4 \cdot S^2 + O_2 \cdot S^1 \overset{k}{\rightarrow} CH_3 \bullet + HO_2 \bullet + S^1 + S^2$	(S3-3)
$CH_3 \bullet + \frac{x}{2} O_2 \overset{k_1}{\rightarrow} CO_x$	(S3-4)
$2CH_3 \bullet \overset{k_2}{\rightarrow} C_2H_6$	(S3-5)
CH_4 consumption rate expression: $r_{CH_4} = \frac{kK_{O_2}K_{CH_4}P_{CH_4}P_{O_2}}{(1+K_{O_2}P_{O_2})(1+K_{CH_4}P_{CH_4})}$	(Eq3-1)

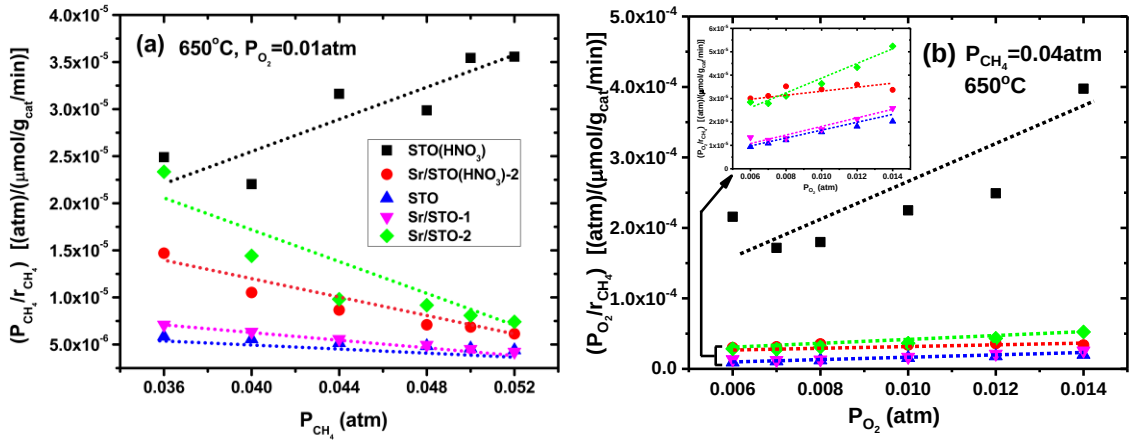

Figure 23. Linearized correlations of (a) $\frac{P_{CH_4}}{r_{CH_4}}$ versus P_{CH_4} and (b) $\frac{P_{O_2}}{r_{CH_4}}$ versus P_{O_2}. The inset in (b) shows an enlarged image of Sr/STO(HNO_3)-2, STO, Sr/STO-1, Sr/STO-2 samples.

Table 13. Kinetic parameters for STO samples analyzed by Double site Langmuir-Hinshelwood model.

Catalyst ID (Unit)	K_{CH_4} (atm^{-1})	K_{O_2} (atm^{-1})	k ($\mu mol/g_{cat}/min$)	k' ($\mu mol/g_{cat}/min$)
STO(HNO_3)	-1.41E+02	8.71E+02	1.41E+02	3.65E+01
Sr/STO(HNO_3)-2	-1.59E+01	1.67E+01	-1.40E+03	-1.20E+03
STO	-9.98E+00	1.10E+03	-1.19E+03	-1.09E+03
Sr/STO-1	-1.33E+01	1.76E+03	-5.89E+02	-5.21E+02
Sr/STO-2	-1.72E+01	4.20E+02	-1.37E+02	-1.49E+02

3.3.7.4 Eley-Rideal Model

The elementary steps in the Eley-Rideal mechanism are listed in Table 14. The oxygen is firstly adsorbed on the surface active site S and form the active species $(O_2)_{ads}$ (S4-1). The gaseous methane reacts with $(O_2)_{ads}$ to form the methyl radicals in step (S4-2). Similar with other mechanism, some generated methyl radicals are oxidized to CO_x product (S4-3), and some undergo the coupling to form the ethane at the same time(S4-4). The rate law for CH_4 consumption is listed in Table 14 as well.

Table 14. The Eley-Rideal mechanism for OCM reaction[68].

$O_2 + S \overset{K_{ads}}{\leftrightarrow} (O_2)_{ads}$	(S4-1)
$CH_4 + (O_2)_{ads} \overset{k}{\rightarrow} CH_3\bullet + HO_2\bullet + S$	(S4-2)
$CH_3\bullet + \frac{x}{2}O_2 \overset{k_1}{\rightarrow} CO_x$	(S4-3)
$2CH_3\bullet \overset{k_2}{\rightarrow} C_2H_6$	(S4-4)
CH_4 consumption rate expression: $r_{CH_4} = \frac{kP_{CH_4}K_{ads}P_{O_2}}{(1+K_{ads}P_{O_2})}$	(Eq S4-1)

When the partial pressure of CH_4 is fixed, the rate expression (Eq S4-1) can be rearranged to,

$$\frac{P_{CH_4}}{r_{CH_4}} = \left(\frac{1}{kK_{ads}}\right)\frac{1}{P_{O_2}} + \frac{1}{k} \qquad \text{(Eq S4-2)}$$

The methane activation rate constant k and adsorption equilibrium constant for oxygen (K_{ads}) can be determined from the intercept $\frac{1}{k}$ and slope $\frac{1}{kK_{ads}}$.

When the partial pressure of O_2 is fixed, the rate expression (Eq S4-1) can be written as,

$$\frac{P_{O_2}}{r_{CH_4}} = \left(\frac{1+K_{ads}P_{O_2}}{kK_{ads}}\right)\frac{1}{P_{CH_4}} \qquad \text{(Eq S4-3)}$$

The linear correlation of $\frac{P_{O_2}}{r_{CH_4}}$ versus $\frac{1}{P_{CH_4}}$ in (Eq S4-3), whose slope is $\frac{1+K_{ads}P_{O_2}}{kK_{ads}}$ and the intercept is 0, can be used for validating the proposed model. The plots of $\frac{P_{CH_4}}{r_{CH_4}} \sim \frac{1}{P_{O_2}}$ and $\frac{P_{O_2}}{r_{CH_4}} \sim \frac{1}{P_{CH_4}}$ are drawn in Figure 24.

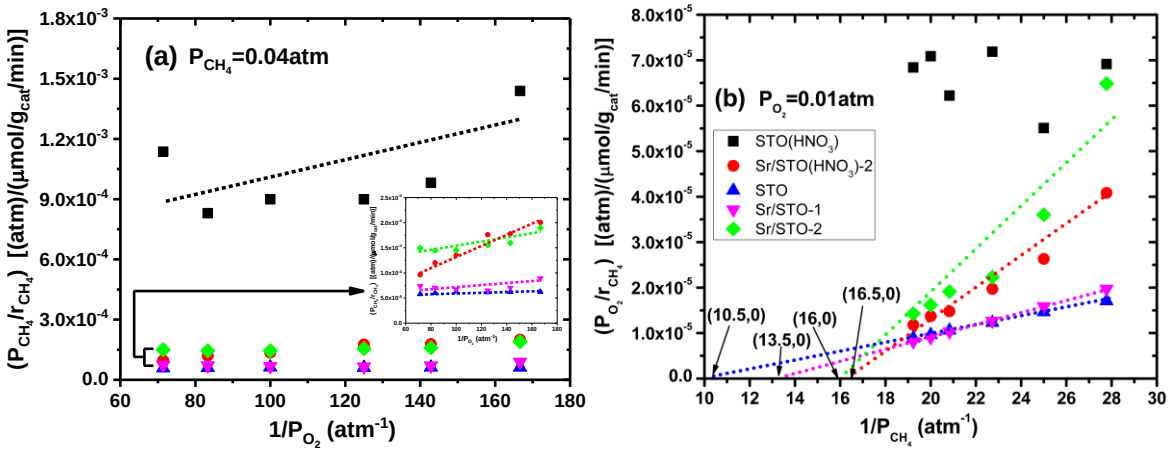

Figure 24. Linearized correlations of (a) $\frac{P_{CH_4}}{r_{CH_4}}$ versus $\frac{1}{P_{O_2}}$, and (b) $\frac{P_{O_2}}{r_{CH_4}}$ versus $\frac{1}{P_{CH_4}}$. The inset in (a) shows an enlarged image of Sr/STO(HNO_3)-2, STO, Sr/STO-1, Sr/STO-2 samples.

Table 15. Kinetic parameters for STO samples analyzed by Eley-Rideal model.

Catalyst ID (Unit)	*k* (μmol/g_{cat}/min/atm)	K_{ads} (atm^{-1})	*Slope-1*	*Slope-2*
STO(HNO_3)	1.54E+03	1.96E+02	9.82E-06	-4.30E-07
Sr/STO(HNO_3)-2	3.58E+04	2.61E+01	1.35E-06	3.27E-06
STO	1.75E+04	1.43E+03	6.11E-07	9.60E-07
Sr/STO-1	1.70E+04	4.91E+02	7.09E-07	1.36E-06
Sr/STO-2	8.94E+03	2.80E+02	1.52E-06	5.61E-06

Note: Slope-1: slope of Eq4-3, calculated based on the k and K_{ads} values from Eq4-2 and Figure S14(a). Slope-2: slope of Eq4-3, obtained from data fitting from Figure S14(b).

The determined kinetic parameters *k* and K_{ads} are presented in the Table 15. However, the curves of $\frac{P_{O_2}}{r_{CH_4}} \sim \frac{1}{P_{CH_4}}$ plotted in Figure 24(b) show that x-intercepts for Sr/STO(HNO_3)-2, STO, Sr/STO-1, Sr/STO-2 lines are (16.5,0), (10.5,0), (13.5,0), (16,0), respectively. Also, the cross-check of Eq S4-3 slope in Table 15 indicates the different values of slope-1 and slope-2. Thus, these results are in contrary to the proposed model. Eley-Rideal model cannot be used for fitting the OCM reaction over STO catalysts.

3.4 Conclusions

In this work, surface reconstructed $SrTiO_3$ samples, with different surface composition of Sr, were obtained through incipient wetness impregnation and chemical etching with HNO_3. UV-Raman and low energy ion scattering (LEIS) analysis results are in good agreement on the surface and subsurface composition of reconstructed STO samples. The redox capability of STO samples was found to be the same, thus their different catalytic performance can be related to the surface acid-base properties rather than lattice reducibility. The OCM reaction at steady state was performed at 600-800 ^oC and it was found that the Sr enrichment (resulting from surface-

reconstruction) enhances the CH_4 conversion, C_2 selectivity as well as the ratio of C_2H_4/C_2H_6 up to certain surface Sr concentration, similar to the promoting effect of the surface Sr concentration on methane combustion. Furthermore, it is shown that the catalytic activity (CH_4 conversion) increases linearly with the relative concentration of basic sites (base/(base+acid)) over the STO catalysts at the full range of surface Sr concentrations, rendering the relative concentration of basic sites as a tentative descriptor for the activity of STO samples in the OCM reaction. These results for the model STO samples with controlled surface compositions and with the same bulk structure provide valuable insights into designing more efficient perovskite-based catalysts for methane activation and conversion via surface reconstructions.

Reference

[1] F. Polo Garzon, V. Fung, X. Liu, Z.D. Hood, E.E. Bickel, L. Bai, H. Tian, G.S. Foo, M. Chi, D.-e. Jiang, Z. Wu, Understanding the Impact of Surface Reconstruction of Perovskite Catalysts on CH4 Activation and Combustion, ACS Catalysis, 8 (2018) 10306-10315.

[2] C. Mesters, A Selection of Recent Advances in C1 Chemistry, Annu Rev Chem Biomol Eng, 7 (2016) 223-238.

[3] U. Zavyalova, M. Holena, R. Schlögl, M. Baerns, Statistical Analysis of Past Catalytic Data on Oxidative Methane Coupling for New Insights into the Composition of High-Performance Catalysts, ChemCatChem, 3 (2011) 1935-1947.

[4] P. Schwach, X. Pan, X. Bao, Direct Conversion of Methane to Value-Added Chemicals over Heterogeneous Catalysts: Challenges and Prospects, Chem Rev, 117 (2017) 8497-8520.

[5] D.J. Driscoll, W. Martir, J.X. Wang, J.H. Lunsford, Formation of gas-phase methyl radicals over magnesium oxide, Journal of the American Chemical Society, 107 (1985) 58-63.

[6] S.C. Reyes, C. Kelkar, E. Iglesia, Kinetic-transport models and the design of catalysts and reactors for the oxidative coupling of methane, Catalysis letters, 19 (1993) 167-180.

[7] J. Song, Y. Sun, R. Ba, S. Huang, Y. Zhao, J. Zhang, Y. Sun, Y. Zhu, Monodisperse Sr–La_2O_3 hybrid nanofibers for oxidative coupling of methane to synthesize C_2 hydrocarbons, Nanoscale, 7 (2015) 2260-2264.

[8] P. Huang, Y. Zhao, J. Zhang, Y. Zhu, Y. Sun, Exploiting shape effects of La_2O_3 nanocatalysts for oxidative coupling of methane reaction, Nanoscale, 5 (2013) 10844-10848.

[9] T. Levan, M. Che, J.M. Tatibouet, M. Kermarec, Infrared Study of the Formation and Stability of $La_2O_2CO_3$ During the Oxidative Coupling of Methane on La_2O_3, Journal of Catalysis, 142 (1993) 18-26.

[10] J.H. Lunsford, The Catalytic Oxidative Coupling of Methane, Angewandte Chemie International Edition in English, 34 (1995) 970-980.

[11] D. Dissanayake, K.C.C. Kharas, J.H. Lunsford, M.P. Rosynek, Catalytic Partial Oxidation of Methane over Ba-Pb, Ba-Bi, and Ba-Sn Perovskites, Journal of Catalysis, 139 (1993) 652-663.

[12] F. Polo-Garzon, Z. Wu, Acid–base catalysis over perovskites: a review, Journal of Materials Chemistry A, (2018).

[13] W. Ding, Y. Chen, X. Fu, Oxidative coupling of methane over Ce^{4+}-doped Ba_3WO_6 catalysts: investigation on oxygen species responsible for catalytic performance, Catalysis Letters, 23 (1994) 69-78.

[14] W. Ding, Y. Chen, X. Fu, Influence of surface composition of perovskite-type complex oxides on methane oxidative coupling, Applied Catalysis A: General, 104 (1993) 61-75.

[15] G.E. Keller, M.M. Bhasin, Synthesis of ethylene via oxidative coupling of methane:I. Determination of active catalysts, Journal of Catalysis, 73 (1982) 9-19.

[16] R.V. Siriwardane*, A. Shamsi, Oxidative coupling of methane over calcium manganate and gadolinium manganate perovskites promoted with sodium pyrophosphate, Applied Catalysis, 60 (1990) 119-136.

[17] R. Ghose, H.T. Hwang, A. Varma, Oxidative coupling of methane using catalysts synthesized by solution combustion method, Applied Catalysis A: General, 452 (2013) 147-154.

[18] K.-I. Aika, K. Aono, Oxidative coupling of methane over $SrCO_3$ and SrO, Journal of the Chemical Society, Faraday Transactions, 87 (1991).

[19] S. Arndt, G. Laugel, S. Levchenko, R. Horn, M. Baerns, M. Scheffler, R. Schlögl, R. Schomäcker, A Critical Assessment of Li/MgO-Based Catalysts for the Oxidative Coupling of Methane, Catalysis Reviews, 53 (2011) 424-514.

[20] L. Luo, Y. Jin, H. Pan, X. Zheng, L. Wu, R. You, W. Huang, Distribution and role of Li in Li-doped MgO catalysts for oxidative coupling of methane, Journal of Catalysis, 346 (2017) 57-61.

[21] U. Zavyalova, M. Geske, R. Horn, G. Weinberg, W. Frandsen, M. Schuster, R. Schlögl, Morphology and Microstructure of Li/MgO Catalysts for the Oxidative Coupling of Methane, ChemCatChem, 3 (2011) 949-959.

[22] N. Maksimov, G. Selyutin, A. Anshits, E. Kondratenko, V. Roguleva, The influence of defect nature on catalytic performance of Li, Na-doped MgO, CaO and SrO in the oxidative coupling of methane, Catalysis today, 42 (1998) 279-281.

[23] S. Arndt, T. Otremba, U. Simon, M. Yildiz, H. Schubert, R. Schomäcker, $Mn–Na_2WO_4/SiO_2$ as catalyst for the oxidative coupling of methane. What is really known?, Applied Catalysis A: General, 425-426 (2012) 53-61.

[24] P. Wang, G. Zhao, Y. Wang, Y. Lu, $MnTiO_3$-driven low-temperature oxidative coupling of methane over TiO_2-doped Mn_2O_3-Na_2WO_4/SiO_2 catalyst, Sci Adv, 3 (2017) e1603180.

[25] D.J. Wang, M.P. Rosynek, J.H. Lunsford, Oxidative Coupling of Methane over Oxide-Supported Sodium-Manganese Catalysts, Journal of Catalysis, 155 (1995) 390-402.

[26] Z. Taheri, N. Seyed-Matin, A.A. Safekordi, K. Nazari, S.Z. Pashne, A comparative kinetic study on the oxidative coupling of methane over LSCF perovskite-type catalyst, Applied Catalysis A: General, 354 (2009) 143-152.

[27] R. Spinicci, P. Marini, S. De Rossi, M. Faticanti, P. Porta, Oxidative coupling of methane on $LaAlO_3$ perovskites partially substituted with alkali or alkali-earth ions, Journal of Molecular Catalysis A: Chemical, 176 (2001) 253-265.

[28] D. Dissanayake, K. Kharas, J.H. Lunsford, M. Rosynek, Catalytic partial oxidation of methane over Ba-Pb, Ba-Bi, and Ba-Sn perovskites, Journal of Catalysis, 139 (1993) 652-663.

[29] H. Liu, Y. Wei, J. Caro, H. Wang, Oxidative Coupling of Methane with High C_2 Yield by using Chlorinated Perovskite $Ba_{0.5}Sr_{0.5}Fe_{0.2}Co_{0.8}O_{3-\delta}$ as Catalyst and N_2O as Oxidant, ChemCatChem, 2 (2010) 1539-1542.

[30] J. Xu, L. Peng, X. Fang, Z. Fu, W. Liu, X. Xu, H. Peng, R. Zheng, X. Wang, Developing reactive catalysts for low temperature oxidative coupling of methane: On the factors deciding the

reaction performance of $Ln_2Ce_2O_7$ with different rare earth A sites, Applied Catalysis A: General, 552 (2018) 117-128.

[31] Y. Ivanova, E. Sutormina, N. Rudina, A. Nartova, L. Isupova, Effect of preparation route on Sr_2TiO_4 catalyst for the oxidative coupling of methane, Catalysis Communications, (2018).

[32] H. Imai, T. Tagawa, N. Kamide, Oxidative coupling of methane over amorphous lanthanum aluminum oxides, Journal of Catalysis, 106 (1987) 394-400.

[33] Z. Fakhroueian, F. Farzaneh, N. Afrookhteh, Oxidative coupling of methane catalyzed by Li, Na and Mg doped $BaSrTiO_3$, Fuel, 87 (2008) 2512-2516.

[34] D.V. Ivanov, L.A. Isupova, E.Y. Gerasimov, L.S. Dovlitova, T.S. Glazneva, I.P. Prosvirin, Oxidative methane coupling over Mg, Al, Ca, Ba, Pb-promoted $SrTiO_3$ and Sr_2TiO_4 : Influence of surface composition and microstructure, Applied Catalysis A: General, 485 (2014) 10-19.

[35] L.C. Seitz, C.F. Dickens, K. Nishio, Y. Hikita, J. Montoya, A. Doyle, C. Kirk, A. Vojvodic, H.Y. Hwang, J.K. Norskov, T.F. Jaramillo, A highly active and stable IrOx/$SrIrO_3$ catalyst for the oxygen evolution reaction, Science, 353 (2016) 1011-1014.

[36] J.M.P. Martirez, S. Kim, E.H. Morales, B.T. Diroll, M. Cargnello, T.R. Gordon, C.B. Murray, D.A. Bonnell, A.M. Rappe, Synergistic Oxygen Evolving Activity of a TiO_2-Rich Reconstructed $SrTiO_3$(001) Surface, Journal of the American Chemical Society, 137 (2015) 2939-2947.

[37] E. Fabbri, M. Nachtegaal, T. Binninger, X. Cheng, B.-J. Kim, J. Durst, F. Bozza, T. Graule, R. Schäublin, L. Wiles, M. Pertoso, N. Danilovic, K.E. Ayers, T.J. Schmidt, Dynamic surface self-reconstruction is the key of highly active perovskite nano-electrocatalysts for water splitting, Nature Materials, 16 (2017) 925.

[38] Y. Peng, W. Si, J. Luo, W. Su, H. Chang, J. Li, J. Hao, J. Crittenden, Surface Tuning of $La_{0.5}Sr_{0.5}CoO_3$ Perovskite Catalysts by Acetic Acid for NO_x Storage and Reduction, Environmental Science & Technology, 50 (2016) 6442-6448.

[39] G.S. Foo, Z.D. Hood, Z. Wu, Shape Effect Undermined by Surface Reconstruction: Ethanol Dehydrogenation over Shape-Controlled $SrTiO_3$ Nanocrystals, ACS Catalysis, 8 (2018) 555-565.

[40] F. Polo-Garzon, S.Z. Yang, V. Fung, G.S. Foo, E.E. Bickel, M.F. Chisholm, D.E. Jiang, Z. Wu, Controlling Reaction Selectivity through the Surface Termination of Perovskite Catalysts, Angew Chem Int Ed Engl, 56 (2017) 9820-9824.

[41] F. Papa, D. Gingasu, L. Patron, A. Miyazaki, I. Balint, On the nature of active sites and catalytic activity for OCM reaction of alkaline-earth oxides-neodymia catalytic systems, Applied Catalysis A: General, 375 (2010) 172-178.

[42] F. Papa, P. Luminita, P. Osiceanu, R. Birjega, M. Akane, I. Balint, Acid–base properties of the active sites responsible for C_2^+ and CO_2 formation over MO–Sm_2O_3 (M=Zn, Mg, Ca and Sr) mixed oxides in OCM reaction, Journal of Molecular Catalysis A: Chemical, 346 (2011) 46-54.

[43] Z. Wu, S. Dai, S.H. Overbury, Multiwavelength Raman Spectroscopic Study of Silica-Supported Vanadium Oxide Catalysts, The Journal of Physical Chemistry C, 114 (2010) 412-422.

[44] D.A. Tenne, A. Bruchhausen, N.D. Lanzillotti-Kimura, A. Fainstein, R.S. Katiyar, A. Cantarero, A. Soukiassian, V. Vaithyanathan, J.H. Haeni, W. Tian, D.G. Schlom, K.J. Choi, D.M. Kim, C.B. Eom, H.P. Sun, X.Q. Pan, Y.L. Li, L.Q. Chen, Q.X. Jia, S.M. Nakhmanson, K.M. Rabe,

X.X. Xi, Probing nanoscale ferroelectricity by ultraviolet Raman spectroscopy, Science, 313 (2006) 1614-1616.

[45] I.E. Wachs, K. Routray, Catalysis Science of Bulk Mixed Oxides, ACS Catalysis, 2 (2012) 1235-1246.

[46] S.P. Phivilay, A.A. Puretzky, K. Domen, I.E. Wachs, Nature of Catalytic Active Sites Present on the Surface of Advanced Bulk Tantalum Mixed Oxide Photocatalysts, ACS Catalysis, 3 (2013) 2920-2929.

[47] M. Li, U. Tumuluri, Z. Wu, S. Dai, Effect of Dopants on the Adsorption of Carbon Dioxide on Ceria Surfaces, ChemSusChem, 8 (2015) 3651-3660.

[48] Y.T. Chua, P.C. Stair, I.E. Wachs, A Comparison of Ultraviolet and Visible Raman Spectra of Supported Metal Oxide Catalysts, The Journal of Physical Chemistry B, 105 (2001) 8600-8606.

[49] H. Tian, I.E. Wachs, L.E. Briand, Comparison of UV and visible Raman spectroscopy of bulk metal molybdate and metal vanadate catalysts, J Phys Chem B, 109 (2005) 23491-23499.

[50] W.G. Nilsen, J.G. Skinner, Raman Spectrum of Strontium Titanate, The Journal of Chemical Physics, 48 (1968) 2240-2248.

[51] D.A. Tenne, A.K. Farrar, C.M. Brooks, T. Heeg, J. Schubert, H.W. Jang, C.W. Bark, C.M. Folkman, C.B. Eom, D.G. Schlom, Ferroelectricity in nonstoichiometric $SrTiO_3$ films studied by ultraviolet Raman spectroscopy, Applied Physics Letters, 97 (2010).

[52] L.F. da Silva, W. Avansi, J. Andres, C. Ribeiro, M.L. Moreira, E. Longo, V.R. Mastelaro, Long-range and short-range structures of cube-like shape $SrTiO_3$ powders: microwave-assisted hydrothermal synthesis and photocatalytic activity, Phys Chem Chem Phys, 15 (2013) 12386-12393.

[53] M.L. Moreira, V.M. Longo, W. Avansi, M.M. Ferrer, J. Andrés, V.R. Mastelaro, J.A. Varela, É. Longo, Quantum Mechanics Insight into the Microwave Nucleation of $SrTiO_3$ Nanospheres, The Journal of Physical Chemistry C, 116 (2012) 24792-24808.

[54] C. Himcinschi, I. Radu, R. Singh, W. Erfurth, A.P. Milenin, M. Reiche, S.H. Christiansen, U. Gösele, Relaxation of strain in patterned strained silicon investigated by UV Raman spectroscopy, Materials Science and Engineering: B, 135 (2006) 184-187.

[55] Y.T. Chua, A.R. Mohamed, S. Bhatia, Oxidative coupling of methane for the production of ethylene over sodium-tungsten-manganese-supported-silica catalyst (Na-W-Mn/SiO_2), Applied Catalysis A: General, 343 (2008) 142-148.

[56] J. Shan, F. Raziq, M. Humayun, W. Zhou, Y. Qu, G. Wang, Y. Li, Improved charge separation and surface activation via boron-doped layered polyhedron $SrTiO_3$ for co-catalyst free photocatalytic CO_2 conversion, Applied Catalysis B: Environmental, 219 (2017) 10-17.

[57] Y. Xu, L. Yu, C. Cai, J. Huang, X. Guo, A study of the oxidative coupling of methane over SrO-La_2O_3/CaO catalysts by using CO_2 as a probe, Catalysis Letters, 35 (1995) 215-231.

[58] Y. Cai, L. Chou, S. Li, B. Zhang, J. Zhao, Selective Conversion of Methane to C_2 Hydrocarbons Using Carbon Dioxide over Mn-$SrCO_3$ Catalysts, Catalysis Letters, 86 (2003) 191-195.

[59] X. Liang, C. Wu, X. Yu, W. Huang, H. Yin, Pd Doped $La_{0.1}Sr_{0.9}TiO_3$ as High-Temperature Water-Gas Shift Catalysts: In-Situ Formation of Active Pd Phase, Catalysis Letters, (2018).

[60] C. Hammond, S. Conrad, I. Hermans, Oxidative methane upgrading, ChemSusChem, 5 (2012) 1668-1686.

[61] R. Ghose, H.T. Hwang, A. Varma, Oxidative coupling of methane using catalysts synthesized by solution combustion method: Catalyst optimization and kinetic studies, Applied Catalysis A: General, 472 (2014) 39-46.

[62] D. Wolf, M. Slinko, E. Kurkina, Baerns, Kinetic simulations of surface processes of the oxidative coupling of methane over a basic oxide catalyst, Applied Catalysis A: General, 166 (1998) 47-54.

[63] E. Iwamatsu, Kinetic analysis of the oxidative coupling of methane over Na^+-doped MgO, Journal of Catalysis, 117 (1989) 416-431.

[64] S.C. Oh, Y. Lei, H. Chen, D. Liu, Catalytic consequences of cation and anion substitutions on rate and mechanism of oxidative coupling of methane over hydroxyapatite catalysts, Fuel, 191 (2017) 472-485.

[65] K. Takanabe, E. Iglesia, Mechanistic Aspects and Reaction Pathways for Oxidative Coupling of Methane on $Mn/Na_2WO_4/SiO_2$ Catalysts, The Journal of Physical Chemistry C, 113 (2009) 10131-10145.

[66] M. Sohrabi, B. Dabir, A. Eskandari, R.D. Golpasha, Some aspects of kinetics and mechanism of the oxidative coupling of methane, Journal of Chemical Technology & Biotechnology: International Research in Process, Environmental AND Clean Technology, 67 (1996) 15-20.

[67] N.R. Farooji, A. Vatani, S. Mokhtari, Kinetic simulation of oxidative coupling of methane over perovskite catalyst by genetic algorithm: Mechanistic aspects, Journal of Natural Gas Chemistry, 19 (2010) 385-392.

[68] E.E. Miro, J.M. Santamaria, E.E. Wolf, Oxidative coupling of methane on alkali metal-promoted nickel titanate: II. Kinetic studies, Journal of Catalysis, 124 (1990) 465-476.

[69] B. Christian Enger, R. Lødeng, A. Holmen, A review of catalytic partial oxidation of methane to synthesis gas with emphasis on reaction mechanisms over transition metal catalysts, Applied Catalysis A: General, 346 (2008) 1-27.

[70] T. Hayakawa, A.G. Andersen, M. Shimizu, K. Suzuki, K. Takehira, Partial oxidation of methane to synthesis gas over some titanates based perovskite oxides, Catalysis Letters, 22 (1993) 307-317.

[71] M. Sohrabi, B. Dabir, A. Eskandari, R.D. Golpasha, Some Aspects of Kinetics and Mechanism of the Oxidative Coupling of Methane, Journal of Chemical Technology & Biotechnology, 67 (1996) 15-20.

Chapter 4. Fabrication of Pillared ZSM-5 Framework for Shape Selectivity of Ethane Dehydroaromatization

Abstract

Ethane, the second major component of shale gas, is a prospective raw feedstock to valuable chemicals and fuels. Innovative pillared ZSM-5 with various lamellar thicknesses and Si/Al ratios were successfully synthesized with the dual-template method. 1% molybdenum species were dispersed over these lamellar ZSM-5, and evaluated for ethane dehydroaromatization. The influence of zeolite morphology and texture property for the reduction/acidity nature of MoO_x species were investigated by XRD, SEM, nitrogen(N_2) sorption, H_2-TPR/TPO and NH_3-TPD. Strong acidity not only increases ethane conversion and aromatic selectivity, but intensely induces surface coking. Therefore, moderate Si/Al ratio maintains a favorable option to balance catalytic reactivity and stability. Thicker zeolite layers with a long diffusion path exhibited fair ethane conversion, but high aromatization yield. It is of significant importance that Mo/MFI-50(T8) catalyst (Si/Al=50, 210 nm layer thickness) demonstrated excellent regenerability during multi-cycle reaction/oxidation operation, which could be a promising system for industrial optimization and process deployment.

4.1 Introduction

With the global shale gas revolution, there are on-growing academia/industrial interests for utilizing C_1-C_4 compounds as the emerging resources for energy and chemical demands. Ethane, the second-concentrated component in natural gas and shale gas, is considered as an environmentally-benign resource for catalytic combustion or conversion. The price of ethane is extraordinary cheap because ethane is a by-product and waste from pipeline compression. In contrast, benzene, toluene and xylene (BTX) are the "building-block" chemicals in many applications, such as the polymer, medical or fragrance industries. The conventional scheme in which BTX is derived from naphtha reforming or oil thermal cracking could hardly meet the fast-growing market demand in recent years. Consequently, non-oxidative dehydro-aromatization of ethane, instead of methane, provides an economically-viable and technical-feasible option for BTX and H_2 production.

Zeolite-supported transition metals have been intensively investigated for the dehydroaromatization reaction. Particularly, HZSM-5 zeolite has been used for many decades in catalytic dehydroaromatization (DHA) of methane due to its acidic and shape selective properties[1, 2]. However, methane DHA requires high reaction temperature and sometimes requires other pretreatment such as nonthermal plasma activation, to achieve higher aromatic yield[3, 4]. Consequently, with the difficulty in direct methane DHA, there is emerging research focusing on ethane DHA. Krogh et al.[5] used Re/HZSM-5 to achieve 65% aromatic selectivity to BTX (benzene, toluene, xylene) under 550 °C. Chetina et al.[6] discovered that platinum and gallium doped HZSM-5 catalyst can achieve 64% aromatic selectivity under 550 °C. ZnO supported over HZSM-5 generally demonstrated >60% ethane conversion with >50% BTX selectivity[7, 8]. Mo species over ZSM-5 zeolite are still being considered as a potential catalyst

for ethane DHA, even though they have smaller reactivity compared to Ga, Zn and Pt catalysts. In academia, Mo/HZSM-5 has been extensively studied for methane-DHA[4, 9-13]. However, the fast deactivation of this catalyst system due to surface coke deposition and the migration of active sites under high-temperature conditions make it very difficult to scale-up for industrial deployment[14-22].

The catalytic mechanism of the ethane DHA reaction over Mo-based catalyst has been hypothesized as a sequential pathways [23-27]: (1) C-H breakage and dehydrogenation of ethane molecules occurred over MoCx or oxycarbide structures anchored on acid sites located in the micro-channels of ZSM-5; (2) the produced ethylene oligomerized via cyclization to benzene or other aromatics over acidic sites. The bifunctional zeolite acidic sites, namely, anchoring the Mo structure and serving as catalytic active sites in oligomerization of ethylene, are both important for the aromatics formation. In addition, ethylene intermediates could re-adsorb over metallic sites for further aromatization[8, 28]. Therefore, catalytic performance of ethane dehydro-aromatization can be fundamentally affected by the distribution/location of Mo species, surface acidity and pore structures.

Compared to conventional microporous zeolites, micro- or mesoporous zeolites with lamellar structures allow the integration of high catalytic activities and fast molecular diffusion[29]. In previous reports, dual-functional templates and diquaternary ammonium-type surfactants have been successfully applied for preparing ZSM-5 zeolites with lamellar structures[30, 31]. A typical dual-functional template is composed of hydrophilic head (quaternary nitrogen atoms) and hydrophobic tails (long alkyl chains). Pentasil structures form in the presence of quaternary nitrogen atoms, and the growth of crystals along b-axis was limited by the long alkyl

chains in the zeolitization process. The micro-mesopore ratio of lamellar ZSM-5 zeolites could be controlled by applying the similar template employing the second structure directing agent (SDA), such as Tetrapropylammonium Hydroxide (TPAOH), or Cetyltrimethylammonium Bromide (CTAB)[32, 33]. Consequently, two-dimensional ZSM-5 nanosheet structures can be fabricated by the presence of two functional groups, which act as a “pillar” after calcination. In addition to surface-active structure, micro/mesopores structures of zeolite framework restrict mass diffusion rates of reactive molecules and surface intermediates, which play a key role for controlling reactivity and selectivity. For a given zeolite framework, the design strategies are generally associated with the change of crystal size, unit-cell volume, morphology[34-36]. In ethane-DHA, the desorption of ethylene intermediates can be accelerated from the catalytic surface and then diffuse from mesoporous structure of zeolite particles, skipping further dehydrogenation and oligomerization to produce aromatics[37, 38]. Furthermore, ZSM-5 particles at the nanoscale possesses high mesopores ratio and short diffusion paths. Big molecules like 1-hexene and aromatics could diffuse between the reaction gas flow and inside the zeolite. Consequently, nano-sized zeolite particles and the meso/macropores framework enable effective mass diffusion, which can notably increase BTX yields during methane aromatization. Pillared ZSM-5, with hierarchical pores, could amplify the mass/heat transfer, which has successfully been demonstrated in the application of ethanol dehydration, monomolecular conversion of propane and isobutene and alkylation of benzyl alcohol with mesitylene reactions[39-41]. This enhanced mass/heat transfer capacity is supposed to be applicable to the DHA reaction. However, very few studies have been reported to directly associate the thickness of lamellar layers with reactant diffusion, Si/Al ratios, surface acidities, as well as catalytic reactivity of ethane-DHA reaction.

During the aromatization reaction, carbon deposition as polyaromatic or graphite species rapidly accumulates over the external surface, blocking the mass transfer in the porous channel, or covering the active Mo species active sites and *Brønsted* acidic sites, resulting in continuous catalytic deactivation[42, 43]. In the last decades, significant efforts have been attempted to address this issue, such as the recent breakthrough of Fe@SiO_2 used at very high temperature during methane-DHA reaction[44]. However, to the best of our knowledge, the formation of carbonaceous deposit is still inevitable, even at laboratory-scale performance testing.

In this study, a regenerable MoO_x/lamellar ZSM-5 is explored based on the strategy of optimizing micro/mesopores structure of zeolite framework, targeting high ethane conversion and aromatic selectivity by optimizing the Si/Al ratio, surface acidity and diffusion path. A series of lamellar ZSM-5 zeolites with controllable thicknesses will be synthesized, the influence of Si/Al ratio of lamellar ZSM-5 zeolite on catalytic performance will be evaluated for the ethane-DHA reaction. Mass diffusion in lamellar zeolites will be optimized by adjusting the hierarchical micro-mesoporous structure, consequently mitigating catalytic deactivation. Different from conventional strategies to minimize catalytic deactivation, easy regeneration of spent catalyst would be more applicable for realistic industrial practices. Therefore, detailed examination of catalytic regenerability/stability will be evaluated during cyclic ethane-DHA/oxidation regeneration operations.

4.2 Experimental Section

4.2.1 Catalyst Preparation

4.2.1.1 Surfactant Synthesis

The surfactants used for zeolite synthesis were prepared by following a previous report[30, 41]: 12.45 g 1-Bromodocosane (98%, TCI) was dissolved in 150 mL toluene (99.5%, Fisher) and 52.22 g N,N,N',N'-tetramethyl-1,6-diaminohexane (98.5%, ACROS Organics) was dissolved in 150 mL acetonitrile (99.9% Fisher). These solutions were evenly mixed and stirred for 1 h, and then refluxed at 353 K for 10 h. After cooling to room temperature, the precipitate was filtered, washed with diethyl ether and dried overnight. The product has been identified as [$C_{22}H_{45}$-$N^+(CH_3)_2$-C_6H_{12}-$N(CH_3)_2$]Br. 11.22 g of [$C_{22}H_{45}$-$N^+(CH_3)_2$-C_6H_{12}-$N(CH_3)_2$]Br and 6.73 g of 1-bromohexane (99%, ACROS Organics) were added into acetonitrile (100 mL), stirred for 1 h and refluxed at 353 K for 10 h. After cooling to room temperature, the precipitated products were filtered, washed with diethyl ether and dried in a vacuum oven at 373 K overnight. The final surfactant has been analyzed as [$C_{22}H_{45}$-$N^+(CH_3)_2$-C_6H_{12}-$N^+(CH_3)_2$-C_6H_{13}]Br_2 ($C_{22\text{-}6\text{-}6}Br_2$).

4.2.1.2 Dual Template Synthesis of Lamellar MFI (ZSM-5) with Different TPAOH Amounts

The zeolites were synthesized with the chemical formula as: $30Na_2O$: $1Al_2O_3$: $100SiO_2$: $10C_{22\text{-}6\text{-}6}Br_2$: xTPAOH: $4000H_2O$, where x equaled to 0, 2, and 8, respectively. Taking ZSM-5, where x equaled to 8, as an example, the detailed procedure is presented as follows: 0.70 g sodium hydroxide (97%, Fisher) was dissolved in 2.09 g $C_{22\text{-}6\text{-}6}Br_2$ and 15 g DI water mixture. 1.17 g TPAOH (40%, TCI) was dropwise added to the prepared solution followed by adding 0.19 g aluminum sulfate hydrate ($Al_2S_3O_{12}\cdot 18H_2O$, 98%, Fisher) and 3.58 g sulfuric acid (60%, Fisher) and 3.06 g DI water with vigorous stirring. Subsequently the mixture was heated at 343 K to obtain

a clear solution. At room temperature, 6.12 g TEOS (98%, ACROS Organics) was dropwise added into the solution and stirred for 20 h at room temperature. The resulted gel was transferred into a Teflon-lined stainless-steel autoclave and crystallized for 5 days at 423 K. The product was filtered and washed with DI water and then dried at 373 K overnight. The samples were calcined at 823 K for 6 hours in air with 10K/min heating rate. The as-synthesized zeolites were named as MFI-50(T0), MFI-50(T2) and MFI-50(T8), whereas 0, 2 and 8 equaled to the TPAOH addition in the synthesis formulation and 50 was corresponding to Si/Al ratios of 50. In comparison, commercial MFI zeolites with the same Si/Al ratio were obtained from Zeolyst Company.

4.2.1.3 Dual Template Synthesis of Lamellar MFI of Different Si/Al Ratios

To prepare lamellar MFI zeolites with different Si/Al ratios, the formula was adjusted as follows: $30Na_2O$: $xAlO_2$: $100SiO_2$: 10 $C_{22\text{-}6\text{-}6}Br_2$: 8TPAOH: $4000H_2O$, in which x equaled to 0.5, 1 and 2, and corresponding to different Si/Al ratios of 100, 50 and 25 respectively. The Si/Al ratios of zeolite samples were adjusted by adding various amount of aluminum sulfate hydrate. The as-synthesized zeolites were identified as MFI-25(T8), MFI-50(T8) and MFI-100(T8), whereas the numbers 25, 50, 100 represented Si/Al ratio of zeolites. The Si/Al ratios of all the zeolites are analyzed and presented in Table 1.

4.2.1.4 Synthesis of Supported Mo/MFI Zeolites

The as-calcined MFI samples were firstly ion-exchanged with 1 M aqueous NH_4NO_3 (99%, ACROS Organics) at 353 K for 8 h, subsequently washed with DI water, and dried at 343 K overnight. Commercial MFI zeolites were received as NH_4^+ form.

1 wt.% of MoO_3/MFI catalysts were prepared by incipient wetness impregnation of aqueous ammonia molybdate tetrahydrate solution as precursor (99%, ACROS Organics). After

impregnation, the catalysts were dried in ambient conditions overnight, and then calcined in air at 773 K for 2 h. The Mo/MFI zeolites with different Si/Al ratios were identified as Mo/MFI-25(T8), Mo/MFI-50(T8), Mo/MFI-100(T8), while the catalysts that were prepared by adding different amounts of TPAOH in the synthesis recipe were named as Mo/MFI-50(T0), Mo/MFI-50(T2), and Mo/MFI-50(T8).

4.2.2 Catalyst Evaluation

4.2.2.1 Ethane Aromatization Reaction:

Catalytic performance of Mo/MFI for ethane dehydro-aromatization was studied at 923 K, atmospheric pressure with a space velocity of 1920 mL/(g_{cat}·h). 500 mg of catalyst was loosely loaded in a fixed bed reactor (9 mm ID.) and purged in N_2 (10 mL/min, UHP, Air gas) at 923 K for 1 h. After pretreatment, 80% C_2H_6/He was introduced into the catalyst at 20 mL/min. Since the produced aromatics cannot be detected by on-line GC at experimental condition, the outlet of the fixed bed reactor was connected with a replaceable bubbler containing hexadecane to absorb/condense aromatic products. The exit gas after the bubbler was analyzed by an on-line GC. The C_2H_6 conversion (%), aromatics selectivity (%), aromatics yield (%)were defined as follows:

$$Ethane\ conversion\ (\%) = \frac{moles\ of\ ethane\ reacted}{moles\ of\ ethane\ in\ feed} \times 100 \quad (1)$$

$$Aromatics\ selectivity\ (\%) = \frac{3(moles\ of\ \text{benzene}\ formed)+3.5(moles\ of\ \text{toluene}\ formed)+4(\text{moles of xylene fromed})}{moles\ of\ ethane\ reacted} \times 100 \quad (2)$$

$$Aromatics\ yield\ (\%) = ethane\ conversion\ (\%) \times aromatic\ selectivity\ (\%) \times \frac{1}{100} \quad (3)$$

4.2.2.2 Cyclic Ethane Dehydro-aromatization Reaction-oxidative Regeneration:

The ethane dehydro-aromatization-oxidative regeneration cycles over Mo/MFI-50(T8) and Mo/Commercial MFI were carried out in Micromeritics Autochem 2950 analyzer. 50 mg of catalyst were loosely loaded into a U-tube (9.5 mm ID.) and pretreated at 923 K for 90 min in He (UHP, 50 mL/min). For a typical reaction-regeneration cycle, 20% C_2H_6/He (50 mL/min) was introduced with on-line mass spectrometer for product analysis. After reacting for 15 minutes, the feedstock changed to pure He at the flow rate of 50 mL/min and held for 10 min to flush out residue gas. The catalyst regeneration was conducted in 2% O_2 in He (50 mL/min) at 773 K for 20 min. Each catalyst was tested for four reaction/regeneration cycles.

4.2.3 Catalytic Characterization

Powder X-ray diffraction (XRD) was performed to identify the product structure and calculate the zeolite crystallinity of each catalyst. XRD patterns were obtained using a PANalytical X'Pert Pro XRD system equipped with Ni filtered Cu target Ka radiation (operation at 45 kV, 40 mA, wavelength λ=0.15418 nm). The morphologies and the crystal sizes of the synthesized samples were examined by scanning electron microscopy (SEM). Nitrogen (N_2) sorption analysis was performed using a Micromeritics Tristar 3000 at 77 K, to characterize the porosity, pore sizes, and surface areas of the catalysts. Prior to measurement, samples were degassed under flowing nitrogen at 350 °C for at least 6 h. The specific surface area was calculated using the Brunauer–Emmett–Teller (BET) equation utilizing the adsorption branch.

The H_2-TPR experiment was conducted in a Micromeritics Autochem 2950 analyzer equipped with a TCD detector to study the reducibility and dispersion of Mo phases anchored over the zeolite frameworks. 5 vol% H_2/Ar (20 mL/min) was introduced to the catalyst bed (0.1 g) at

373 K until stable TCD signals were obtained. The reactor was heated at 5 K/min up to 1123K. Temperature-programmed oxidation (TPO) measurements were carried out after the fourth dehydro-aromatization/ regeneration cycle. The spent catalyst was heated from room temperature to 1073 K in a stream of 2 vol% O_2/He (20 mL/min) at the rate of 10 K/min.

NH_3-TPD used the same micro-reactor system as the H_2-TPR. NH_3 adsorption/desorption cycles were performed to evaluate the effect of Si/Al ratios and acidic structure of the synthesized MFI. These studies were performed in four steps: (i) pretreatment, (ii) NH_3 adsorption, (iii) Ar purge, and (iv) temperature-programmed desorption (TPD). During sample pretreatment, the catalysts were dehydrated at 723 K in the mixture of 10 cm^3/min 5%O_2/He anmd 20 cm^3/min Ar for 30 min, and then the gas was switched to pure Ar flow for another 30 min. NH_3 adsorption was performed by exposing the catalyst to 1% NH_3/He (30 cm^3/min) for 15 min at 423 K until NH_3 adsorption was saturated. The residual gas in the reactor was completely purged by UHP Ar. TPD was conducted by heating the catalyst to 723 K at the rate of 10 K/min with on-line MS detection (Omnistar GSD-301, Pfeiffer).

4.3 Results and Discussion

4.3.1 Bulk Structures and Morphology of the Zeolites

XRD patterns of lamellar MFI and commercial MFI zeolites are shown in Fig. 1. The high-angle region of XRD patterns of lamellar MFI-50(T0), MFI-50(T2), MFI-50(T8), MFI-25(T8), MFI-100(T8) zeolites are identical to commercial MFI zeolite, indicating the pentasil-type zeolites are successfully prepared with MFI topology[30, 40]. Table 1 summarized the key parameters of the synthesized zeolites. The crystallinity of MFI-50(T0), MFI-50(T2), MFI-50(T8), MFI-25(T8), MFI-100(T8) zeolites respectively equaled to 56%, 75%, 83%, 105% and 82% as referred to

commercial MFI with 100% crystallinity as standard. This type of pillared ZSM-5 is of numerically poor crystallinity compared to the conventional ZSM-5, partly due to the formation of small crystals (eg. (421) Miller index at 13.8° and (133) Miller index at 24.3° are weak)[29, 30, 32].

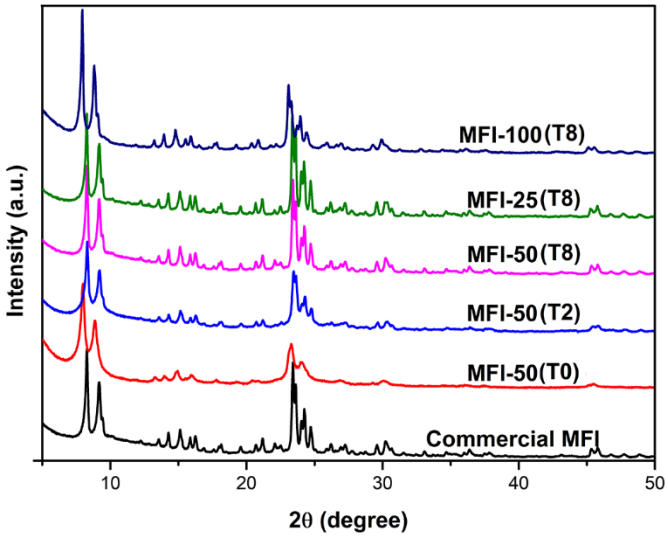

Figure 1. XRD patterns of lamellar MFI-50(T0), MFI-50(T2), MFI-50(T8), MFI-25(T8), MFI-100(T8) and commercial MFI.

Table 1 Key crystalline parameters of various zeolites from XRD result.

Zeolite	Si/Al Ratio	Crystallinity (%)	Layer thickness (nm)
Commercial MFI	50	100*	-
MFI-50(T0)	50	56	35
MFI-50(T2)	50	75	60
MFI-50(T8)	50	88	210
MFI-25(T8)	25	105	-
MFI-100(T8)	100	75	-

*referenced crystallinity of the zeolites

SEM images of the crystal morphologies of the lamellar zeolites are shown in Fig. 2. All zeolite samples consisted of random-oriented nanosheets with different thicknesses, which function as pillars to support a microporous structure. As shown in Fig. 2 (a-c), the thickness of nanosheets increases from ca. 35 nm on MFI-50(T0) to ca. 210 nm on MFI-50(T8). Due to the framework growth of ZSM-5 zeolites, the crystallinity of zeolites in the XRD pattern increases with the increasing of TPAOH/$C_{22\text{-}6\text{-}6}Br_2$ ratio[32, 33]. The b-axis dimension of a single MFI unit cell is 1.9738 nm[30]. The zeolite was synthesized as multilamellar stacking of MFI nanosheets that were three-dimensionally intergrown. As mentioned, the overall thickness of the lamellar stacking was 35, 60 and 210 nm, for MFI-50(T0), MFI-50(T2), MFI-50(T8), respectively. The stackings were proposed to composed of numerous 2.0-nm-thick MFI zeolite framework according to the reports from Ryong Ryoo and colleagues[30, 45]. Compared to MFI-50(T0), the other two zeolites (MFI-50(T2) and MFI-50(T8)) exhibit thicker nanosheets with extra addition of TPAOH, indicating that the formation of crystalline ZSM-5 was not only influenced by the addition of $C_{22\text{-}6\text{-}6}Br_2$, but also the amount of TPAOH. There are random nanosheets aligned with ZSM-5 framework which create hierarchical channels during the hydrotreating[46, 47]. Thicker nanosheets suggested longer diffusion paths, which could directly change the overall catalytic reactivity and selectivity[30]. Moreover, the Si/Al ratios have noticeable impact on the morphologies as shown in Fig. 2c to 2e. A fraction of a nanosheet has converted to coffin-shape particles among the MFI-25(T8) zeolite sample, while MFI-100(T8) exhibits flower-like morphology with various thicknesses of nanosheet. For comparison, commercial ZSM-5 zeolite demonstrates spherical structure, which is totally different from nanosheet structure of lamellar MFI (Fig 2e).

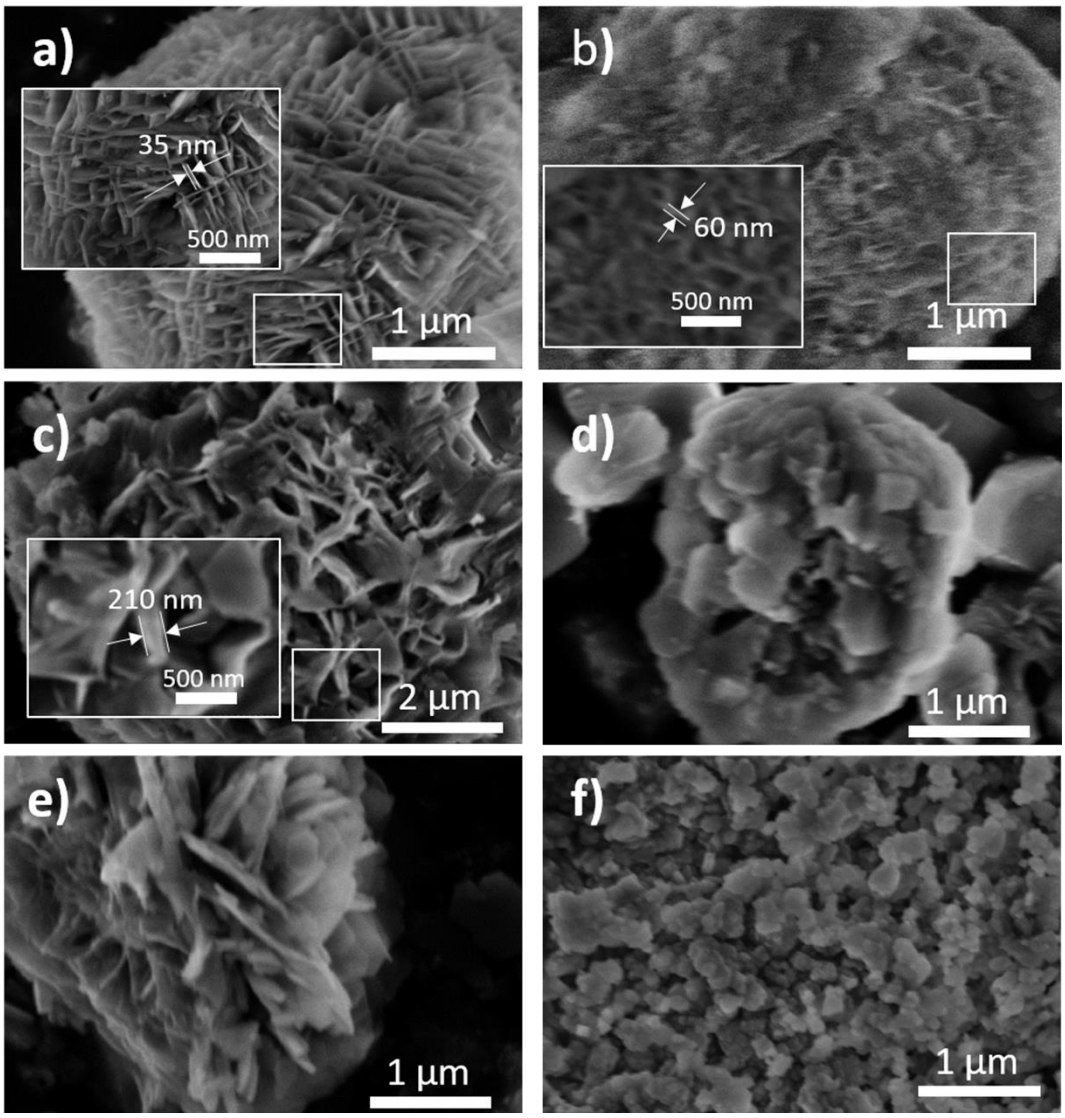

Figure 2. SEM images of a) MFI-50(T0); b) MFI-50(T2); c) MFI-50(T8); d) MFI-25(T8); e) MFI-100(T8); f) commercial MFI

N_2 adsorption-desorption isotherms were carried out to reveal the porosity features of zeolites. All the samples exhibit type-IV N_2 isotherms with a hysteresis loop, corresponding to capillary condensation in mesopores[48], as depicted in Fig. 3a. For MFI-50(T0), MFI-50(T2) and MFI-50(T8), the decrease in adsorption volume at the low pressure region ($P/P_0 < 0.45$) indicates that the thicker layer expose less micropores (Table 2). Moreover, Fig. 3b reveals that the mesopores at the range of 3-7 nm disappear with a high quantity of TPAOH added to the synthesis

recipe, while those at the range <3 nm increase slightly. This pore structure tendency is consistent with previous findings[32, 40]. For MFI-25(T8) and MFI-100(T8), morphologies and Si/Al ratio have a vital influence on porosities. As Si/Al ratio increases, the increase of mesopore volume and the decrease of micropore volume can be observed (Table 2). The total pore volumes of most synthesized MFI are larger than those of commercial MFI. Therefore, most of the synthesized zeolites are more capable to accommodate coke than the commercial zeolites. The hierarchy factor, defined as the product of the relative micropore volume and the relative mesopore surface area, $(V_{micro}/V_{total})\times(S_{meso}/S_{BET})$, is used to describe the interplay between the catalytic function located in the micropores and the accessibility function provided by the mesopores in the hierarchical zeolites[49]. The order of hierarchy factor of synthesized zeolites with various TPAOH adding amounts is: MFI-50(T0) < MFI-50(T2) < MFI-50(T8). For MFI samples with different Si/Al ratios, the order of hierarchy factor order is MFI-25(T8) < MFI-50(T8) < MFI-100(T8), since the relative increase of meso-porosity is higher than the relative decrease of micro-porosity in these zeolites. Both tailoring of the TPAOH concentration and Si/Al ratio in the MFI synthesis process results in tunable meso-microporosity in lamellar MFI catalysts.

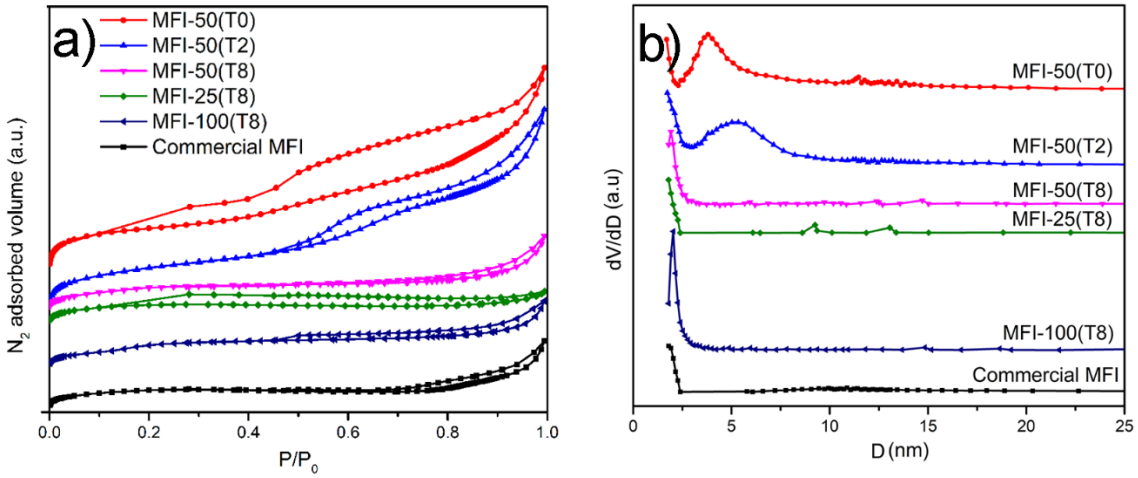

Figure 3. a) N_2 adsorption-desorption isotherms and b) pore size distributions as derived from N_2 sorption of the zeolites. The pore size distribution were calculated by using Barrett-Joyner-Halenda (BJH) algorithm from the adsorption branch.

Table 2 Textural property of zeolites measured by N_2 Adsorption-Desorption

Catalyst	S_{BET}[a] (m^2g^{-1})	S_{micro}[b] (m^2g^{-1})	S_{meso}[b] (m^2g^{-1})	V_{total}[c] (cm^3g^{-1})	V_{micro}[b] (cm^3g^{-1})	V_{meso}[d] (cm^3g^{-1})	Hierarchy factor[e]
Commercial MFI	263.8	206.7	57.1	0.228	0.108	0.120	0.10
MFI-50(T0)	424.9	280.6	144.3	0.515	0.145	0.370	0.10
MFI-50(T2)	422.7	226.0	196.7	0.506	0.118	0.388	0.11
MFI-50(T8)	319.5	214.9	104.6	0.257	0.112	0.145	0.14
MFI-25(T8)	320.2	270.6	49.6	0.191	0.143	0.048	0.12
MFI-100(T8)	314.2	150.0	164.2	0.238	0.080	0.158	0.18

a: Determined from multipoint BET method. *b*: Determined from t-method. *c*: Determined from adsorbed volume at P/P_0=0.99. *d*: $V_{meso} = V_{total} - V_{micro}$ *e*: Described as the product $(V_{micro}/V_{total}) \times (S_{meso}/S_{BET})$.

4.3.2 Temperature-Programmed Reduction Analysis

The reducibility of MoO_x/ZSM-5 species was studied by H_2-TPR. Previous MAS NMR spectra suggested that surface MoO_x could migrate into the structural channels during calcination, and anchor over conventional ZSM-5 frameworks as active sites[50, 51]. Moreover, DFT calculation and UV-Raman study also demonstrated that Mo oxide species preferentially anchor

on framework Al sites[52, 53]. In this study, TPR profiles are deconvoluted into four peaks (as shown in Fig. 4), and the corresponding hydrogen consumptions are summarized in Table 3. Peak I at the lowest reduction temperature (~530 K) is assigned to partial reduction of amorphous polymolybdates (Mo^{6+}), peak II at ~640 K and peak III at ~790 K are corresponding to the reduction of octahedrally-coordinated Mo^{6+} in MoO_3 to Mo^{4+}. Peak IV with the highest reducing temperature (~940 K) is assigned to the sequential reduction of Mo^{4+} to metallic Mo(0)[54-56]. The reduction of amorphous polymolybdates (peak I) are not pronounced in all Mo/MFI samples, which confirmed the successful preparation of highly-dispersed of Mo species over the synthetic zeolites. The reduction of Mo^{4+} to metal Mo (0) dominates the TPR profile, and only a small fraction of Mo^{4+} was reduced to metal Mo (0) over Mo/MFI-50(T0) catalyst. Mo/MFI-50(T8) catalyst indicates more than 3-fold increase of hydrogen consumption of peak IV than that of Mo/MFI-50(T0). Therefore, thicker layers introduced by TPAOH addition contributed to the reducibility from Mo^{4+} to metal Mo. As summarized in Table 3, the relative concentration of reducible Mo^{4+} in various catalysts decreases with layer thickness in the order: MFI-50(T8) > MFI-50(T2) > MFI-50(T0), while that of the catalysts with different Si/Al ratios decreases in the order: Mo/MFI-25(T8) >Mo/MFI-100(T8) > Mo/MFI-50(T8).

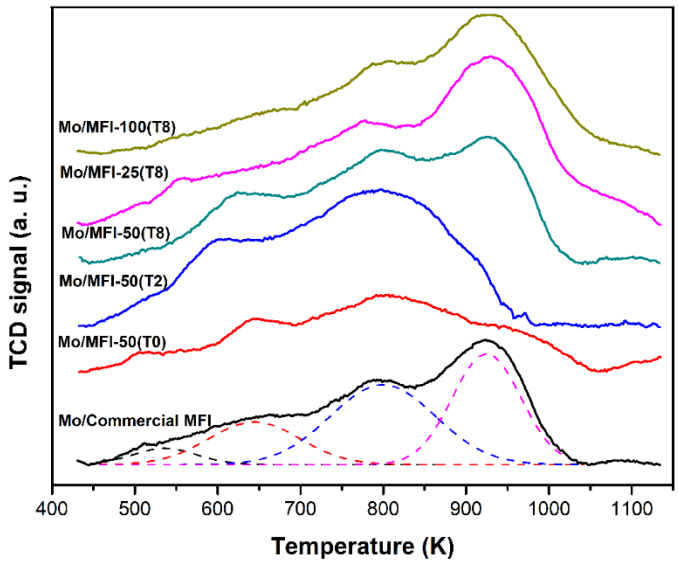

Figure 4. H_2-TPR profiles for fresh Mo/MFI-50(T0), Mo/MFI-50(T2), Mo/MFI-50(T8), Mo/MFI-25(T8), Mo/MFI-100(T8) catalysts

Table 3 Numerical results of TPR experiments on Mo loaded catalysts

Catalyst		Peak I	Peak II	Peak III	Peak IV
Mo/Commercial MFI	Temperature (K)	536	644	799	924
	H_2 consumption (µmol/g)	**13**	**49**	**106**	**96**
Mo/MFI-50(T0)	Temperature (K)	541	646	808	964
	H_2 consumption (µmol/g)	**14**	**23**	**142**	**15**
Mo/MFI-50(T2)	Temperature (K)	535	633	785	879
	H_2 consumption (µmol/g)	**8**	**100**	**168**	**42**
Mo/MFI-50(T8)	Temperature (K)	519	633	807	932
	H_2 consumption (µmol/g)	**3**	**59**	**174**	**70**
Mo/MFI-25(T8)	Temperature (K)	560	634	778	925
	H_2 consumption (µmol/g)	**2**	**85**	**87**	**203**
Mo/MFI-100(T8)	Temperature (K)	569	680	795	924
	H_2 consumption (µmol/g)	**8**	**48**	**68**	**163**

4.3.3 NH_3-TPD Analysis

The NH_3-TPD measurements were performed to analyze the acid distribution and concentrations on the zeolite surface. As shown in Figure 5, two desorption peaks were obtained by conducting deconvolution at low temperature around 530 K and high temperature around 700 K, which is consistent with reported data[57, 58]. These two peaks correspond to weak-acid sites and strong-acid sites on the zeolite surface, respectively. It is widely accepted that the Al in the zeolitic framework causes strong-acid sites, whereas framework terminal Si mainly brings weak acidity[59, 60]. The results indicated the concentration of strong-acid sites associated with Al are dominant among every zeolite.

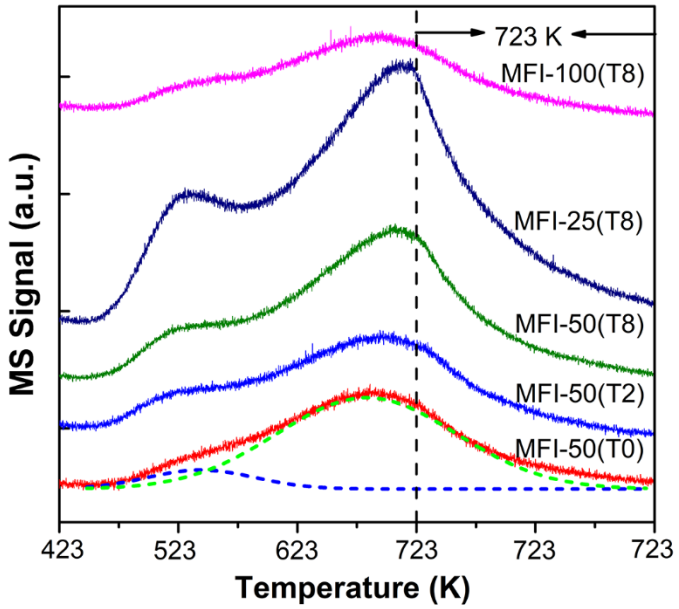

Figure 5. NH_3-TPD profiles of MFI-50(T0), MFI-50(T2), MFI-50(T8), MFI-25(T8) and MFI-100(T8).

Table 4 NH_3-TPD data of synthesized ZSM-5

Catalyst	Distribution and concentration of acid sites (μmol NH_3/g)		
	Region Weak	Region Strong	Total
MFI-25(T8)	118	443	561
MFI-100(T8)	12	132	144
MFI-50(T8)	60	280	340
MFI-50(T2)	27	154	181
MFI-50(T0)	19	150	169

The acidities of the synthesized ZSM-5 are summarized in Table 4. The MFI-25(T8), MFI-50(T8) and MFI-100(T8) clearly exhibited different scales of acid sites, suggesting that the change of the Si/Al ratio is an effective approach to modify surface acidity. Moreover, the MFI-50(T8) possessed a larger amount of acidic sites than MFI-50(T2) and MFI-50(T0), though they were in the same Si/Al ratio of 50. Consequently, the extra addition of TPAOH in MFI-50(T2) and MFI-50(T8) promoted the Al embedding into the framework.

4.3.4 Ethane Dehydro-aromatization on Mo/MFI Catalysts with Different Layer Thickness

All synthetic/commercial zeolites demonstrated negligible aromatic productivity. The reaction profiles of ethane conversion with time-on-stream (TOS) over Mo/MFI-50(T0), Mo/MFI-50(T2), Mo/MFI-50(T8) and Mo/commercial MFI with the *same Si/Al ratio (Si/Al=50), but different layer thickness* are presented in Figure 6a. Among various catalysts, Mo/MFI-50(T0) with the thinnest nanosheets exhibits the best performance in ethane conversion, while Mo/MFI-50(T8) with the thickest nanosheets shows fair performance. During the initial period of dehydro-aromatization reaction, gaseous ethane must diffuse through the channels of zeolite framework, and then contact the reduced Mo species[61-63]. Thus, the thicker the nanosheet, the longer

diffusion path is necessary for the reactant to pass through. Once the intermediates and the products were mixed with ethane, the TOF (turn-over-frequency) of ethane on Mo active sites was negatively affected by longer channels, and results in lower ethane conversion. Moreover, from NH_3-TPD results, the concentration of acid sites on MFI-50(T2) (181 μmol NH_3/g) is comparable to that of MFI-50(T0) (169 μmol NH_3/g), however Mo/MFI-50(T2) shows lower ethane conversion but higher aromatic selectivity. From Fig. 6 c and d, it is found that the synthesized pillared MFI samples presented the higher produced ethylene flow rate but lower aromatic yields than those of commercial MFI, which is attributed to the less shape selectivity of the lamellar zeolite samples.

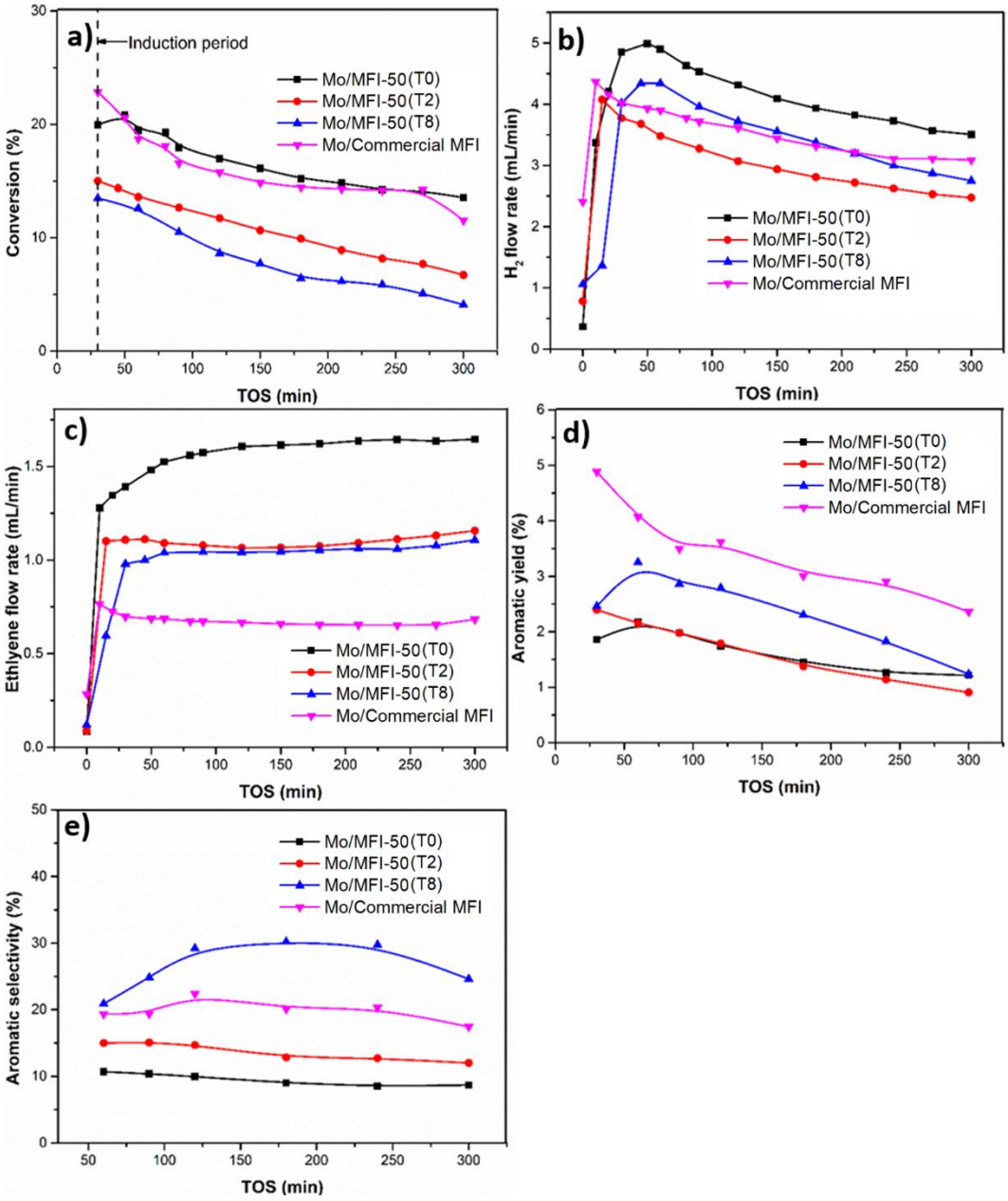

Figure 6. Mo/MFI-50(T0), Mo/MFI-50(T2), Mo/MFI-50(T8) and Mo/Commercial MFI catalysts in ethane aromatization reaction with the TOS of a) ethane conversion, b) H_2 flow rate, c) C_2H_4 flow rate, d) aromatic yield, e) aromatic selectivity.

Figure 6b, c, and d depict the productivities of H_2, C_2H_4 and the aromatic yield (containing benzene and toluene). The ratio of benzene to toluene in the product of Mo/MFI-50(T8) catalyst reached 1.85, which is greater than that of Mo/MFI-50(T0) and Mo/MFI-50(T2) catalyst, whose ratio equaled 1.35 and 1.53, respectively. Interestingly, Mo/MFI-50(T0) exhibited the highest C_2H_6 conversion and H_2/C_2H_4 productivity, but the yield of aromatic was the lowest. Mo/MFI-50(T8) exhibited higher aromatic yield compared to Mo/MFI-50(T0) and Mo/MFI-50(T2) despite lower ethane conversion, suggesting that the thicker zeolite layer is beneficial for aromatic yields. Based on the carbon balance, it is remarkable that the Mo/MFI-50(T8) catalyst showed the highest aromatic selectivity, even compared to the referential Mo/commercial ZSM-5 with spherical structure from SEM observation. Compared with Mo/MFI-50 (T0), both Mo/MFI-50(T2) and Mo/MFI-50(T8) catalysts with thicker layers demonstrated lower ethane conversion but higher aromatic yield. Therefore, it is conclusive that the pillar layers with long diffusion path plays a critical role in improving the formation of aromatics.

4.3.5 Ethane Dehydro-aromatization on Mo/MFI Catalysts with Different Si/Al Ratios

It is widely accepted that alumina defects provide nucleation sites during the formation of the ZSM-5 structure and Brønsted acidity[52, 64]. In this study, the influence of Si/Al ratio and Al/Mo for the reactivity of ethane dehydro-aromatization was studied with Mo/MFI-25(T8), Mo/MFI-50(T8) and Mo/MFI-100(T8), in which the numbers (25, 50, 100) represents various Si/Al ratios. Because this study focuses on the zeolite structure, the same Mo loading (1%) was applied. Therefore, Si/Al ratio is inversely with Al/Mo ratios, which can serve as an indicator of the amount of acid sites taken by Mo for aromatization. As shown in Figure 7, the ethane conversion on the Mo/MFI-25(T8) catalyst with lowest Si/Al (25) dropped dramatically after the initial period, while Mo/MFI-50(T8) (Si/Al=50, Al/Mo=3.14) and Mo/MFI-100(T8) (Si/Al=100,

Al/Mo=1.57) decreased steadily. It should be noted that simultaneous downtrend of H_2 and aromatic yields can be observed in Figure 7b and d. Stable ethylene yield was obtained over all catalysts after 30 mins reaction. Mo/MFI-25(T8) catalyst exhibited the highest initial activity, while Mo/MFI-100(T8) catalyst indicated the lowest aromatic yield. On the other hand, NH_3-TPD profiles demonstrated that Si/Al ratio of zeolite directly correlated with the surface acidity of Mo/MFI catalyst. As shown in Table 4, Mo/MFI-25(T8) represents the highest surface acidity among various synthesized zeolites. Considering negligible reactivity of pure zeolites, it is Mo species neighboring *Brønsted* acid sites that synergistically convert ethane into aromatics, and the Si/Al ratios greatly affect initial reaction performance[52].

Despite the trace amount polymolybdates identified by H_2-TPR, Mo is mainly highly-dispersed in all catalysts. There are three types of MoO_x allocated in the zeolite framework: anchoring at double Al sites, single Al sites and surface Si sites. It is accepted that the C-H bond activation energy over the Mo nanostructures anchored are increasing in the order: double Al acid sites > single Al acid sites > external Si sites[52, 53, 65]. In MFI-25(T8) and MFI-50(T8), the Al/Mo ratio are 6.28 and 3.14, respectively (Table 5). Therefore, Mo species are likely to anchor at double/single Al sites, which may contribute to the higher initial aromatic yield of MFI-25 (T8).

Table 5. The Si/Al and Al/Mo ratio for samples

Sample	**Si/Al Ratio**	**Al/Mo Ratio**
MFI-25(T8)	25	6.28
MFI-50(T0)/(T2)/(T8)	50	3.14
MFI-100 (T8)	100	1.57

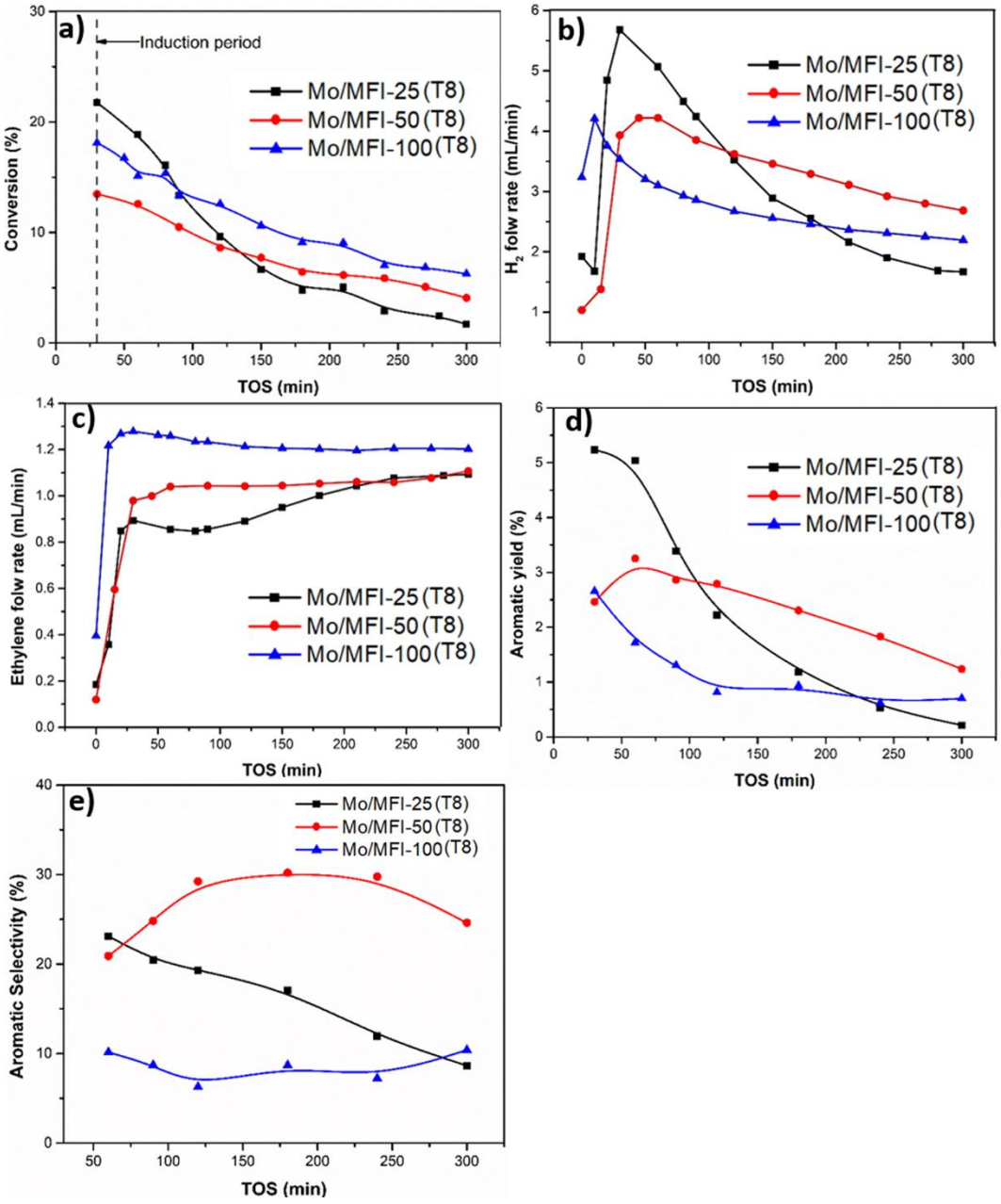

Figure 7. Mo/MFI-25(T8), Mo/MFI-50(T8), Mo/MFI-100(T8) catalysts in ethane aromatization reaction with the TOS of a) ethane conversion, b) H_2 flow rate, c) C_2H_4 flow rate, d) aromatic yield, e) aromatic selectivity.

The prepared Mo/MFI catalysts indicated different deactivation behavior: the Mo/MFI-25(T8) catalyst with the lowest Si/Al ratio remarkably increases ethane conversion and aromatic

selectivity, though fast deactivation was observed as well. For Mo/MFI-100(T8), Mo sites over the lowest acidity results in the lowest ethane conversion, lowest ethane/H_2/aromatics productivity and least aromatic selectivity. Instead, Mo/MFI-50(T8) catalyst indicated highest H_2 and aromatic productivity during 250 min reaction. Thus, lamellar zeolites with moderate Si/Al ratio maintains a favorable balance between catalytic activity, high selectivity to aromatics and catalyst stability in ethane aromatization.

4.3.6 Coke Analysis

Coke formed during aromatization reaction is a complicated mixture of polyaromatics and graphitic species which blocks *Brønsted* acidic sites, zeolite micropores and Mo active centers, thus leading to the inevitable decline of catalytic performance[42, 43, 66]. Fig. 8 presents TPO profiles of spent catalysts after continuous aromatization testing at 923 K for 300 min, and the relative areas of each peak were summarized in Table 6.

The amount of the coke deposit content is: Mo/MFI-25(T8) > Mo/MFI-50(T0) > Mo/MFI-50(T2) > Mo/MFI-100(T8) > Mo/MFI-50(T8) ≈ commercial MFI. CO_2 profiles could be deconvoluted into three peaks at ~705, 750 and 830 K[42, 67, 68] as shown in Figure 8. Carbon deposits burned out at 705 K were located at the external surface of the catalytic particles, the peak at 750 K corresponds to the coke associated with the Mo species in the zeolite, whereas the carbon species burning at high temperatures (> 800 K) were mainly from coking anchored over the *Brønsted* acid sites.

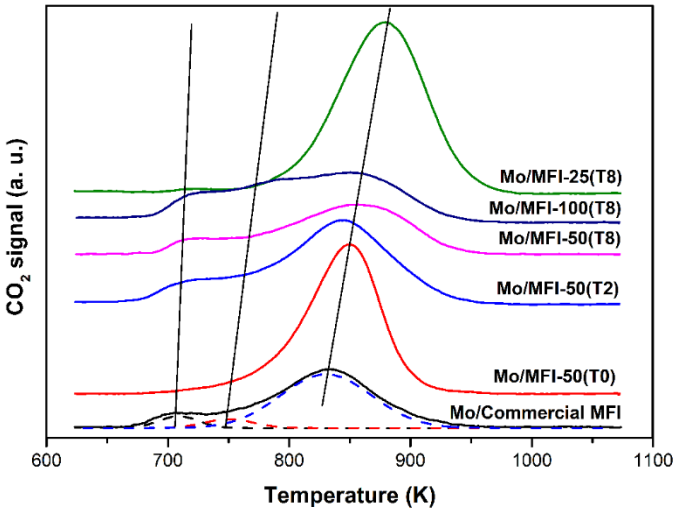

Figure 8. TPO profiles for spent Mo/MFI-50(T0), Mo/MFI-50(T2), Mo/MFI-50(T8), Mo/MFI-25(T8), Mo/MFI-100(T8) catalysts after ethane dehydro-aromatization reactions

Trace carbon deposits over external surface of Mo species are observed at 705 K, which demonstrated that the coking over external surface are negligible for prepared Mo/lamellar zeolites catalyst. On the spent Mo/MFI-25(T8) (Si/Al=25, Al/Mo=6.28), the largest amount of coke appeared on the *Brønsted* acid sites with very few carbon deposits associated with Mo species. In contrary, over the spent Mo/MFI-100(T8) catalyst with less *Brønsted* acidity, carbon deposits mainly associated with Mo species, instead of *Brønsted* sites.

Regarding the spent samples of Mo/MFI-50(T0), Mo/MFI-50(T2), Mo/MFI-50(T8) catalysts with same Si/Al ratio, TPO profiles showed that the nature and amount of deposited coke are associated with zeolite thicknesses. With the thinner nanosheet, carbon deposits were preferable to be formed over *Brønsted* acid sites. Combined with performance data in Figure 7, it is concluded that that the large amount of coke in Mo/MFI-50(T0) catalyst with thinner layer could be induced by high ethane conversion and lower aromatic selectivity, whereas Mo/MFI-50(T8)

catalyst exhibited higher aromatic selectivity as well as less amount of coke deposited on the *Brønsted* acid sites.

Table 6 Numerical results of TPO experiments on used Mo/MFI-T0, Mo/MFI-T2, Mo/MFI-T8(Mo/MFI-50), Mo/MFI-25, Mo/MFI-100 catalysts.

Catalyst	Peak relative area			Total carbon amount
	Peak I	Peak II	Peak III	
Mo/MFI-25(T8)	1	5	100*	106
Mo/MFI-100(T8)	2	42	15	59
Mo/MFI-50(T8)	3	10	34	47
Mo/MFI-50(T2)	3	10	56	69
Mo/MFI-50(T0)	2	11	67	80
Commercial MFI	4	3	38	45

*reference value of peak area

Overall, it is believed that the complicated coking over Mo/lamellar zeolites follows two mechanisms: (1) in the case of lamellar zeolites with high Si/Al ratio, coke mainly covered Mo active sites, whereas only a small fraction of coke associated with *Brønsted* acid sites blocked the channel, ensuring the stability of aromatic selectivity while the ethane conversion dropped; (2) in the case of lamellar zeolites with lower Si/Al ratio, a large amount of coke mainly covered *Brønsted* acid sites and clogged the channels, which would further decrease the ethane conversion. Consequently, a moderate Si/Al ratio of a lamellar zeolite sustained the ethane conversion and aromatic selectivity, which benefited from the balance between hydrocarbons activation over Mo carbide species and modest channel coking over *Brønsted* acid sites.

4.3.7 Oxidative Regenerations and Ethane Aromatization Reaction

Considering surface coking and catalytic deactivation are unavoidable, it is proposed to study aromatization-regeneration cycle for realistic application of ethane aromatization. As

discussed above, it is identified that surface coking is mainly associated with MoCx nanoparticles and strong acidic sites. Therefore, the preservation of the overall framework and the decoking degree should be considered during oxidative regeneration[1, 69, 70]. From the TPO data as shown in Figure 8, oxidative calcination at 823 K can greatly preserve the zeolite structure and avoid catalytic deactivation caused by Mo content[70]. Therefore, all cyclic reaction-regeneration experiments were performed at isothermal 823 K in this study.

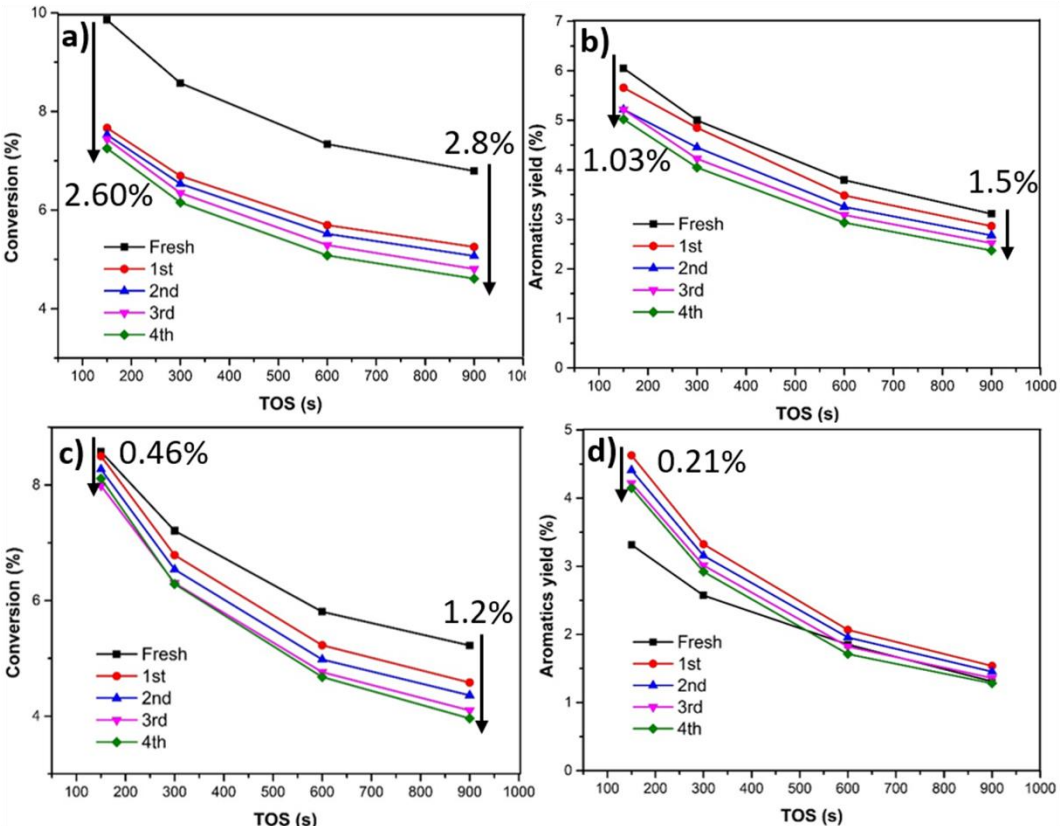

Figure 9. Ethane dehydro-aromatization reaction-regeneration cyclic operation. a), b) plots of ethane conversion and aromatic yield achieved on Mo/Commercial MFI catalyst in each reaction cycle; c), d) plots of ethane conversion and aromatic yield achieved on Mo/MFI-50(T8) in each reaction cycle.

Multi-cycle reaction-regeneration testing of Mo/Commercial-MFI and Mo/MFI-50(T8) were compared because they have the same Si/Al ratio (as shown in Figure 9). At initial reaction (TOS=150s), ethane conversion notably dropped in the first cycle, and then continuously declined in the next three cycles over Mo/Commercial-MFI. The conversion for Mo/Commercial-MFI

(Figure 9a) gave total 2.60% reactivity recession in four-cycle testing. In contrary, *only* 0.46% decrease of initial reactivity was observed over Mo/MFI-50(T8) under the same cyclic testing (Figure 9c). Regarding aromatic yield (Figure 9b and 9d), Mo/Commercial MFI showed continuous decrease with the increasing of cyclic testing, and totally 1.03% decrease of aromatic yields was observed. Surprisingly, the aromatic yields greatly improved from 3.1% to ~5.0% after first regeneration for Mo/MFI-50(T8), and then minor decrease of aromatic yields in subsequent cycles. Therefore, the innovative Mo/MFI-50(T8) sample remains constant or even slightly improved aromatic productivity during multiple cyclic reactions.

Similar scenarios have been observed at ending stage of aromatization reaction (TOS=900s): ethane conversion and aromatic yield was significantly decreased at 2.8% and 1.5% for Mo/Commercial-MFI. In comparison, *only* 1.2% conversion was observed for Mo/MFI-50(T8) catalyst, while aromatic yields remains constant during four-cycle testing.

Excellent stability of Mo/MFI-50(T8) can also be validated by direct performance comparison of cycled catalyst with fresh sample. As shown in Table 7, catalytic performance (ethane conversion and aromatic yields) of spent catalyst after four cycle testing relatively mitigate >30% reactivity compared to fresh sample. The Mo/MFI-50(T8), instead, lost less than 5% of initial activity, and generate higher aromatic yield during cyclic testing. In conclusion, it is reasonable to predict that the industrial reaction/regeneration process will be operate quietly smoothly with Mo/MFI-50(T8) as a promising catalyst for ethane aromatization.

TPO profiles of the spent catalysts after the fourth aromatization reaction are shown in Figure 10. The spent Mo/Commercial ZSM-5 possess a considerably higher amount (by 21% compared to the Mo/MFI-50(T8)) of coke deposition than that of Mo/MFI-50(T8), which required

longer period for decoking under oxidative condition. The size of HZSM-5 channels is identical to the diameters of benzene and naphthalene molecules so that the coke species, polyaromatics on the *Brønsted* acid sites spatially clogged the channel[43, 66]. The hierarchical cross of ZSM-5 nanosheet, micro-mesopores structure was fabricated to afford better mass transfer for regeneration of coking combustion as well as heat diffusion. Therefore, the hierarchical structure of Mo/MFI-50(T8) had an advantage of easy regeneration for continuous operations. In summary, our study confirmed that Mo/MFI-50(T8) is a promising catalyst support for ethane aromatization under cyclic operation. We are currently optimizing regeneration temperature and other parameters, and the results will be reported soon.

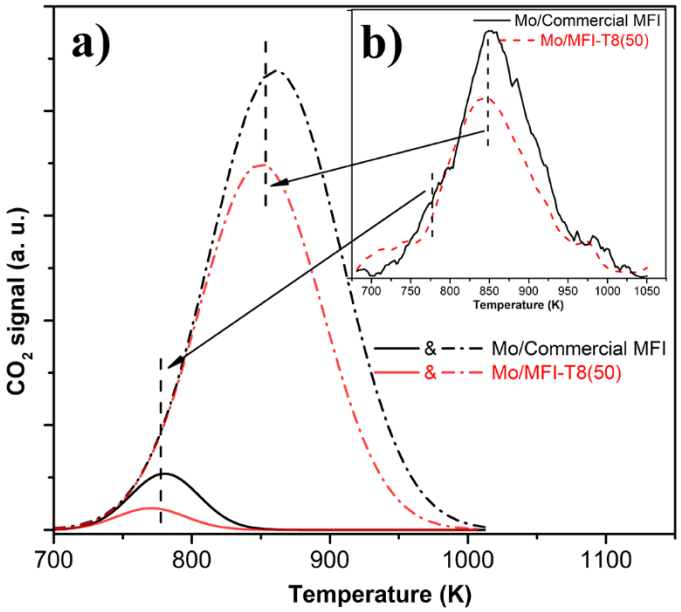

Figure 10. TPO profiles for fresh Mo/Commercial MFI and Mo/MFI-50(T8) catalyst after the fourth dehydro-aromatization reactions-regeneration cycles. The curves in the small window represent the original curves between two used catalysts. Deconvolution peaks of TPO profiles in the main window: a) back solid line and red solid line stand for carbide associated with Mo species over Mo/Commercial MFI and Mo/MFI-50(T8), respectively; b) black and red dash-dot-dash lines are assigned to coke combined with Brønsted acid sites over Mo/Commercial MFI and Mo/MFI-50(T8), respectively.

Table 7 Ethane conversion ratio and aromatics yield ratio between reactions after cyclic regeneration and reaction with fresh sample at 150 and 900s TOS

Sample	Ethane conversion ratios								Aromatics yield ratios							
	TOS=150s				TOS=900s				TOS=150s				TOS=900s			
	$\frac{x_1}{x_f}$	$\frac{x_2}{x_f}$	$\frac{x_3}{x_f}$	$\frac{x_4}{x_f}$	$\frac{x_1}{x_f}$	$\frac{x_2}{x_f}$	$\frac{x_3}{x_f}$	$\frac{x_4}{x_f}$	$\frac{y_1}{y_f}$	$\frac{y_2}{y_f}$	$\frac{y_3}{y_f}$	$\frac{y_4}{y_f}$	$\frac{y_1}{y_f}$	$\frac{y_2}{y_f}$	$\frac{y_3}{y_f}$	$\frac{y_4}{y_f}$
Mo/Commercial-MFI	0.78	0.76	0.75	0.73	0.77	0.75	0.71	0.68	0.94	0.86	0.86	0.83	0.92	0.86	0.81	0.76
Mo/MFI-T8	0.99	0.97	0.93	0.95	0.88	0.84	0.79	0.76	1.39	1.33	1.27	1.25	1.17	1.11	1.04	0.98

x: ethane conversion; y: aromatics yield; number 1-4: regeneration cycle numbers; f: ethane aromatization reaction with fresh sample.

4.4. Conclusions

Lamellar MoO_3/ZSM-5 catalysts with various thicknesses were fabricated for ethane dehydro-aromatization by adding TPAOH in the synthesis recipe. The thicker layers with longer diffusion paths of zeolite lengthen the reaction path for the reactant and thus help the shape selectivity of aromatics, despite the lower ethane conversion. The ZSM-5 support with low Si/Al ratio helps to promote the ethane conversion as well as aromatic selectivity, but it sacrifices the stability of catalytic performance. Suitable Si/Al ratios can balance high aromatic selectivity and catalytic stability. The longer diffusion pathway in ZSM-5 nanosheet can enhance the aromatic selectivity and lower the coke formation over thicker catalyst. Coke unevenly accumulated on *Brønsted* acid sites associated with Mo species, suggesting that Si/Al ratio plays a crucial role in the reaction of ethane dehydro-aromatization. During the cyclic reaction-regeneration progress, lamellar zeolites with hierarchical structure among the layers allow better mass transfer for better reproducibility, which significantly improves catalyst regenerability over the conventional Mo/ZSM-5 catalyst. Overall, Mo-based catalysts supported over novel lamellar zeolites, such as Mo/MFI-50(T8) catalyst, indicated stable reactivity during multiple-cycle reaction-regeneration operation, and could be a promising system for industrial optimization and process deployment.

Reference

[1] X. Bai, A. Samanta, B. Robinson, L. Li, J. Hu, Deactivation Mechanism and Regeneration Study of Ga–Pt Promoted HZSM-5 Catalyst in Ethane Dehydroaromatization, Industrial & Engineering Chemistry Research, 57 (2018) 4505-4513.

[2] M. Guisnet, P. Magnoux, C. Canaff, Formation and nature of coke deposits on zeolites HY and HZSM-5, in: Studies in Surface Science and Catalysis, Elsevier, 1986, pp. 701-707.

[3] X.S. Li, C. Shi, Y. Xu, X.L. Zhang, K.J. Wang, A.M. Zhu, Pulsed Streamer Discharge Plasma over Ni/HZSM-5 Catalysts for Methane Conversion to Aromatics at Atmospheric Pressure, Plasma Processes and Polymers, 4 (2007) 15-18.

[4] L. Wang, L. Tao, M. Xie, G. Xu, J. Huang, Y. Xu, Dehydrogenation and aromatization of methane under non-oxidizing conditions, Catalysis Letters, 21 (1993) 35-41.

[5] A. Krogh, A. Hagen, T.W. Hansen, C.H. Christensen, I. Schmidt, Re/HZSM-5: a new catalyst for ethane aromatization with improved stability, Catalysis Communications, 4 (2003) 627-630.

[6] O. Chetina, T. Vasina, V. Lunin, Aromatization of ethane over Pt, Ga/HZSM-5 catalyst and the effect of intermetallic hydrogen acceptor on the reaction, Applied Catalysis A: General, 131 (1995) 7-14.

[7] Y. Xiang, H. Wang, J. Cheng, J. Matsubu, Progress and prospects in catalytic ethane aromatization, Catalysis Science & Technology, 8 (2018) 1500-1516.

[8] A. Mehdad, R.F. Lobo, Ethane and ethylene aromatization on zinc-containing zeolites, Catalysis Science & Technology, 7 (2017) 3562-3572.

[9] K. Skutil, M. Taniewski, Indirect methane aromatization via oxidative coupling, products separation and aromatization steps, Fuel processing technology, 88 (2007) 877-882.

[10] S. Majhi, P. Mohanty, H. Wang, K. Pant, Direct conversion of natural gas to higher hydrocarbons: A review, Journal of Energy Chemistry, 22 (2013) 543-554.

[11] M. Guisnet, N.S. Gnep, F. Alario, Aromatization of short chain alkanes on zeolite catalysts, Applied Catalysis A: General, 89 (1992) 1-30.

[12] L. Bai, Karnowo, S. Kudo, K. Norinaga, Y.-g. Wang, J.-i. Hayashi, Kinetics and Mechanism of Steam Gasification of Char from Hydrothermally Treated Woody Biomass, Energy & Fuels, 28 (2014) 7133-7139.

[13] K. Sun, W. Gong, K. Gasem, H. Adidharma, M. Fan, R. Chen, Catalytic Methane Dehydroaromatization with Stable Nano Fe Doped on Mo/HZSM-5 Synthesized with a Simple and Environmentally Friendly Method and Clarification of a Perplexing Catalysis Mechanism Dilemma in This Field for a Period of Time, Industrial & Engineering Chemistry Research, 56 (2017) 11398-11412.

[14] Y. Shu, D. Ma, L. Xu, Y. Xu, X. Bao, Methane dehydro‐aromatization over Mo/MCM‐22 catalysts: a highly selective catalyst for the formation of benzene, Catalysis Letters, 70 (2000) 67-73.

[15] Y. Xu, L. Lin, Recent advances in methane dehydro-aromatization over transition metal ion-modified zeolite catalysts under non-oxidative conditions, Applied Catalysis A: General, 188 (1999) 53-67.

[16] Y. Wang, J. Zhou, L. Bai, Y. Chen, S. Zhang, X. Lin, Impacts of Inherent O-Containing Functional Groups on the Surface Properties of Shengli Lignite, Energy & Fuels, 28 (2014) 862-867.

[17] D.Y. Wang, Q.B. Kan, N. Xu, P. Wu, T.H. Wu, Study on methane aromatization over MoO3/HMCM-49 catalyst, Catalysis Today, 93-95 (2004) 75-80.

[18] B. Tian, Y. Qiao, L. Bai, W. Feng, Y. Jiang, Y. Tian, Pyrolysis behavior and kinetics of the trapped small molecular phase in a lignite, Energy Conversion and Management, 140 (2017) 109-120.

[19] Z.R. Ismagilov, E.V. Matus, L.T. Tsikoza, Direct conversion of methane on Mo/ZSM-5 catalysts to produce benzene and hydrogen: achievements and perspectives, Energy & Environmental Science, 1 (2008) 526-541.

[20] A. Samanta, X. Bai, B. Robinson, H. Chen, J. Hu, Conversion of Light Alkane to Value-Added Chemicals over ZSM-5/Metal Promoted Catalysts, Industrial & Engineering Chemistry Research, 56 (2017) 11006-11012.

[21] B. Robinson, X. Bai, A. Samanta, V. Abdelsayed, D. Shekhawat, J. Hu, Stability of Fe- and Zn-Promoted Mo/ZSM-5 Catalysts for Ethane Dehydroaromatization in Cyclic Operation Mode, Energy & Fuels, 32 (2018) 7810-7819.

[22] R. Chu, C. Song, W. Hou, X. Meng, Z. Miao, X. Li, G. Wu, Y. Wan, L. Bai, Improved stability of Pd/HZSM-5 bifunctional catalysts by the addition of promoters (CeO_2, CaO) for the One-step synthesis of dimethyl ether from Sulfur-containing CO_2 hydrogenation, Journal of the Taiwan Institute of Chemical Engineers, 80 (2017) 1041-1047.

[23] C. Karakaya, H. Zhu, R.J. Kee, Kinetic modeling of methane dehydroaromatization chemistry on Mo/Zeolite catalysts in packed-bed reactors, Chemical Engineering Science, 123 (2015) 474-486.

[24] M.C. Iliuta, I. Iliuta, B.P.A. Grandjean, F. Larachi, Kinetics of Methane Nonoxidative Aromatization over Ru−Mo/HZSM-5 Catalyst, Industrial & Engineering Chemistry Research, 42 (2003) 3203-3209.

[25] K.S. Wong, J.W. Thybaut, E. Tangstad, M.W. Stöcker, G.B. Marin, Methane aromatisation based upon elementary steps: Kinetic and catalyst descriptors, Microporous and Mesoporous Materials, 164 (2012) 302-312.

[26] S.S. Arzumanov, A.A. Gabrienko, D. Freude, A.G. Stepanov, In situ high temperature MAS NMR study of the mechanisms of catalysis. Ethane aromatization on Zn-modified zeolite BEA, Solid State Nuclear Magnetic Resonance, 35 (2009) 113-119.

[27] J. Gao, Y. Zheng, Y. Tang, J.-M. Jehng, R. Grybos, J. Handzlik, I.E. Wachs, S.G. Podkolzin, Spectroscopic and Computational Study of Cr Oxide Structures and Their Anchoring Sites on ZSM-5 Zeolites, ACS Catalysis, 5 (2015) 3078-3092.

[28] V.R. Choudhary, P. Devadas, S. Banerjee, A.K. Kinage, Aromatization of dilute ethylene over Ga-modified ZSM-5 type zeolite catalysts, Microporous and Mesoporous Materials, 47 (2001) 253-267.

[29] R. Srivastava, M. Choi, R. Ryoo, Mesoporous materials with zeolite framework: remarkable effect of the hierarchical structure for retardation of catalyst deactivation, Chemical Communications, (2006) 4489-4491.

[30] M. Choi, K. Na, J. Kim, Y. Sakamoto, O. Terasaki, R. Ryoo, Stable single-unit-cell nanosheets of zeolite MFI as active and long-lived catalysts, Nature, 461 (2009) 246.

[31] B. Liu, C. Li, Y. Ren, Y. Tan, H. Xi, Y. Qian, Direct synthesis of mesoporous ZSM-5 zeolite by a dual-functional surfactant approach, Chemical Engineering Journal, 210 (2012) 96-102.

[32] R. Barakov, N. Shcherban, P. Yaremov, I. Bezverkhyy, A. Baranchikov, V. Trachevskii, V. Tsyrina, V. Ilyin, Synthesis of micro-mesoporous aluminosilicates on the basis of ZSM-5 zeolite using dual-functional templates at presence of micellar and molecular templates, Microporous and Mesoporous Materials, 237 (2017) 90-107.

[33] Y. Wu, L. Emdadi, S.C. Oh, M. Sakbodin, D. Liu, Spatial distribution and catalytic performance of metal–acid sites in Mo/MFI catalysts with tunable meso-/microporous lamellar zeolite structures, Journal of Catalysis, 323 (2015) 100-111.

[34] J. Pérez-Ramírez, C.H. Christensen, K. Egeblad, C.H. Christensen, J.C. Groen, Hierarchical zeolites: enhanced utilisation of microporous crystals in catalysis by advances in materials design, Chemical Society Reviews, 37 (2008) 2530-2542.

[35] Y. Tao, H. Kanoh, L. Abrams, K. Kaneko, Mesopore-Modified Zeolites: Preparation, Characterization, and Applications, Chemical Reviews, 106 (2006) 896-910.

[36] J. Liu, L. Yu, Z. Zhao, Y. Chen, P. Zhu, C. Wang, Y. Luo, C. Xu, A. Duan, G. Jiang, Potassium-modified molybdenum-containing SBA-15 catalysts for highly efficient production of acetaldehyde and ethylene by the selective oxidation of ethane, Journal of Catalysis, 285 (2012) 134-144.

[37] K. Sun, D.M. Ginosar, T. He, Y. Zhang, M. Fan, R. Chen, Progress in Nonoxidative Dehydroaromatization of Methane in the Last 6 Years, Industrial & Engineering Chemistry Research, 57 (2018) 1768-1789.

[38] Y. Wu, L. Emdadi, Z. Wang, W. Fan, D. Liu, Textural and catalytic properties of Mo loaded hierarchical meso-/microporous lamellar MFI and MWW zeolites for direct methane conversion, Applied Catalysis A: General, 470 (2014) 344-354.

[39] D. Liu, A. Bhan, M. Tsapatsis, S. Al Hashimi, Catalytic Behavior of Brønsted Acid Sites in MWW and MFI Zeolites with Dual Meso- and Microporosity, ACS Catalysis, 1 (2011) 7-17.

[40] L. Emdadi, Y. Wu, G. Zhu, C.-C. Chang, W. Fan, T. Pham, R.F. Lobo, D. Liu, Dual Template Synthesis of Meso- and Microporous MFI Zeolite Nanosheet Assemblies with Tailored Activity in Catalytic Reactions, Chemistry of Materials, 26 (2014) 1345-1355.

[41] Y. Wu, Z. Lu, L. Emdadi, S.C. Oh, J. Wang, Y. Lei, H. Chen, D.T. Tran, I.C. Lee, D. Liu, Tuning external surface of unit-cell thick pillared MFI and MWW zeolites by atomic layer deposition and its consequences on acid-catalyzed reactions, Journal of Catalysis, 337 (2016) 177-187.

[42] D. Ma, D. Wang, L. Su, Y. Shu, Y. Xu, X. Bao, Carbonaceous Deposition on Mo/HMCM-22 Catalysts for Methane Aromatization: A TP Technique Investigation, Journal of Catalysis, 208 (2002) 260-269.

[43] Y. Song, Y. Xu, Y. Suzuki, H. Nakagome, Z.-G. Zhang, A clue to exploration of the pathway of coke formation on Mo/HZSM-5 catalyst in the non-oxidative methane dehydroaromatization at 1073K, Applied Catalysis A: General, 482 (2014) 387-396.

[44] X. Guo, G. Fang, G. Li, H. Ma, H. Fan, L. Yu, C. Ma, X. Wu, D. Deng, M. Wei, D. Tan, R. Si, S. Zhang, J. Li, L. Sun, Z. Tang, X. Pan, X. Bao, Direct, Nonoxidative Conversion of Methane to Ethylene, Aromatics, and Hydrogen, Science, 344 (2014) 616-619.

[45] K. Na, M. Choi, W. Park, Y. Sakamoto, O. Terasaki, R. Ryoo, Pillared MFI Zeolite Nanosheets of a Single-Unit-Cell Thickness, Journal of the American Chemical Society, 132 (2010) 4169-4177.

[46] C.E.A. Kirschhock, R. Ravishankar, F. Verspeurt, P.J. Grobet, P.A. Jacobs, J.A. Martens, Identification of Precursor Species in the Formation of MFI Zeolite in the TPAOH−TEOS−H_2O System, The Journal of Physical Chemistry B, 103 (1999) 4965-4971.

[47] D.D. Kragten, J.M. Fedeyko, K.R. Sawant, J.D. Rimer, D.G. Vlachos, R.F. Lobo, M. Tsapatsis, Structure of the Silica Phase Extracted from Silica/(TPA)OH Solutions Containing Nanoparticles, The Journal of Physical Chemistry B, 107 (2003) 10006-10016.

[48] K.S.W. Sing, Reporting physisorption data for gas/solid systems with special reference to the determination of surface area and porosity (Recommendations 1984), in: Pure and Applied Chemistry, 1985, pp. 603.

[49] X. Zhang, D. Liu, D. Xu, S. Asahina, K.A. Cychosz, K.V. Agrawal, Y. Al Wahedi, A. Bhan, S. Al Hashimi, O. Terasaki, M. Thommes, M. Tsapatsis, Synthesis of Self-Pillared Zeolite Nanosheets by Repetitive Branching, Science, 336 (2012) 1684-1687.

[50] H. Zheng, D. Ma, X. Bao, J.Z. Hu, J.H. Kwak, Y. Wang, C.H.F. Peden, Direct Observation of the Active Center for Methane Dehydroaromatization Using an Ultrahigh Field 95Mo NMR Spectroscopy, Journal of the American Chemical Society, 130 (2008) 3722-3723.

[51] D. Ma, W. Zhang, Y. Shu, X. Liu, Y. Xu, X. Bao, MAS NMR, ESR and TPD studies of Mo/HZSM‐5 catalysts: evidence for the migration of molybdenum species into the zeolitic channels, Catalysis Letters, 66 (2000) 155-160.

[52] J. Gao, Y. Zheng, J.-M. Jehng, Y. Tang, I.E. Wachs, S.G. Podkolzin, Identification of molybdenum oxide nanostructures on zeolites for natural gas conversion, Science, 348 (2015) 686-690.

[53] J. Gao, Y. Zheng, G.B. Fitzgerald, J. de Joannis, Y. Tang, I.E. Wachs, S.G. Podkolzin, Structure of Mo_2C_x and Mo_4C_x Molybdenum Carbide Nanoparticles and Their Anchoring Sites on ZSM-5 Zeolites, The Journal of Physical Chemistry C, 118 (2014) 4670-4679.

[54] P. Arnoldy, J.C.M. De Jonge, J.A. Moulijn, Temperature-programed reduction of molybdenum(VI) oxide and molybdenum(IV) oxide, The Journal of Physical Chemistry, 89 (1985) 4517-4526.

[55] S. Rajagopal, H.J. Marini, J.A. Marzari, R. Miranda, Silica-Alumina-Supported Acidic Molybdenum Catalysts - TPR and XRD Characterization, Journal of Catalysis, 147 (1994) 417-428.

[56] K. Chen, S. Xie, A.T. Bell, E. Iglesia, Structure and Properties of Oxidative Dehydrogenation Catalysts Based on MoO_3/Al_2O_3, Journal of Catalysis, 198 (2001) 232-242.

[57] G.V.A. Martins, G. Berlier, C. Bisio, S. Coluccia, H.O. Pastore, L. Marchese, Quantification of Brønsted Acid Sites in Microporous Catalysts by a Combined FTIR and NH_3-TPD Study, The Journal of Physical Chemistry C, 112 (2008) 7193-7200.

[58] Y. Xu, Y. Shu, S. Liu, J. Huang, X. Guo, Interaction between ammonium heptamolybdate and NH_4ZSM-5 zeolite: the location of Mo species and the acidity of Mo/HZSM-5, Catalysis Letters, 35 (1995) 233-243.

[59] R. Kawase, A. Iida, Y. Kubota, K. Komura, Y. Sugi, K. Oyama, H. Itoh, Hydrothermal Synthesis of Calcium and Boron Containing MFI-Type Zeolites by Using Organic Amine as Structure Directing Agent, Industrial & Engineering Chemistry Research, 46 (2007) 1091-1098.

[60] F. Yaripour, Z. Shariatinia, S. Sahebdelfar, A. Irandoukht, Effect of boron incorporation on the structure, products selectivities and lifetime of H-ZSM-5 nanocatalyst designed for application in methanol-to-olefins (MTO) reaction, Microporous and Mesoporous Materials, 203 (2015) 41-53.

[61] I. Lezcano-González, R. Oord, M. Rovezzi, P. Glatzel, S.W. Botchway, B.M. Weckhuysen, A.M. Beale, Molybdenum Speciation and its Impact on Catalytic Activity during Methane Dehydroaromatization in Zeolite ZSM-5 as Revealed by Operando X-Ray Methods, Angewandte Chemie International Edition, 55 (2016) 5215-5219.

[62] A. Smiešková, P. Hudec, N. Kumar, T. Salmi, D.Y. Murzin, V. Jorík, Aromatization of methane on Mo modified zeolites: Influence of the surface and structural properties of the carriers, Applied Catalysis A: General, 377 (2010) 83-91.

[63] W. Ding, S. Li, G. D Meitzner, E. Iglesia, Methane Conversion to Aromatics on Mo/H-ZSM5: Structure of Molybdenum Species in Working Catalysts, The Journal of Physical Chemistry B, 105 (2001) 506-513.

[64] B. Hunger, M. Heuchel, L.A. Clark, R.Q. Snurr, Characterization of Acidic OH Groups in Zeolites of Different Types: An Interpretation of NH_3-TPD Results in the Light of Confinement Effects, The Journal of Physical Chemistry B, 106 (2002) 3882-3889.

[65] N. Kosinov, A.S.G. Wijpkema, E. Uslamin, R. Rohling, F.J.A.G. Coumans, B. Mezari, A. Parastaev, A.S. Poryvaev, M.V. Fedin, E.A. Pidko, E.J.M. Hensen, Confined Carbon Mediating Dehydroaromatization of Methane over Mo/ZSM-5, Angewandte Chemie International Edition, 57 (2018) 1016-1020.

[66] Y.-H. Kim, R.W. Borry, E. Iglesia, Genesis of methane activation sites in Mo-exchanged H–ZSM-5 catalysts, Microporous and Mesoporous Materials, 35-36 (2000) 495-509.

[67] H. Liu, X. Bao, Y. Xu, Methane dehydroaromatization under nonoxidative conditions over Mo/HZSM-5 catalysts: Identification and preparation of the Mo active species, Journal of Catalysis, 239 (2006) 441-450.

[68] H. Jiang, L. Wang, W. Cui, Y. Xu, Study on the induction period of methane aromatization over Mo/HZSM-5: partial reduction of Mo species and formation of carbonaceous deposit, Catalysis Letters, 57 (1999) 95-102.

[69] E.V. Matus, I.Z. Ismagilov, O.B. Sukhova, V.I. Zaikovskii, L.T. Tsikoza, Z.R. Ismagilov, J.A. Moulijn, Study of Methane Dehydroaromatization on Impregnated Mo/ZSM-5 Catalysts and Characterization of Nanostructured Molybdenum Phases and Carbonaceous Deposits, Industrial & Engineering Chemistry Research, 46 (2007) 4063-4074.

[70] N. Kosinov, F.J.A.G. Coumans, G. Li, E. Uslamin, B. Mezari, A.S.G. Wijpkema, E.A. Pidko, E.J.M. Hensen, Stable Mo/HZSM-5 methane dehydroaromatization catalysts optimized for high-temperature calcination-regeneration, Journal of Catalysis, 346 (2017) 125-133.

Chapter 5. Conclusions

The research efforts conducted for this work represent a contribution to the field of shale gas combustion and utilization via multiple promising schemes at various O_2 partial pressure conditions. In this research, chemical looping combustion (CLC) of methane with inherent CO_2 capture, oxidative coupling of methane (OCM) and dehydro-aromatization (DHA) of ethane are systematically studied as promising alternatives at O_2-rich, O_2-lean and nonoxidative conditions, respectively. The work offers several economically-viable and technically-feasible solutions for shale gas utilization to value-added products. The present research provided fundamental insights of surface structure performance relationships of model catalysts for catalytic methane/ethane conversion. Briefly:

The study of chemical looping combustion (CLC) of methane with inherent CO_2 capture study (**Chapter 2**) reveals the oxygen transfer mechanisms in CLC by using the surface calcium-doped (1, 2 and 4 wt%) copper oxide-based OC. In this chapter, the Ca is well-dispersed on the CuO surface without deep penetration to the bulk, confirmed by the combination of XPS and XRD characterizations. CaO-CuO oxygen carriers present three reductive active sites corresponding to CuO reduction, CaO reduction and impurity $CaCO_3$ decomposition in H_2-TPR. The surface modification with the alkaline earth metal Ca promotes CuO oxygen uncoupling characteristics, since Ca surface-doping increases the lattice oxygen transfer and surface O_2 formation rate under CLOU conditions. The reduction pathway for CuO from a sequential ($CuO \rightarrow Cu_2O \rightarrow Cu$) to a direct transition ($CuO \rightarrow Cu$) during is verified through the decomposition of oxygen carriers and *in situ* Raman analysis. When methane was used as gaseous fuel in the CLC process, the calcium dopant not only accelerates the reaction rate, but also induces methane reforming reaction by

reacting with released CO_2, which was initially bound in the form of $CaCO_3$, to promote the formation of CO and H_2. (**Publication**: Lei Bai, Jarret Riley, Hanjing Tian, Zili Wu, Si Luo, He Qi, Haiyang Li, Xingbo Liu. Mechanism Study of Char/Methane Chemical Looping Reduction Process Over Calcium-doped Copper Oxide as Oxygen Carrier. Submitted to *Applied Energy*.)

Extending the CLC work in O_2-rich conditions from Chapter 2 into **Chapter 3** allowed the investigation of the effect of surface compositions of perovskites on the OCM by using $SrTiO_3$ as a model catalyst in O_2-lean conditions. Specifically, in this chapter, a set of $SrTiO_3$ samples was synthesized with different surface densities of Sr (25-96%, verified by Low Energy Ion Scattering (LEIS)), through incipient wetness impregnation, chemical etching with HNO_3, and thermal treatment. The redox capability for STO samples was found to be the same due to the same bulk structure. Therefore, their different catalytic performance was studied and related to the surface acid-base properties rather than reducibility properties. The surface basicity and composition have been studied via NH_3-/CO_2-TPD, UV-Raman, LEIS, etc. The OCM reaction at steady state was performed at 600-800 ^oC and it was found that the Sr enrichment enhances the CH_4 conversion, C_2 selectivity as well as the ratio of C_2H_4/C_2H_6 up to a certain surface Sr concentration. Furthermore, it was found that the catalytic activity (CH_4 conversion) increases linearly with the relative concentration of basic sites (base/(base+acid)) over the STO catalysts at the full range of surface Sr concentrations, rendering the relative concentration of basic sites as a tentative descriptor for the activity of STO samples in the OCM reaction. This work shows the clear correlation between surface compositions, relative basicity/acidity and OCM catalytic performance over perovskite catalysts. Overall, it is suggested that tuning the surface reconstruction/composition of perovskites can be an effective approach to control CH_4 activation and conversions.(**Publication**: Lei Bai, Felipe Polo-Garzon, Zhenghong Bao, Si Luo, Hanjing Tian*, Zili Wu*. Effect of Surface

Composition of $SrTiO_3$ on Oxidative Coupling of Methane (OCM). Just Accepted. DOI:10.1002/cctc.201900159. ChemCatChem. 2019.)

Lastly, in **Chapter 4**, we designed a regenerable MoO_x/lamellar ZSM-5 was designed with the strategy of optimizing the micro/mesopores structure of the zeolite framework. The pillar ZSM-5 is applied in the non-oxidative ethane dehydroaromatization reaction, and high ethane conversion and aromatic selectivity were obtained by optimizing Si/Al ratio, surface acidity and diffusion path. The thicker layers with longer diffusion paths of zeolite lengthen the reaction path for the reactant and thus help the shape selectivity of aromatics, despite the lower ethane conversion. ZSM-5 support with low Si/Al ratio helps to promote the ethane conversion as well as aromatic selectivity, but it sacrifices the stability of catalytic performance. Suitable Si/Al ratios can balance high aromatic selectivity and catalytic stability. The cyclic reaction-regeneration strategy was utilized to remove the produced coke, lamellar zeolites with hierarchical structure among the layers allows better mass transfer for better reproducibility, which significantly improve catalyst regeneratability than conventional Mo/ZSM-5 catalyst. Overall, Mo-based catalysts supported over novel lamellar zeolites, such as Mo/MFI-50(T8) catalyst, indicated stable reactivity during multiple-cycle reaction-regeneration operation, and could be a promising system for industrial optimization and process deployment. (**Publication**: Jiahui Ye[#], Lei Bai[#], Baoyu Liu, Hanjing Tian*, Jianli Hu, Felipe Polo-Garzon, Richard T. Mayes, Zili Wu, Yanxiong Fang*. Fabrication of ZSM-5 Framework for Shape Selectivity of Ethane Dehydroaromatization. (# for equal contribution, Just Accepted. DOI: 10.1021/acs.iecr.8b04965. Industry & Engineering Chemistry Research. 2019.)